Department of Precision and Microsystems Engineering

Variable thickness and initially curved flexures for improved flexure mechanisms

F.W.F. Colin

Report no : 2023.020
Coach : A. Yaşır
Professor : J.L. Herder
Specialisation : Mechatronic System Design
Type of report : Master Thesis
Date : 25 April 2023

TU Delft Delft University of Technology

Challenge the future

Variable thickness and initially curved flexures for improved flexure mechanisms

Variable thickness and initially curved flexures for increased support stiffness and minimal stress

by

F.W.F. Colin

to obtain the degree of Master of Science
at the Delft University of Technology,
to be defended publicly on April 25, 2023 at 14:30 AM.

Student number:	4452569	
Project Duration:	September, 2022 - April, 2023	
Faculty:	Faculty of Precision and Microstystems Engineering	
Company:	ASML, departement of Mechanical Analysis	
Thesis committee:	Prof. dr. ir. J.L. Herder	TU Delft, supervisor
	Ir. A. Yaşır	TU Delft, daily supervisor
	Ir. G. Radaelli	TU Delft
	Ir. E. Mulder	ASML, daily supervisor

An electronic version of this thesis is available at http://repository.tudelft.nl/

TU Delft ASML

Preface

This work presented is my MSc thesis that I have been working on for the last 8 months. This work has been conducted in part as a collaboration with ASML. My journey to the departement of Precision and Microsystems Engineering has been an unorthodox one as I started and finished my Bachelor in Industrial Design Engineering. Over the years in Delft I gradually found my passion which ultimately led me to mechanical engineering in the departement of Biomechanical Design. After following the courses precision mechanism design and compliant mechanisms it was even more clear for me what my true passion is and the switch to PME was an easy one. I really loved working on this topic and with a bit of hope, I can continue similar work in the future.

First and foremost I would like to thank Erwin Mulder. He was the supervisor from ASML that anyone could only hope for. He had enormous amounts of time available for brainstorming and help on many topics. I learned a lot from him and again would like to thank him for this collaboration.

Eventhough we did not spend the same amount of time brainstorming and discussing my project as I did with Erwin, I would like to thank Abdullah and Just for guiding me through this process. I really like the approach you took in letting me be free in exploring what I found interesting and helping me a lot in structuring and learn to better and clearer convey my research. I also want to thank you for having the faith in my research and giving me the opportunity to create and test a genuine working prototype, it really brought my research to life!

I would like to thank Giuseppe to be part of my graduation committee and I hope you find the research as interesting as I found it.

Lastly I would like to thank Jaques Brenkman for helping me setup my experiment and letting me do my experiments swiftly.

F.W.F. Colin
Delft, April 2023

Summary

In the high-precision industry, there is an increasing drive to increase performance in precision and speed. In the field of lithography machines, there is a drive to increase the range of motion and support stiffness for compliant mechanisms. These mechanisms are the perfect fit due to their excellent properties in repeatability, no need for lubrication and a lack of friction. These compliant mechanisms pose a few common limitations such as their limited range of motion, high stress peaks and a significant drop in support stiffness when deflected.

In the first part of this thesis, various approaches for development of high range of motion compliant one degree-of-freedom guiding mechanisms are compared on their precision, range of motion and support properties. Two approaches from literature, namely variable thickness flexures and initially curved flexures show high potential. Variable thickness flexures show promise in terms of increasing support stiffness when deflected and show the ability to minimize stress for flexures with the same reaction force. The use of initially curved flexures show potential by using the non-linearities these flexures bring to increase precision and support stiffness.

In this thesis, the research is divided into 2 parts. First, the influence of variable thickness flexures is examined in Paper I. As numerous flexure mechanisms utilize parallelogram flexure mechanisms, a comparison is made for fixed guided beams and their improvement in terms of support stiffness and stress peaks in comparison to the more common constant thickness flexures. These variable thickness flexures are parameterized by 2 novel shape functions using quadratic and cubic bezier curves. This thickness profile is then used in a custom built mesher to generate a consistent mesh, resulting in a massive time saving. This mesh is used to evaluate the stress and stiffness using an Ansys APDL solver called from python. This method of using a custom mesher and calling Ansys from python decreases the simulation time per design iteration to 10-20 seconds compared to 1-2 minutes in Ansys Workbench, making it feasible to optimize designs with thousands of design iterations.

Three cases were evaluated, the first case optimizes the stiffness ratio of the flexure, defined as the support stiffness when deflected, C_x, divided by the undeflected support stiffness, C_{x0}. An increase of 114% can be achieved using variable thickness flexures. The second case optimizes the support stiffness when deflected, C_x, while maintaining the same drive stiffness. The idea of this optimization is to design a flexure that can replace a flexure in a current mechanism without compromising on other aspects and be a viable replacement part with better performance. In this case an increase of 125% is observed using a variable thickness flexure incorporating a partially rigid midsection. The last case tries to minimize the peak stress for a flexure with the same drive stiffness as its constant thickness counterpart. In this case a decrease in stress of 31% can be achieved.

The second part of this research (Paper II) implements this approach of using variable thickness in another promising design approach, namely initially curved flexure mechanisms. This is relatively new design strategy shows great potential in terms of increasing support stiffness by handing over support stiffness as one or more flexures increase their stiffness by straightening when deflected. Another research looked at the ability to optimize mechanisms with very low parasitic errors and a well constrained uncontrollable mass. To further analyse the ability of this approach, 3 cases are evaluated. The first case aims to generate a mechanism with a near-constant support stiffness over the full stroke. Case 2 aims to generate a mechanism with a very low parasitic error and case 3 optimizes a mechanism with a maximum stroke subject to parasitic motion, stress and minimum stiffness ratio constraints. These cases are evaluated with the method introduced in previous research and secondly, to see the influence variable thickness can pose in terms of stiffness increase in case 1 and 2 and in decreased stress peaks and thus increased range of motion for case 3, variable thickness is added and a second optimization is done with the previously found mechanisms.

To generate these new design geometries, Matlab optimization is used in combination with *SPACAR*, a nonlinear finite element software package in Matlab. The optimizer optimizes the locations of multiple control points that are used to generate bezier curves that represent the leaf flexures with initial curvature. These bezier curves are discretized in beam sections that are used by *SPACAR*. Besides the curvature, the thickness of each flexure is optimized at the same time and for the mechanisms with variable thickness flexures, 3 parameters per flexure are added. Since *SPACAR* uses beam elements and runs natively in Matlab, it is very fast in comparison to other commercial FEA software packages, making it ideal for these optimizations with large sets of parameters and highly nonlinear behaviour.

Case 1 resulted in a mechanism with a support stiffness difference of only 0.1% with a parasitic translation of $10\,$µm and a stiffness ratio (support stiffness, C_y, divided by the drive stiffness, C_x) of 248. Incorporating variable thickness increases this stiffness ratio further to 503, an increase of 103%. Case 2 results in a mechanism with a parasitic motion of only $0.2\,$µm and a stiffness ratio of 729. When variable thickness is added, an increase of 84% in stiffness ratio and an increase of 26% in mean support stiffness can be achieved. The last case looks to maximize the stroke for a mechanism with a maximum parasitic translation of $10\,$µm and a minimum stiffness ratio of 100. Using constant thickness flexures, a stroke of $27.65\,$mm can be achieved and by using variable thickness flexures this can be increased to $30.60\,$mm, an increase of 10.7%.

To evaluate the results obtained from *SPACAR*, the mechanism from case 1, the constant support stiffness mechanism, is evaluated with quadratic solid elements in Ansys and an aluminium version is created using wire EDM and measurements are done to compare the methods. A very high similarity in parasitic motion is seen, however to evaluate the constant stiffness, a deviation from *SPACAR* and Ansys can be seen. This is most likely due to using fitted data that is used to calculate the induced parasitic motion in multiple steps and thus stacking the error every time the data is used to calculate the next data points.

From this research it can be concluded that variable thickness flexures offer significant improvements over commonly used constant thickness flexures in terms of increased support stiffness and decreased maximum stress levels. Additionally, generating mechanisms using initially curved flexures show potential in many fields, such as constant support stiffness, high precision and increased range of motion. If these two methods are combined, an ever higher increase in performance in terms of increasing support stiffness and range of motion can be achieved making it a very promising method that can influence a lot of different designs in a variety of different applications.

Contents

1

Review article: Comparison of different design methods and their influence on compliant mechanisms towards the design of large range of motion and minimal parasitic error mechanisms

Review article: Comparison of design methods for large range of motion compliant mechanisms for motion guidance

F.W.F. Colin [1]

[1] *Department of Precision and Microsystems Engineering, Faculty of 3mE, Delft University of Technology, Delft, the Netherlands*

ARTICLE INFO

Keywords:
Parasitic motion
Range of motion
Cross-coupling
Compliant mechanism
Support stiffness

Abstract

In the field of precision engineering, perfect positioning accuracy is necessary. This is often done by means of compliant mechanisms that offer zero backlash, no friction and require no lubrication. Using elastic deformation of compliant elements is limited to the maximum allowable stress resulting in small-range motion devices. This paper compares different design methods from literature of achieving a high range of motion mechanisms, their influence on the parasitic motion and their influence on the stiffness in support and out-of-plane directions. This comparison is made for 1 degree of freedom(rotational and linear translation) mechanisms with the aim to find the most promising methods to achieve the goal of a high range of motion mechanism with optimal support and out-of-plane stiffness while having minimal parasitic motion. Initially curved and variable thickness flexures show the best performance towards this goal and 2 case studies are done to show the potential of these methods and to bridge the gap in the literature.

1 Introduction

Compliant mechanisms become more and more important in precision mechanisms. High-precision motion stages in the field of lithography, for example, have an increasing need for larger ranges of motion. Compliant mechanisms are the perfect fit as they exhibit no friction, require no lubrication and have near-perfect repeatability. The downside is that the range of motion is limited by the material properties and in particular, the maximum allowable stress concentrations [1–3].

This limited range of motion can influence the choice between compliant mechanisms over the use of more complex and space-consuming alternatives such as air bearings or magnetic bearings. In the field of lithography for example the use of air or magnetic bearings is quite common [4, 5]. A few examples of the advantages of these alternatives are very low parasitic motion, high support stiffness and virtually no friction. Disadvantages are size and complexity which sums up to higher cost [3]. Besides that, air bearings are limited to work in non-vacuum environments, limiting their use in lithography applications. That leaves only the option for magnetic levitation, which is even more complex as the parasitic motions need to be minimized using active measuring and controlling.

Besides linear guiding, precision stages also require output decoupling to prevent the need for position mapping or other active compensation methods to generate the desired output. Output decoupling in this context is stated as generating an output in the desired degree of freedom without any parasitic motion in the non-actuated directions. A perfectly decoupled mechanism is, based on Hooke's Law, only achieved if you have a diagonal stiffness matrix [6–9]. This property can be achieved if the motion generated by one straight-line guiding mechanism is free of parasitic motion, thus adding no strain due to deformation in undesired directions.

An alternative compliant high range of motion guiding can have merits in terms of low cost, no backlash and friction, vacuum compatibility and easy manufacture [10]. This, and the minimal parasitic errors, leads us to the objective of this paper.

This paper aims to give an overview of the design methods available for use in compliant precision mechanisms and their influence on the range of motion, support capabilities and parasitic properties.

The structure of this paper is as follows: the method is firstly discussed, then the classification is proposed in chapter 3. Then the results are discussed and compared in chapter 4. Afterwards, there is a discussion and conclusion chapter. A combination of promising methods in two test cases is further analyzed in the Appendix.

2 Search method

The following search criteria were used to find relevant research on the topics of high precision, large range of motion, thickness varying and initially curved

mechanisms in the field of compliant mechanisms.

The search was limited to 1 degree of freedom mechanisms only, as the effects towards the metrics are more equally compared and thus the effect of different design methods can be compared more fairly.

The search for relevant literature was conducted in 2 search engines, Google Scholar and Scopus. The search terms used are listed in table (1) and (2).

Table 1. Search terms used to find relevant research on parasitic behavior of compliant mechanisms. Vertical search terms are combined with 'OR' and columns are combined with 'AND'

Compliant mechanism	parasitic motion
Flexure mechanism	accuracy
Compliant	axis drift
Flexure	axis shift
Leaf spring	center of rotation drift
Notch OR Lumped	center of rotation shift

Table 2. Search terms used to find relevant research on initially curved flexures. Vertical search terms are combined with 'OR' and columns are combined with 'AND'

Initially curved	compliant mechanism	parasitic motion
Wide curve	flexure mechanism	output decoupling
Bezier curve	compliant	path following
Spline	flexure	stress minimization
Thickness varying	leaf	accuracy
Variable thickness	spring	axis drift
		axis shift
		center of rotation drift
		center of rotation shift

3 Classification

In the classification, to compare methods equally, rotational mechanisms are compared to each other and linear guiding mechanisms are compared to each other(Level 1, see figure (4)). Maximum rotation is hard to compare to translation and the applications are often different. Other types of motion were not taken into account, as the majority of 1 degree of freedom mechanisms can be described by the first two.

The second level is the compliance type. Lumped(notch flexures) and distributed(leaf flexures). Hybrid variants are also not taken into account as here again, the majority can be labeled as either lumped or distributed. Level 3 is the initial curvature level 4 is the thickness type. See figure (2) for some examples of linear mechanisms from literature that fall into different categories as part of the classification and figure (3) for examples of rotational mechanisms.

To compare the linear and rotational mechanisms, some metrics will be used. Those metrics are as follows: the metric to compare the range of motion is the maximum deflection normalized to length L. See figure (4)

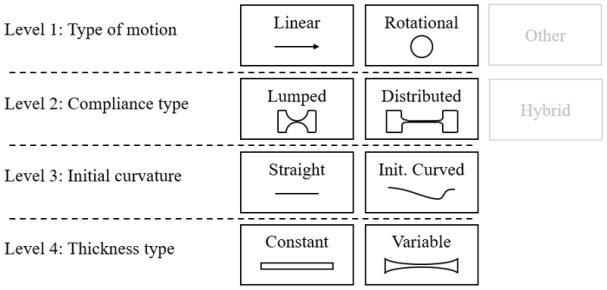

Figure 1. Schematic representation of the classification levels to compare the design methods

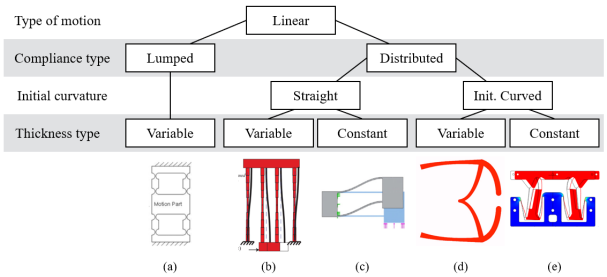

Figure 2. Classification tree for linear mechanisms with some example mechanisms from literature. Figures retrieved from: a [11], b [12], c [13], d [14], e [15]

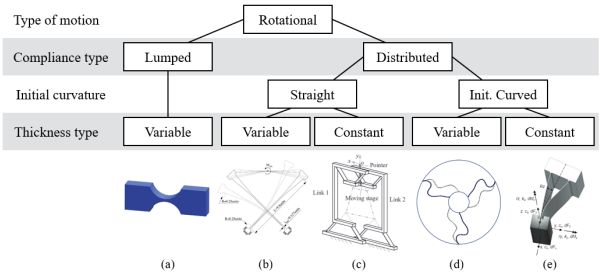

Figure 3. Classification tree for rotational mechanisms with some example mechanisms from literature. Figures retrieved from: a [16], b [17], c [18], d [19], e [20]

The parasitic motion(δe_y) is another important factor and this again is the percentage of the maximum parasitic error normalized to Δx_{max}.

The last 2 important metrics to compare are the support stiffness in-plane and out-of-plane. These metrics give an insight into the different methods and their ability to be used for higher-loading applications. Higher stiffness in these "constrained" directions means that the parasitic motion in these directions will also be lowered.

4 Results

Using the classification proposed in chapter 3, the mechanisms and shape concepts for linear guiding

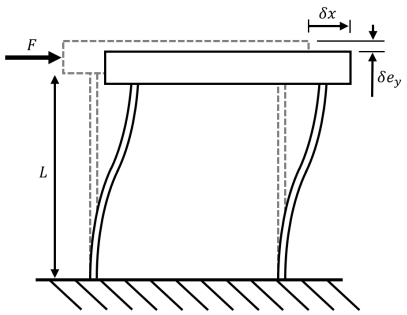

Figure 4. Parasitic motion definition for parallelogram mechanism

mechanisms are shown in table (3). In table (4), the comparison of rotational mechanisms is shown. The use of a + and - grading system is used for the in-plane and out-of-plane stiffness, as these are mentioned but often not quantified in literature.

In tables (3) and (4) you can find an overview of the different design methods and for different types of mechanisms their advantages and disadvantages. The rest of this chapter will go into further detail on the methods and their specific uses and advantages and downfalls.

4.1 Lumped flexure mechanisms

For high-precision devices, lumped, more commonly known as notch flexures, are a popular choice. They offer higher strength and concentrated deflection resulting in a small rotation center shift and thus a more accurate rotation [48], however, flexural pivots are prone to stress concentration and thus limit the mechanisms to have use in small-deflected applications with small angular displacements [54, 55].

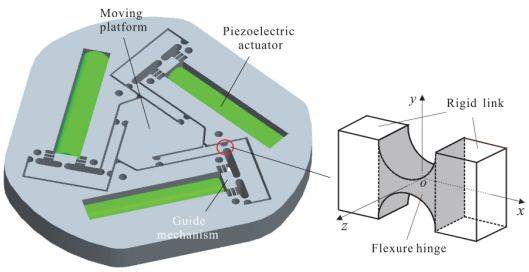

Figure 5. Use of notch flexure hinges in a compliant micro–motion stage. Figure retrieved from [41]

As these hinges are commonly used in precision mechanisms(see figure (5) for a micro-motion stage that uses notch hinges), the axis shift or parasitic motion is an important factor. Normally a higher accuracy also means a higher stiffness [1, 61]. Different methods for generating notches with higher accuracy are discussed in [40, 41, 61], using exponent-sine-shaped flexure hinges and topology optimization to generate quasi-V-shaped flexure hinges topology optimization to minimize parasitic motion optimizing cartwheel like notch hinges.

Apart from minimal parasitic motion, range of motion is an important property as well. As discussed before, the optimal hinge has a high range of motion while having good accuracy, so in designing this ideal hinge, different approaches in terms of optimization are proposed in literature. Optimizing the contour of the notch can increase the range of motion of the hinge [38] but can also increase the ratio of bending to axial compliance by optimizing for the highest stiffness in the axial direction while keeping the compliance in the compliant direction above a set limit [47] or by using multi-objective optimization [62].

These methods are still bounded by the shape functions used that are optimized, limiting the possible design domain. So to have complete freedom, a different method is to design flexure hinges using topology optimization. Allowing for every possible shape as each element in the full design domain can be turned on or off independently. By optimizing for a given compliance matrix and displacement, new geometries can be generated to achieve these properties [42, 63]. Koppen et al. used this method to generate 3D mechanisms as well. Here the different degrees of freedom can be picked to be active and the others will be stiff, however, these optimized shapes are only valid for small deflections when linear stress-strain and a linear strain-displacement relationship suffice [63]. See figure (6)

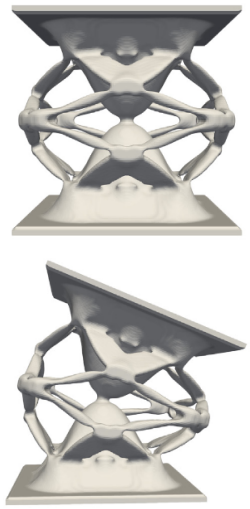

Figure 6. Optimized hinge to be stiff in all directions except RX and RY. Figure retrieved from [63]

4.2 Constant thickness straight flexures

The advantages of notch flexures over leaf flexures are their ability to have higher accuracy, higher strength and more concentrated deformation [48]. In contrast,

Table 3. Comparison table for linear guiding mechanisms showing the range of motion and the effects of the methods on parasitic error, the in-plane support stiffness and out-of-plane support stiffness. A + sign means a good performance and a **-** sign means a worse performance. If data was not available, relevant, or could not be based on other things the cell is left blank.

		Mechanism	Method	Reference	RoM $\Delta y/L$	Parasitic error $\delta e_x/\Delta y$	In plane stiffness	Out-of-plane stiffness
Lumped		Displacement amplifier	Notched double parallelogram	[11]	0.53%		+	+
		Parallelogram	Notched parallelogram(mirrored)	[21]	0.1%	0	+	+
Straight	**CT**	Parallelogram		[22, 23]	$0.6\% - 5\%$	$0.36\% - 15\%$*	-	-
		Parallelogram	Mirror stacked	[13]	2.25%	0.200%	+	
		parallel-DPFM		[24]	2.78%	0	+	
		Parallel XY stage	Double parallelogram	[2, 11, 23, 25–30]	10%	0.0005%	-	-
		Double Parallelogram	Nested stages	[29, 30]	$10\% \times N$		-	
			Robberts mechanism	[31, 32]	10%	1.700%	+	+
			Spacial configuration of DP	[3]	16.70%	0.013%	+	+
		Linear motion guide	Use COR shift	[33]	36%	0.056%	-	-
	VT	VT double parallelogram		[12]	14%**	0.0005%	-	
Init. Curved	**CT**	Linear stage	Opt. IC flexure guiding mechanism	[15]	10%	0.071%	+	+
		Folded leaf spring	STAGE method Folded Leaf Spring	[34]	30%			+
		Folded leaf spring	Double element Folded leaf spring	[34]	21%			+
			semicircular flexures	[35]	3.13%		-	-
	VT	Constant force mechanism		[36]	20%			-

CT = Constant thickness, VT = Variable thickness
* Calculated using formula from [26]
** Based on results from Appendix A.1

Table 4. Comparison table for rotational mechanisms showing the maximum angle and the effects of the methods on axis drift, the in-plane support stiffness and out-of-plane support stiffness. A + sign means a good performance and a **-** sign means a worse performance. If data was not available, relevant, or could not be based on other things the cell is left blank.

		Mechanism	Method	Reference	Angle [deg]	Axis drift	In plane stiffness	Out-of-plane stiffness
Lumped		Notch hinge	Circular notch hinge	[37]	±0.5	0	+	+
		Optimized notch	shape optimization	[38, 39]		+	+	+
			Sine shape notch	[40]	±0.57	+	+	+
			Topology opt for high stiffness ratio	[41, 42]		+	+	+
			Multicavity flexure hinge	[43]	*		+	
			Deep notch optimization(ellipsoid)	[44, 45]	±1	+	+	+
			Power-function geometry/ spline optimization	[46–48]		+	+	
Straight	**CT**	Cross flexure		[49]	±30	-	-	
		Trapezoidal mechanism	Use COR shift to compensate parasitic motion	[18]	±5	0		
		Trapezoidal mechanism	Stack stages	[50]	±3.3	+		
	VT	Cross flexure	Variable thickness flexure pivot(VTFP)	[17, 51, 52]	±20	0	+	
Init. Curved	**CT**	Cross flexure	Pre-stressed flexures to minimize stress peaks	[34]	±45	-	-	
		Rotation hinge	Curved Hinge Flexure (CHF)	[20]	±15		+	+
			Curved Hinge Flexure (CHF)	[53]	±20		+	+
		Optimized notch	large displ. Notch(use initially curved leafs)	[54]	±60	+	-	-
		Optimized rotation mechanism	Curved flexures to opt angle	[55]	6.67**		-	-
		Optimized notch	Curved flexures as notch flex	[56]		0		
		Cross flexure	Curved cross flexure leafs	[57]	±90	+	-	-
			semicircular flexures	[58]	±90	+	-	-
	VT	Constant torque		[19, 59, 60]	±20		-	-

CT = Constant thickness, VT = Variable thickness
* Compliance 5.4× higher in working direction as multi notched flexure hinge [43]
** More than twice compared to the folded flexure variant [55]

leaf flexures are very good at large rotations and displacements [64].

Towards these problems some methods are used to mitigate part of the problems. These methods and their uses and properties are discussed further in this chapter.

4.2.1 Use of serial stages

For straight-line motion, the most common method is using a parallelogram layout(see figure (4)), this prevents parasitic rotation(if actuated in the stiffness center and for small translations) and for small translations the parasitic motion is minimal. For this mechanism, the equation for the approximation of

the parasitic error is described in equation (1) [26]

$$\delta e_y = \frac{3\delta x^2}{5L} \tag{1}$$

As can be seen in equation (1), the parasitic motion can be reduced by either limiting its range or increasing L.

As increasing the length of the flexures is often not an option, as in practice the length is restricted by the compactness requirements of the design [23, 29]. Another strategy to decrease parasitic motion is by using stacked intermediate stages. This has 2 main advantages.

Firstly, the second parasitic motion is canceled as the parasitic motion of the first set of flexures is equal and opposite. See figure (7) for an example of a double parallelogram mechanism. This double parallelogram mechanism is widely used in 2-degree-of-freedom positioning stages for its excellent properties in minimizing parasitic motion and output decoupling [2, 11, 23, 25–30].

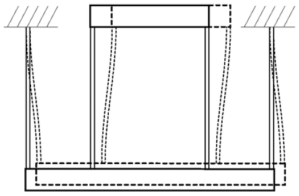

Figure 7. Double parallelogram mechanism. Figure retrieved from [65]

The second advantage is that the necessary displacement per set of flexures is lowered thus resulting in larger allowable displacements with acceptable parasitic motion and stress levels [66]. This lower displacement per leaf also has an advantage towards its axial stiffness as the axial stiffness has an inverse-quadratic correlation with respect to the transverse displacement causing problems in supporting larger masses [22]. These advantages are further extended by using the multi-stage compound parallelogram flexure concept. The motion range is enlarged by N times, where N is the number of basic modules [29, 30].

A few disadvantages of this use of intermediate bodies include dynamic and axial stiffness issues due to the under-constrained bodies that are susceptible to parasitic errors, unwanted vibrations and poor controllability [67]. This is in the case of the double parallelogram mechanism because the degree of freedom of the intermediate stage is the same as the final stage [29, 66].

A way to mitigate this problem is to remove the under-constrained intermediate body. This can be done by implementing a mechanism that forces the $2:1$ ratio of the motion of the final stage to the intermediate stage. See figure (8) for 2 examples of such mechanisms. Constraining the intermediate stage results in an $11\times$ gain in resonance frequency and $134\times$ gain in static stiffness of the unconstrained motion of the intermediate body [66, 67]. The downside is a more complex system.

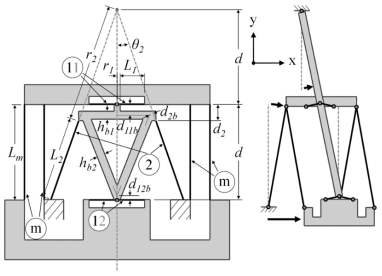

Figure 8. Perfectly constrained double parallelogram mechanism. Figure retrieved from [66]

The second problem is the axial stiffness. A solution to the axial stiffness can be the inversion principle [68]. Using flexures in tension instead of compression increases the maximum allowable load. Hao et al. proposed new designs to eliminate the loading direction stiffness by placing beams in tension and compression at the same time [24]. It has the same parasitic error as the compound parallel flexure mechanism but at the same time the same stiffness as a single parallel leaf set in tension. This, however, comes at the cost of higher internal stresses.

4.2.2 Use of straight line mechanisms

A way of increasing the range of motion while keeping the parasitic motion to a minimum is by using straight-line mechanisms. The most common example is the Roberts approximate straight-line mechanism. The compliant version of the mechanism is used in an XY-positioning stage by Wan et al. to increase the working space while still having a parasitic motion of less than 1.7% [32].

Another example of a high stroke linear motion mechanism is the XBob, a straight line mechanism using a double Roberts approximate straight-line mechanism with the original mechanisms output body rigidly connected. This increases the allowable stroke by 2 times and eliminates the parasitic rotation of the output at the same time when the mechanism is placed in parallel [31]. When this system is mirrored over its horizontal axis as well, the parasitic translation is eliminated at the cost of internal stresses. See figure (9) for one single block and the double mirrored system.

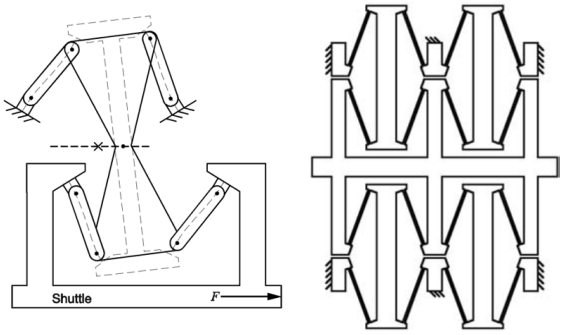

Figure 9. Straight line motion using the stacked Roberts mechanism. Left: single block and right: double mirrored layout. Figures retrieved from [31]

4.2.3 Use of the center of rotation shift

As linear mechanisms measure have a parasitic error predominantly in translation perpendicular to its desired displacement, rotational mechanisms suffer mostly from center of rotation shift. The center of rotation shift that mechanisms undergo is usually minimized as much as possible to generate a better hinge with concentrated rotation. This shift in the center of rotation can also be used towards compensation for other parasitic errors in the mechanism. Zhao et al., for example, used the parasitic motion of trapezoidal flexures to compensate for the parasitic motion of a linear motion mechanism [33]. Later Huo et al. used this same method to generate a remote center of motion mechanism(RCM) with ultra-high-precision rotation [18]. See figure (10). This comes however at the cost of in and out-of-plane support stiffness.

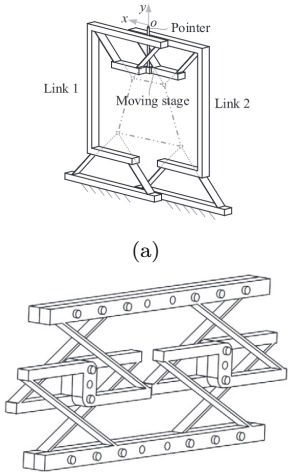

Figure 10. (a) Optimized RCM mechanism and (b) an optimized linear motion mechanism based on parasitic motion compensation. Figures retrieved from [18, 33]

4.3 Variable thickness flexures

The main limitation for constant thickness flexures is the limitation on the range of motion due to stress peaks, while a large amount of material is not used to its full stress limit. So to push the performance of these distributed flexures even further, variable thickness flexures could offer better solutions. Variable thickness leaf flexures can traverse a longer distance and handle larger input forces than a beam of the same stiffness but uniform cross-section when optimizing for a maximum strain energy density [12]. How much this increase in range of motion is however is not elaborated on. Leaf flexures optimized for the highest strain energy density thus results in geometries where the largest amount of material is maximally utilized towards load bearing. This shows lower stresses than their non-optimized counterparts. See figure (12). This method of optimizing for the highest strain energy density is used towards an optimized design for an assistive elbow orthosis. Using variable thickness on top of initially curved flexures to achieve a sinusoidal force/angle curve increases the ability to follow this curve better(1.5% instead of 2%) and at the same time increases the energy density by 277% [69].

Besides increasing the range of motion, variable thickness flexures offer other improvements in terms of accuracy. These flexures have been optimized for their use in cross flexures and it shows that they can have a more concentrated deformation while still allowing large rotations and at the same time can lower the maximum stress levels to up to 24%. These benefits do exist at the cost of a higher stiffness of the joint. [17, 51, 52]. See figure (11)

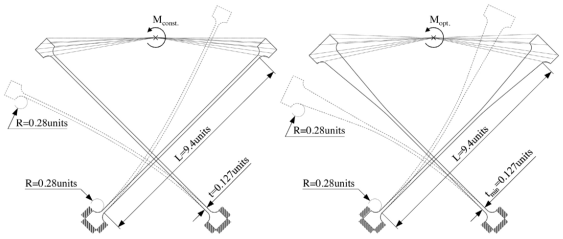

Figure 11. Model of a constant thickness cross flexure and a variable thickness flexure joint. Figure retrieved from [17]

By optimizing the configuration of these cross flexures, the center shifts can be lowered, however, some configurations yield higher center shifts [17]. This tunability can be advantageous as explained in more depth in section 4.2.3.

Another added benefit of thickness-varying flexures is their ability to deform less under axial load [51, 52]. This is advantageous in applications where a high support stiffness is necessary. Furthermore, Wu et

al. showed that with the tuning of the parameters of thickness-varying flexures, a high influence on compliance and stiffness ratios can be achieved [48]. This makes them useful to optimize desired performance for specific load cases.

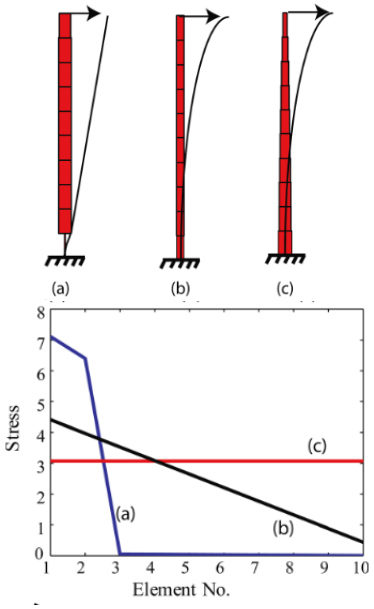

Figure 12. Comparison of three beams and their stress distribution in all elements. Figures retrieved from [12]

As discussed in this chapter, variable thickness can offer improvement in terms of a large range of motion, but how much improvement in maximum stroke up until a set maximum stress is not elaborated on directly. To fill this gap in literature a small test case was designed where a variable thickness flexure is optimized to have the same stiffness and length as a constant thickness flexure, while optimizing for maximum average stress. It shows that for a flexure of the same length and stiffness, for a fixed guided beam, the maximum deflection up until the maximum peak stress point can be increased by 40 to 46 percent. This test case is further elaborated in appendix A.1. See figure (13) for the optimized design that has the same stiffness as a 1/50 thickness-to-length ratio. This is a significant improvement compared to constant thickness flexures and more research needs to be done to uncover the full potential of variable thickness flexures.

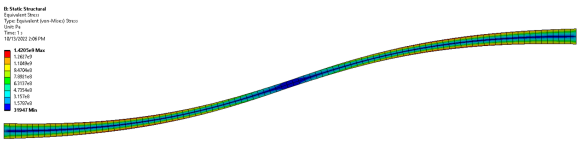

Figure 13. Optimized flexure for highest average stress to maximum stress ratio

4.4 Optimize initially curved leaf flexures

A relatively new method for designing leaf flexures is to use the advantages of initially curved flexures. The advantages these initially curved flexures pose are a relatively large range of motion and a relatively small strain range [14, 35, 54, 70, 71].

The work of Rommers also uses a novel method called the STAGE(Stress and Geometry) method to design a deformed flexure using inversed FEM to lower the stresses in the flexure during operation. This can lead to up to 23% lower peak stresses in cross-flexure joints with a range of ±45 deg [34].

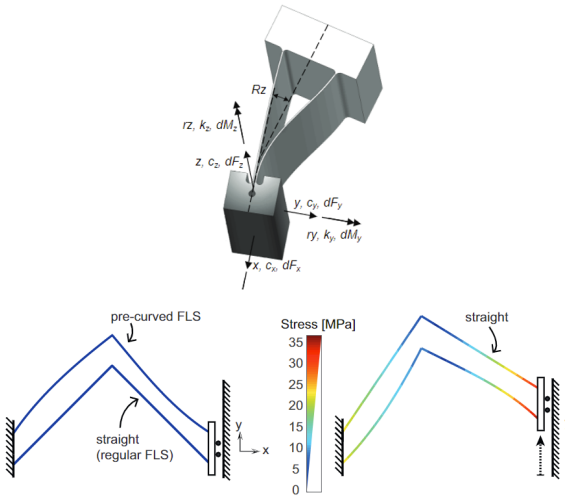

Figure 14. 2 initially curved flexure mechanisms achieving the desired geometry when deformed. Figures retrieved from [20, 34]

Another benefit could be to use the geometric non-linearities that these flexures exhibit for large deflections to our advantage. In the use of output decoupling and parasitic motion minimization, these non-linearities can be used to compensate the parasitic motions about 3.4 times better than the Roberts mechanism [15]. It is also shown in a different case study that a much more constant stiffness along the full displacement can be achieved in all directions [15]. Besides constant stiffness, to aid in the design of better rehabilitation devices, constant torque joints and constant force mechanisms have been designed using curved and thickness-varying leaf flexures [19, 36, 59, 60].

A drawback these initially curved flexures have is that they perform poorly under compressive forces [68]. This however can be compensated for. By using a set of curved leaf flexures, the drop of stiffness in the stiff directions can be compensated. One of the 2 leaf flexures will straighten when deflected resulting in a stiffer geometry in deflected configuration [15, 20, 34, 53]. See figure (14)

Another field of research looks at the ability to use systems of multiple curved and sometimes thickness varying flexures, to generate path following and force and motion converting mechanisms [14, 71–77]. This methodology of optimizing the curvature and thickness can lead to a design for a gripper that has an output force increase of 45% [14]. Another design of a gripper shows an increase of 18% in output force when taking into account variation of thickness on top of initial curvature [55]. This method is mostly used for optimizing structures to have desired mechanical properties in terms of minimum force or a maximum input/output ratio, less focus is placed on the combination of initial curvature and variable thickness towards mechanisms with a larger range of motion and minimal parasitic motions.

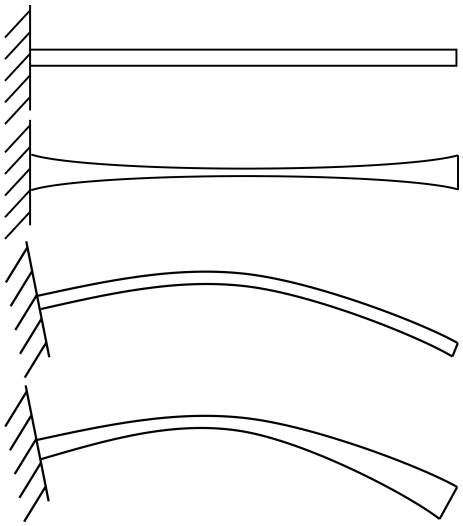

Figure 15. From top to bottom: Straight CT, Straight VT, IC CT, IC VT

All these papers look at different properties and none seem to look at the ability of the method of initial curvature and variable thickness to generate a lower parasitic motion. Meinders [15] looked at the minimization of parasitic motion but only for constant thickness flexures. Other papers as discussed above look at different aspects of their properties but none use the initial curvature and variable thickness to see what the increase in performance on the parasitic motion could be. So in a simple test case, a design is optimized for a minimal parasitic error along its trajectory for an incremental displacement in y direction to fill this gap in knowledge. The optimization is run for the 4 methods(straight constant thickness(CT), straight variable thickness(VT), initially curved(IC) CT and IC VT (See figure (15))) are compared to each other. Results show that the maximum parasitic error can be lowered by 11.5% by using IC and VT compared to a straight CT flexure(See figure (16) for the optimized design using IC and VT). See Appendix A.2 for more details.

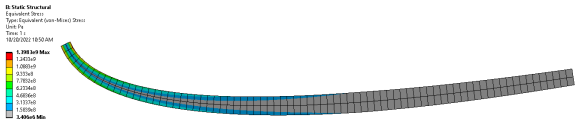

Figure 16. Optimized flexure for minimal parasitic error

5 Discussion

Looking at the current literature on the topics mentioned in chapter 4, it is clear that the research for every different method looks at a different aspect that it influences or is used towards. To generate an equal comparison seemed to involve a lot of estimating parameters. For each metric, the pitfalls will shortly be mentioned.

Looking at the range of motion of different types of mechanisms, it can be challenging to find the maximum range of motion. Most papers do not look at the maximum range of motion as an important metric. The focus lies more on small stroke but with high precision. For example, the double parallelogram mechanisms are mostly used towards its properties of minimization of parasitic motion and minimizing cross-coupling. These mechanisms are often not deflected more than tenths of millimeters, while at other times they are displaced tens of times more.

Parasitic motion is for this same reason challenging to compare. Using a dimensionless parasitic error, $\delta e_{y_{max}}/\Delta x_{max}$, the comparison is equal, however, this paper aims to look at the ability of mechanisms to have a high range of motion and at the same time look at the performance in parasitic error. As mentioned before, the double parallelogram mechanisms are often not displaced by more than 1% [2, 26, 27]. For these small relative displacements, the parasitic error is very small. It would be more interesting to see what the performance is for its maximum displacements.

Parasitic motion in the form of axis drift is especially difficult to compare. Different types of measuring the error are used in literature and often the aim is more on increasing the compliance ratio of α_z to the compliance in support directions. This is why a rating system was used.

In and out-of-plane support stiffness is another property that is often not taken into account when different methods are discussed. In-plane support stiffness is sometimes taken into account, but out-of-plane stiffness is barely touched upon in the literature. This is a very important characteristic for motion guiding with a predictable path. An educated guess can be made if only curved flexures are present in the de-

formed state, the axial and out-of-plane stiffness will most likely have dropped significantly.

6 Conclusion

The goal of this article is to give an overview of methods that can be used towards the design of high-range-of-motion mechanisms used for motion guiding with high precision and look at the support properties and the influence the methods have on those aspects.

In the comparison, rotational mechanisms are compared to each other, and separately, linear guiding mechanisms are compared to each other. For most concepts, a high range of motion seems to go hand in hand with poor support and out-of-plane stiffness. Conversely, notch-type hinges have a significantly lower range of motion but do perform better on support stiffness.

A field that is mostly undiscovered towards the means of designing mechanisms with high translations and low parasitic errors, while still having excellent support properties, are initially curved and variable thickness flexure mechanisms. Using these methods of initial curvature and variable thickness combined could offer a better-performing mechanism that performs better in every aspect at the same time making it a very interesting field of interest that can be explored further. With variable thickness, the range of motion can drastically be increased(for a simple case of a fixed-guided beam, variable thickness can increase the range of motion by $40 - 46\%$. See appendix A.1), while initial curvature can have a positive effect on parasitic performance [15] and for the combination of initial curvature and variable thickness, for a simple case of a cantilever beam, it can have a positive effect towards parasitic motion minimization of up to 11.5%(See appendix A.2 for more information)

References

[1] Philipp Gräser, Sebastian Linß, Felix Harfensteller, Mario Torres, Lena Zentner, and René Theska. "High-precision and large-stroke XY micropositioning stage based on serially arranged compliant mechanisms with flexure hinges". In: *Precision Engineering* 72 (Nov. 2021), pp. 469–479.

[2] Lei-Jie Lai, Guo-Ying Gu, and Li-Min Zhu. "Design and control of a decoupled two degree of freedom translational parallel micro-positioning stage". In: *Rev. Sci. Instrum* 83 (2012), p. 45105.

[3] Hua Liu, Shixun Fan, Xin Xie, Zhiyong Zhang, and Dapeng Fan. "Design and modeling of a novel monolithic parallel XY stage with centimeters travel range". In: *Special Issue Article Advances in Mechanical Engineering* 9.11 (2017), p. 2017.

[4] W Dong, J Tang, and Y ElDeeb. "Design of a linear-motion dual-stage actuation system for precision control". In: *Smart Mater. Struct* 18 (2009), p. 11.

[5] M. Y. Chen, C. C. Wang, and L. C. Fu. "Adaptive sliding mode controller design of a dual-axis maglev positioning system". In: *Proceedings of the American Control Conference* 5 (2001), pp. 3731–3736.

[6] Minh Tuan Pham, Tat Joo Teo, and Song Huat Yeo. "Synthesis of multiple degrees-of-freedom spatial-motion compliant parallel mechanisms with desired stiffness and dynamics characteristics". In: *Precision Engineering* 47 (Jan. 2017), pp. 131–139.

[7] Minh Tuan Pham, Song Huat Yeo, Tat Joo Teo, Pan Wang, and Mui Ling Sharon Nai. "Design and Optimization of a Three Degrees-of-Freedom Spatial Motion Compliant Parallel Mechanism With Fully Decoupled Motion Characteristics". In: (2019).

[8] Minh Tuan Pham, Song Huat Yeo, Tat Joo Teo, Pan Wang, Mui Ling, and Sharon Nai. "A Decoupled 6-DOF Compliant Parallel Mechanism with Optimized Dynamic Characteristics Using Cellular Structure". In: (2021).

[9] Minh Tuan Pham, Song Huat Yeo, and Tat Joo Teo. "Three-Legged Compliant Parallel Mechanisms: Fundamental Design Criteria to Achieve Fully Decoupled Motion Characteristics and a State-of-the-Art Review". In: (2022).

[10] Sudarshan Hegde and G. K. Ananthasuresh. "A spring-mass-lever model, stiffness and inertia maps for single-input, single-output compliant mechanisms". In: *Mechanism and Machine Theory* 58 (Dec. 2012), pp. 101–119.

[11] Yangmin Li, Shunli Xiao, Longquan Xi, and Zhigang Wu. "Design, Modeling, Control and Experiment for a 2-DOF Compliant Micro-Motion Stage". In: *International Journal of Precision Engineering and Manufacturing* 15.4 (2014), p. 735.

[12] Girish Krishnan, Charles Kim, and Sridhar Kota. "A Metric to Evaluate and Synthesize Distributed Compliant Mechanisms". In: (2013).

[13] Guangbo Hao and Jingjun Yu. "Design, modelling and analysis of a completely-decoupled XY compliant parallel manipulator". In: *Mechanism and Machine Theory* 102 (Aug. 2016), pp. 179–195.

[14] Hong Zhou and Kwun Lon Ting. "Shape and Size Synthesis of Compliant Mechanisms Using Wide Curve Theory". In: *Journal of Mechanical Design* 128.3 (May 2006), pp. 551–558.

[15] N.K. Meinders. "Compensating parasitic motions and cross-couplings in compliant mechanisms". PhD thesis. Delft: Delft University of Technology, 2021.

[16] Ning Xu, Ming Dai, and Xiaoqin Zhou. "Analysis and design of symmetric notch flexure hinges". In: *Research Article Advances in Mechanical Engineering* 9.11 (2017), p. 2017.

[17] Jon Freire Gómez, Julian D Booker, and Phil H Mellor. "2D shape optimization of leaf-type crossed flexure pivot springs for minimum stress". In: *Precision Engineering* 42 (2015), pp. 6–21.

[18] Tonglong Huo, Jingjun Yu, Hongzhe Zhao, Haoran Wu, and Yuan Zhang. "A family of novel RCM rotational compliant mechanisms based on parasitic motion compensation". In: *Mechanism and Machine Theory* 156 (Feb. 2021).

[19] Hong Zhou and Hari Nair Prakashah. *Synthesis of constant torque compliant mechanisms.* Tech. rep. 2015.

[20] D M Brouwer, J P Meijaard, and J B Jonker. "Elastic element showing low stiffness loss at large deflection". In: ().

[21] Zhiwei Zhu, Xiaoqin Zhou, Zhiwei Liu, Rongqi Wang, and Lei Zhu. "Development of a piezoelectrically actuated two-degree-of-freedom fast tool servo with decoupled motions for micro-/nanomachining". In: *Precision Engineering* 38.4 (2014), pp. 809–820.

[22] Shuai-Shuai Lu and Peng Yan. "A Stiffness Modeling Approach for Multi-Leaf Spring Mechanism Supporting Coupling Error Analysis of Nano-Stages". In: *International Journal of Precision Engineering and Manufacturing* 18.6 (2017), pp. 863–870.

[23] Guangbo Hao and Xianwen Kong. "A 3-DOF Translational Compliant Parallel Manipulator Based on Flexure Motion". In: (2012).

[24] Guangbo Hao, Xiuyun He, and Shorya Awtar. "Design and analytical model of a compact flexure mechanism for translational motion". In: *Mechanism and Machine Theory* 142 (Dec. 2019).

[25] Shorya Awtar and Alexander H Slocum. "Constraint-Based Design of Parallel Kinematic XY Flexure Mechanisms". In: (2007).

[26] Kee-Bong Choi and Doo-Hyeong Kim. "Monolithic parallel linear compliant mechanism for two axes ultraprecision linear motion". In: *Rev. Sci. Instrum* 77 (2006), p. 65106.

[27] Fujun Wang, Xiaolu Zhao, Zhichen Huo, Beichao Shi, Cunman Liang, Yanling Tian, and Dawei Zhang. "A 2-DOF nano-positioning scanner with novel compound decoupling-guiding mechanism". In: *Mechanism and Machine Theory* 155 (Jan. 2021).

[28] Jingjun Yu, Yan Xie, Zhenguo Li, and Guangbo Hao. "Design and experimental testing of an improved large-range decoupled XY compliant parallel micromanipulator". In: *Journal of Mechanisms and Robotics* 7.4 (Nov. 2015).

[29] Qingsong Xu. "New flexure parallel-kinematic micropositioning system with large workspace". In: *IEEE Transactions on Robotics* 28.2 (Apr. 2012), pp. 478–491.

[30] Qingsong Xu. "Design, testing and precision control of a novel long-stroke flexure micropositioning system". In: *Mechanism and Machine Theory* 70 (2013), pp. 209–224.

[31] Neal B Hubbard, Jonathan W Wittwer, John A Kennedy, Daniel L Wilcox, and Larry L Howell. "A novel fully compliant planar linear-motion mechanism". In: (2004).

[32] Sicong Wan and Qingsong Xu. "Design and analysis of a new compliant XY micropositioning stage based on Roberts mechanism". In: *Mechanism and Machine Theory* 95 (Jan. 2016), pp. 125–139.

[33] Hongzhe Zhao, Shusheng Bi, and Jingjun Yu. "A novel compliant linear-motion mechanism based on parasitic motion compensation". In: *Mechanism and Machine Theory* 50 (Apr. 2012), pp. 15–28.

[34] J Rommers. "Design strategies for large range flexure mechanisms". PhD thesis. Delft: Delft University of Technology, June 2022.

[35] Ke Wu, Gang Zheng, and Guangbo Hao. "Efficient spatial compliance analysis of general initially curved beams for mechanism synthesis and optimization". In: *Mechanism and Machine Theory* 162 (Aug. 2021).

[36] Qingyi Zhang, Peng Yan, and Haipeng Wang. "A curved-beam based quasi-constant force mechanism supporting large range and force-sensitive robotic manipulation". In: *Mechanism and Machine Theory* 172 (June 2022).

[37] P Merken, O Smal, J F Debongnie, and B Raucent. "Design and test of a circular notch hinge". In: ().

[38] F. De Bona and M. Gh Munteanu. "Optimized flexural hinges for compliant micromechanisms". In: *Analog Integrated Circuits and Signal Processing* 44.2 (2005), pp. 163–174.

[39] Saša Zelenika, Mircea Gh Munteanu, and Francesco De Bona. "Optimized flexural hinge shapes for microsystems and high-precision applications". In: *Mechanism and Machine Theory* 44.10 (Oct. 2009), pp. 1826–1839.

[40] Rongqi Wang, Xiaoqin Zhou, and Zhiwei Zhu. "Development of a novel sort of exponent-sine-shaped flexure hinges". In: *Review of Scientific Instruments* 84.9 (Sept. 2013).

[41] Min Liu, Jinqing Zhan, and Xianmin Zhang. "Topology optimization of distributed flexure hinges with desired performance". In: *Engineering Optimization* 52.3 (Mar. 2020), pp. 405–425.

[42] Min Liu, Jinqing Zhan, Benliang Zhu, and Xianmin Zhang. "Topology optimization of flexure hinges with a prescribed compliance matrix based on the adaptive spring model and stress constraint". In: *Precision Engineering* 72 (Nov. 2021), pp. 397–408.

[43] Lifang Qiu, Xin Yue, and Zhongtian Xie. "Design and analysis of Multicavity Flexure Hinge (MCFH) based on three-dimensional continuum topology optimization". In: *Mechanism and Machine Theory* 139 (2019), pp. 21–33.

[44] Qian Lu, Zhi Cui, and Xifu Chen. "Fuzzy multi-objective optimization for movement performance of deep-notch elliptical flexure hinges". In: *Rev. Sci. Instrum* 86 (2015), p. 65005.

[45] Nicolae Lobontiu, Jeffrey S.N. Paine, Ephrahim Garcia, and Michael Goldfarb. "Design of symmetric conic-section flexure hinges based on closed-form compliance equations". In: *Mechanism and Machine Theory* 37.5 (2002), pp. 477–498.

[46] Qiang Li, Cunyun Pan, and Xiaojun Xu. "Closed-form compliance equations for power-function-shaped flexure hinge based on unit-load method". In: *Precision Engineering* 37.1 (Jan. 2013), pp. 135–145.

[47] R. Ryan Vallance, Behnoush Haghighian, and Eric R. Marsh. "A unified geometric model for designing elastic pivots". In: *Precision Engineering* 32.4 (Oct. 2008), pp. 278–288.

[48] Jianwei Wu, Yin Zhang, Shuai Cai, and Jiwen Cui. "Modeling and analysis of conical-shaped notch flexure hinges based on NURBS". In: *Mechanism and Machine Theory* 128 (Oct. 2018), pp. 560–568.

[49] Yeong jun Choi, S. V. Sreenivasan, and Byung Jin Choi. "Kinematic design of large displacement precision XY positioning stage by using cross strip flexure joints and over-constrained mechanism". In: *Mechanism and Machine Theory* 43.6 (June 2008), pp. 724–737.

[50] Sicong Wan and Qingsong Xu. "Design of a new rotational micropositioning mechanism driven by limited-angle torque motor". In: *2015 IEEE 10th International Conference on Nano/Micro Engineered and Molecular Systems, NEMS 2015*. Institute of Electrical and Electronics Engineers Inc., July 2015, pp. 209–213.

[51] Yang Miao, Du Zhijiang, Sun Lining, and Dong Wei. "Optimal design, modeling and control of a long stroke 3-PRR compliant parallel manipulator with variable thickness flexure pivots". In: *Robotics and Computer-Integrated Manufacturing* 60 (Dec. 2019), pp. 23–33.

[52] Miao Yang, Zhijiang Du, and Wei Dong. "Design and Modeling of a Variable Thickness Flexure Pivot". In: (Feb. 2019).

[53] Steven E Boer, Ronald G K M Aarts, Dannis M Brouwer, and J Ben Jonker. "Multibody Modelling and Optimization of a Curved Hinge Flexure". In: *The 1st Joint International Conference on Multibody System Dynamics* (May 2010).

[54] Yu Jingjun, Zong Guanghua, Yu Zhiwei, and Bi Shusheng. *A new family of large-displacement flexural pivots*. Tech. rep. 2007.

[55] Chao-Chieh Lan and Yung-Jen Cheng. "Chao-Chieh Lan 1 Distributed Shape Optimization of Compliant Mechanisms Using Intrinsic Functions". In: (2008).

[56] Horacio Ahuett-Garza, Oscar Chaides, Pedro N. Garcia, and Pedro Urbina. "Studies about the use of semicircular beams as hinges in large deflection planar compliant mechanisms". In: *Precision Engineering* 38.4 (2014), pp. 711–727.

[57] S. Serafino, P. Fanghella, and M. Verotti. "Initial curvature and centroid positioning effects on cross-axis flexural pivots accuracy". In: *Mechanism and Machine Theory* 177 (Nov. 2022).

[58] M. Verotti. "Effect of initial curvature in uniform flexures on position accuracy". In: *Mechanism and Machine Theory* 119 (Jan. 2018), pp. 106–118.

[59] Hari Nair Prakashah and Hong Zhou. "Synthesis of Constant Torque Compliant Mechanisms". In: (2016).

[60] Ivan A Parinov, Shun-Hsyung Chang, and Banh Tien Long. "Springer Proceedings in Materials". In: (2019).

[61] Min Liu, Xianmin Zhang, and Sergej Fatikow. "Design and analysis of a high-accuracy flexure hinge". In: *Review of Scientific Instruments* 87.5 (May 2016), p. 055106.

[62] Shenyuan Dai, Chongxiang Li, Yue Yu, and Lifang Qiu. *View of Computer-Aided Optimal Design and Analysis of Symmetric Single-Axis Flexure Hinges*. Feb. 2022.

[63] S. Koppen, M. Langelaar, and F. van Keulen. "A simple and versatile topology optimization formulation for flexure synthesis". In: *Mechanism and Machine Theory* 172 (June 2022).

[64] Pei Xu, Yu Jingjun, Zong Guanghua, Bi Shusheng, and Yu Zhiwei. "Analysis of rotational precision for and isosceles-trapezoidal flexural pivot". In: *Journal of Mechanical Design, Transactions of the ASME* 130.5 (May 2008).

[65] Fulei Ma and Guimin Chen. "Bi-BCM: A Closed-Form Solution for Fixed-Guided Beams in Compliant Mechanisms". In: (2017).

[66] Robert M Panas and Jonathan B Hopkins. "Eliminating Underconstraint in Double Parallelogram Flexure Mechanisms". In: (2015).

[67] J B Hopkins and R M Panas. *A Family of Flexures That Eliminate Underconstraint in Nested Large-Stroke Flexure Systems*. Tech. rep. 2013.

[68] Alexandre E Guérinot, Spencer P Magleby, Larry L Howell, and Robert H Todd. "Compliant Joint Design Principles for High Compressive Load Situations". In: (2005).

[69] Martin Tschiersky, Edsko E G Hekman, Dannis M Brouwer, and Just L Herder. "Gravity Balancing Flexure Springs for an Assistive Elbow Orthosis". In: *IEEE TRANSACTIONS ON MEDICAL ROBOTICS AND BIONICS* 1.3 (2019).

[70] Hong Zhou and Nisar Ahmed. *Synthesis of path generation compliant mechanisms using variable width spline curves*. Tech. rep. 2014.

[71] Ashok Kumar Rai, Anupam Saxena, and Nilesh D Mankame. "Synthesis of Path Generating Compliant Mechanisms Using Initially Curved Frame Elements". In: (2007).

[72] Hong Zhou. "Geometric Modeling and Optimization of Multimaterial Compliant Mechanisms Using Multilayer Wide Curves". In: (2008).

[73] Hong Zhou and Kwun-Lon Ting. *Geometric optimization of spatial multimaterial compliant mechanisms and structures using three-dimensional multilayer wide curves*. Tech. rep. 2009.

[74] Hong Zhou, Azher Hussain, and Naser Mohammed. *Compliant mechanism synthesis using degree of genus and variable width curves*. Tech. rep. 2014.

[75] Dong Xu and G. K. Ananthasuresh. "Freeform Skeletal Shape Optimization of Compliant Mechanisms". In: *Journal of Mechanical Design* 125.2 (June 2003), pp. 253–261.

[76] J A Hetrick and S Kota. "An Energy Formulation for Parametric Size and Shape Optimization of Compliant Mechanisms". In: (1999).

[77] Mehdi Mokhtari, Seyyed Mojtaba Varedi-Koulaei, Jiaxiang Zhu, and Guangbo Hao. "Topology optimization of the compliant mechanisms considering curved beam elements using metaheuristic algorithms". In: *Original Research Article Proc IMechE Part C: J Mechanical Engineering Science* 2022.13 (2019), pp. 7197–7208.

[78] JPE. *Beam theory: Bending*. `https://www.jpe-innovations.com/precision-point/beam-theory-bending/`. July 2020.

A Test cases

Varying the thickness of leaf flexures can be a very useful way to increase performance in multiple fields. By choosing the shape carefully you can increase the amount of material that is maximally utilized towards load bearing [12]. Freire Gómez et al. and Krishnan et al. used thickness-varying leaf flexures to minimize stress peaks and to extend the working range of compliant mechanisms [12, 17]. Miao et al. talk about the ability of varying thickness leaf flexures to have a lower parasitic motion due to the deformation of the leaf flexures being more concentrated near the rotation center of the cross flexure [51]. This ability to have an influence on the center of rotation shift and parasitic motion is however not researched for single, thickness-varying, leaf flexures.

Another promising technology is using initially curved flexures as presented in [15]. The nonlinearities can help counter parasitic motions for large translations. Using pre-curved flexures can also increase the supporting stiffnesses for the full range of motion [20, 34, 53].

To see what the 2 methods influence and what the influence is if both of the methods are combined, a few use cases for optimizing different aspects of leaf flexures are conducted. The first test case looks at the influence of variable thickness on the range of motion and the second case is conducted for all four methods: Constant thickness(CT), Variable thickness(VT), Constant thickness flexures that are initially curved and lastly a combination of the 2, VT flexures that are initially curved.

A.1 Optimize leaf spring for maximum stroke

As using variable thickness leaf flexures can reduce stress levels in cross flexures [17, 51], this might result in flexures that have the same length and stiffness while allowing larger displacements before reaching a predefined maximum stress level. Krishnan et al. do mention the ability to increase the range but do not elaborate on how much the range is increased, so to fill this gap this test case is designed [12].

To generate a beam that has the same mechanical properties as a constant thickness one, we first need to find the properties of a constant thickness beam. As linear guiding is the most important property, the beam is fixed on one end and can translate in x and y, but rotation is fixed to 0. The endpoint is displaced in y and the reaction force is measured. See figure (A.1)

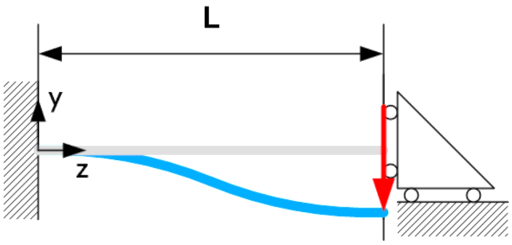

Figure A.1. Boundary conditions for the test case. Figure retrieved from [78]

Now a new flexure that has a variable thickness can be designed by optimizing for the same resultant force for the input stroke, while also maximizing the ratio of average stress over the edges of the flexure to the maximum stress occurring somewhere along the surface(see equation (A.1) for the optimization problem). The hypothesis is that this way the largest amount of material is optimally used. See figure (A.4) for the parameters optimized for.

$$\begin{aligned} max. \quad & \frac{\sigma_{ave}}{\sigma_{max}} \\ \text{s.t.} \quad & \sigma_{max} - \sigma_{ref} < 0 \\ & |F_{reaction} - F_{target}| \quad < \quad 0.01 \cdot F_{target} \end{aligned} \tag{A.1}$$

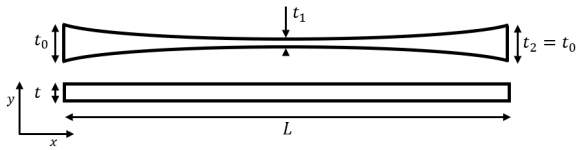

Figure A.2. Parameters optimized for the VT flexure and the constant thickness flexure

Lastly, the constant thickness flexure and the new optimized flexure are displaced until the maximum stress reaches a set stress limit and the deflection is measured.

This is done for 3 thickness-to-length ratios, namely 1/20, 1/50 and 1/100. The results are listed in table (A.1) and show that the stroke can be increased by at least 40% by using a variable thickness flexure. The optimized design in deformed shape for 1/50 is shown in figure (A.3). The length L is fixed for every case and set to 100 [mm] and the maximum stress σ_{max} is set to 1.40 [GPa].

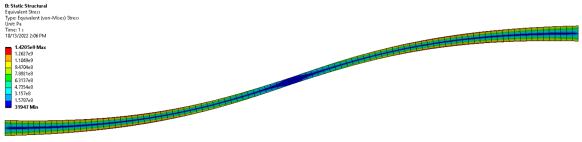

Figure A.3. Optimized flexure for highest average stress to maximum stress ratio

Table A.1. Difference in maximum stroke, for different t/L ratios, between CT and VT flexures

	1/20		1/50		1/100	
	y_{max} [mm]	Δ_y [%]	y_{max} [mm]	Δ_y [%]	y_{max} [mm]	Δ_y [%]
CT	4.66		11.33		22.88	
VT	6.69	43.5	16.54	46.0	32.12	40.4

A.2 Minimizing parasitic motion for the same stroke

As the use of initially curved flexures is not a new method for designing mechanisms, it is frequently not used in the context of high precision, low parasitic motion, mechanisms. Meinders N did show in his work that the use of constant thickness initially curved flexures can have a positive effect towards low parasitic error mechanisms [15]. This work is done for mechanisms for multiple flexures, but an interesting comparison can be made by looking at a simple single flexure and the ability to compensate for its shortening effect. With the shortening effect, the parasitic motion is depicted in figure (4). For a cantilever beam, this shortening effect is the parasitic motion in x direction.

To look at the ability to minimize parasitic motion using the non-linear effects that the methods: variable thickness and initially curved influence, a second case study was run to optimize designs for the lowest deviation of a straight path. The flexures have the same length and the same incremental displacement applied. For every load step, the parasitic error is reported and their squares are summed up to define the objective function. See equation (A.2)

$$Obj = \sum_{n=1}^{10} (\delta e_x^n)^2 \tag{A.2}$$

Besides the Obj function, a constraint was set on a maximum of 1% deviation in reaction force and a constraint was set on a maximum stress level.

$$\begin{aligned} \text{min.} \quad & Obj \\ \text{s.t.} \quad & \sigma_{max} - \sigma_{ref} < 0 \\ & |F_{reaction} - F_{target}| \quad < \quad 0.01 \cdot F_{target} \end{aligned} \tag{A.3}$$

To compare different flexures equally, the length is fixed to $L = 50$ [mm] and the reaction force on the end of the displacement, at $y^{n=10} = 5$ [mm], is constrained to 5000 [N](This is a 2D simulation, with the virtual thickness set to 1 m). For the 4 different cases, different parameters are optimized, see figure (A.4) and (A.5). As can be seen, the angle α is also included as an optimization parameter, so that the beam can lengthen before shortening to minimize the parasitic motion, because if a constant thickness flexure is optimized for this case, alpha can have a great influence on maximum parasitic error.

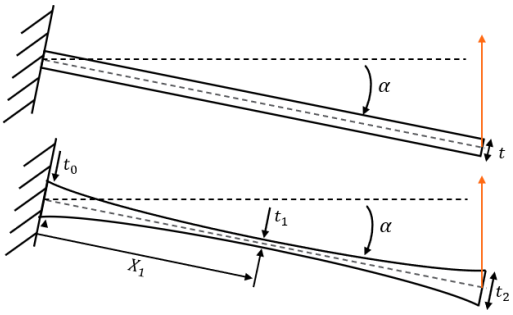

Figure A.4. Parameters optimized for the straight flexures

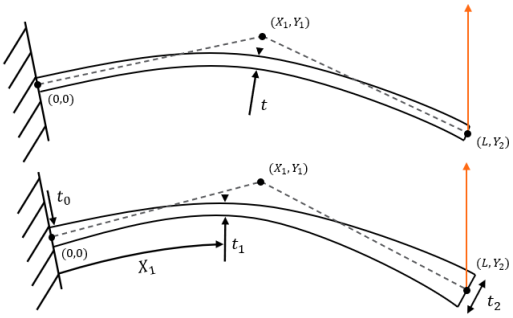

Figure A.5. Parameters optimized for the IC flexures

The results are stated in table (A.2) and it is clear that the VT has the most influential impact on the objective function. This objective is the sum of the squared parasitic errors, however, the maximum parasitic motion might be more meaningful in the design of mechanisms. These results are stated in table (A.3)

Table A.2. Minimized parasitic motion Objective function values

	Straight $\times 10^{-8}$ [m^2]		IC $\times 10^{-8}$ [m^2]	
CT	1.41		1.30	-7.9%
VT	1.18	-16.2%	1.11	-21.4%

Table A.3. Maximum parasitic error $\delta e_{x_{max}}$

	Straight $\times 10^{-5}$ [m]		IC $\times 10^{-5}$ [m]	
CT	6.67		6.45	-3.4%
VT	6.32	-5.3%	5.91	-11.5%

Looking at the results, a clear increase in parasitic performance is obtained for all methods compared to CT straight flexures, with a maximum decrease

of 11.5% in maximal parasitic error. This design is shown in figure (A.6). Looking at the design, you can see that the new design most likely performs worse for axial and out-of-plane support. This is however out of the scope of this test case, but as discussed in chapter 4.4, this can be compensated for by using multiple flexures.

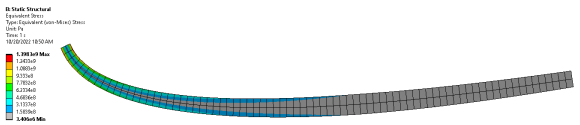

Figure A.6. Optimized flexure for minimal parasitic error using IC and VT

The paths followed by the endpoint of the beams are shown in figure (A.7). You see that the characteristic motion is more or less a circular arc, however, using the VT and IC the radius seems to increase, making the maximum error lower.

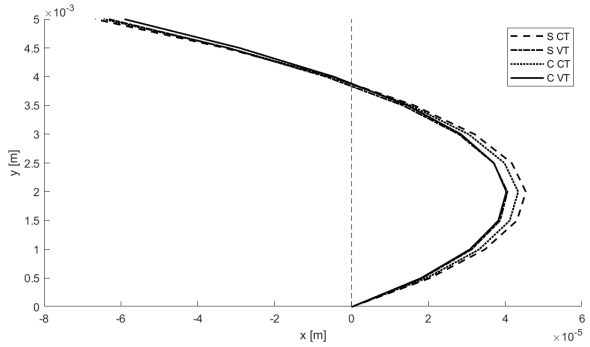

Figure A.7. Optimized flexure paths

To make the most equal comparison, a set stiffness was also optimized for, however disregarding this for the VT flexures and optimizing only for path following resulted in even better mechanisms. For the straight VT flexure, the optimized geometry has a decrease in the objective of 14% compared to the force-bounded variant. The maximum parasitic motion is 14% lower than the original straight CT flexure, this all at the cost of a significant difference in stiffness. The reaction force is lowered by 84%.

The results of the IC VT optimization, not taking stiffness into account, also show significant improvements in performance. The decrease in the objective function is 11% and the maximum parasitic motion is 16% lower than the original straight CT flexure. The reaction force is also significantly lower, 85% of what the IC VT previously showed.

2

Project proposal

The aim for this literature survey was to find methods to generate compliant mechanisms for large ranges of motion with improved parasitic properties and increased support stiffness characteristics. Two strategies show great potential in this field. Variable thickness flexures show great potential to increase support stiffness when deflected subject to stress constraints and additionally changing the thickness profile can decrease the maximum stress levels making them useful if stress is critical or an increased range of motion is desired. Secondly, initially curved flexure mechanism show a great potential to decrease parasitic error for large deflections and show the ability to increase the support stiffness when deflected.

Compliant mechanisms show a great ability to be used in many application fields for high precision and great deterministic behaviour. Besides micron ranges for precision stages, compliant mechanisms pose bigger difficulties as significant parasitic motion, limited range of motion due to stress limits and support stiffness issues. If these problems could somehow be mitigated, the use of compliant mechanisms could grow to an even greater field of applications where for example, now air bearings are used. In vacuum environments this is even more complex and expensive and magnetic levitation becomes a solution, however these solutions are complex and expensive and can be prevented if these aforementioned issues can be solved.

Towards this goal, in this thesis, it is proposed to investigate the influence of variable thickness flexures and come up with a new shape function that can be used to optimize the thickness profile for straight flexures. To show the potential of this method, multiple cases will be optimized for. Secondly, as initially curved flexures show great potential when optimized for low parasitic error, this method is further explored for different objectives and afterwards, the two combinations will be combined to generate ever better performing flexure mechanisms.

3

Paper I: Variable thickness flexures for increased support stiffness and lowered peak stress

Highlights

Variable thickness flexures for increased support stiffness and lowered peak stress

F.W.F. Colin

- 2 novel variable thickness parametrizations using quadratic and cubic bezier curves to be able to generate variable thickness flexures from noth-type hinges to fully distributed flexures.
- An increase in support stiffness ratio, C_x/C_{x0}, of 114% using variable thickness compared to a constant thickness flexure for same length and same stroke.
- An increase in support stiffness when deflected, C_x, of 125% for a same length, same stroke and same drive stiffness flexure compared to a constant thickness flexure.
- A decrease in maximum stress of 31% using variable thickness compared to a same length, same stroke and same drive stiffness flexure compared to a constant thickness flexure.

Variable thickness flexures for increased support stiffness and lowered peak stress

F.W.F. Colin [1]

[1] *Department of Precision and Microsystems Engineering, Faculty of 3mE, Delft University of Technology, Delft, the Netherlands*

ARTICLE INFO

Keywords:
Support stiffness
Stiffness ratio
Range of motion
Stress minimization
Compliant mechanism
Flexure optimization

Abstract

Flexure mechanisms have gained popularity as a viable alternative to conventional mechanical systems due to their high precision, lack of friction and lubrication-free operation. However, the limited range of motion caused by stress peaks and the significant reduction in support stiffness when deflected are two primary concerns in the application of flexure mechanisms. Typically, these flexures are designed with a constant thickness, sometimes incorporating a partially rigid section in the middle to improve support stiffness at the expense of a reduced range of motion. In this study, we propose two new variable thickness parametrizations for flexure mechanisms and optimize them for three cases. In the first case, the support stiffness ratio is optimized. In the second case, the support stiffness is maximized when deflected with a constant drive stiffness. In the third case, the maximum stress is minimized with the same drive stiffness. The results indicate that variable thickness flexures outperform constant thickness leaf flexures in all cases. In case 1 and 3, the variable thickness flexures perform identically with an increase in support stiffness ratio of 114% and a decrease in maximum stress of 31%. The variable thickness flexure with a partially rigid midsection exhibits the best performance in case 2, achieving an increase in support stiffness when deflected of 125%, compared to 100% for a fully distributed variable thickness flexure.

1 Introduction

Compliant mechanisms become more and more important in precision mechanisms in different fields like micro-manufacturing, optical fiber alignment, biological engineering and scanning probe microscopy [1]. High-precision motion stages in the field of lithography have an increasing need for larger ranges of motion. Given the lack of friction, lack of lubrication needs and nearly flawless repeatability, compliant mechanisms are the ideal fit [1–3].

A commonly used mechanism is the parallel leaf spring flexure. Parallel flexure mechanisms have an approximate straight line motion for small displacements. These mechanisms are used for example in the use of precision coordinate measurement machines [4], Hao and Yu used this mechanism for a compliant xy manipulator [5], Hao and Kong used this in the design for a self-adaptive compliant parallel gripper for high-precision manipulation [6]. When stacked and mirrored, a double parallel leaf spring flexure is achieved where the parasitic motion of the intermediate body cancels that of the output body. This double parallelogram mechanism is widely used in 2-degree-of-freedom positioning stages for its excellent properties in minimizing parasitic motion and output decoupling [3, 7–9].

These double parallelogram mechanisms allow for translations with high repeatability, however, the range of motion is constrained by the material characteristics, particularly the maximum permitted stress concentrations [1–3]. Besides the stress concentrations, the drop in support stiffness (C_x as seen in figure 3) when deflected limits the precision that can be obtained [10, 11]. Approximations for the stiffness in support directions and drive force have been provided by van Eijk [12]. In these approximations, the displacement in u is described and constrained. This results in infinite external parallel drive stiffness. Brouwer, Meijaard and Jonker proposed a FEM-based approximation [10]. In this research, the influence of parallel drive stiffness is also taken into account.

A method to increase support stiffness is to make use of partially reinforced leaf flexures. Here the part that undergoes the least bending and stress is made significantly stiffer to increase the support stiffness [12]. Minimizing the length of these flexures results in notch-type flexure hinges. These joints may be susceptible to high stress concentrations and, as a result, have a low fatigue life [11, 13]. Notch hinges have been optimized using a variety of shapes [14–17], frequently employing topology optimization [18, 19]. As notch flexures are normally employed for small ranges of motion, this research does not address the subject of flexure joints for large motion ranges, which

typically include long and narrow leaf springs and deformed shapes having a massive influence on the deflected support stiffness.

Another way to improve flexure performance is by using variable thickness (VT) flexures. Krishnan, Kim and Kota optimized flexures with VT to maximize the percentage of the material volume that is maximally utilized toward load bearing. For a VT cantilever beam with the same drive stiffness, a near-constant stress level can be obtained which reduces the peak stress by approximately 30% [13]. To increase support stiffness, Freire Gómez, Booker and Mellor optimized variable thickness flexures in a crossed flexure pivot to reduce the maximum stress up to 24% [20].

Increasing support stiffness usually comes at the cost of increased stress or decreased range of motion. This could be a limiting factor in the choice of compliant mechanisms. As the parallelogram mechanisms are the most widely used compliant mechanisms, an increase in support stiffness drop or an increase in support stiffness for the same range of motion could benefit a lot of designs in a lot of fields and this leads to the objective of this research.

In this research, the improvement using variable thickness flexures will be investigated towards the increase in support stiffness and a decrease in maximum stress, for same range of motion flexures. This will be done for a partially reinforced flexure and a fully distributed flexure using 2 novel thickness parametrizations.

The structure of this paper is as follows. In section 2, more background will be given on the ideal theoretical thickness profile. In section 3, the method and case studies are introduced. Afterward, the results of these case studies are presented in section 4. Lastly, the findings are discussed in section 5 and conclusions are drawn in section 6.

2 Background

2.1 Ideal thickness for constant stress

Take the end-loaded cantilever beam with rectangular cross-section, thickness ($t(x)$) and uniform out-of-plane thickness (h) into consideration. The moment produced by the end load (F) changes linearly with distance from the force application point.

$$\sigma = \frac{F \cdot x \cdot t(x)}{2I(x)} = \frac{6F \cdot x}{t(x)^2 h} \tag{1}$$

For a constant stress, the expression for $t(x)$ is as follows:

$$t(x) = \sqrt{\frac{6Fx}{\sigma h}} \tag{2}$$

This denotes a parabolic relation between thickness and length. Krishnan et al. [13] showed that when comparing a flexural hinge with lumped compliance at its joint, a constant thickness distributed flexure and a parabolic tapered beam, all with the same stiffness and length, the maximum stress of the parabolic tapered beam is lowest and constant, while the stress in the lumped compliant hinge is highest.

In this research, cubic bezier curves are used to parameterize the thickness profile of the flexures. These curves are used as they only need 4 control points thus minimizing the number of parameters used in the optimization. To see how close a cubic bezier can approach the ideal thickness as stated in equation (2), a small optimization on the control points is done. More on this in appendix A.1. The effectiveness of creating a constant stress flexure is limited by the minimum allowable thickness of the flexure as the end of the flexure must be parallel with the mid-line as this flexure is mirrored.

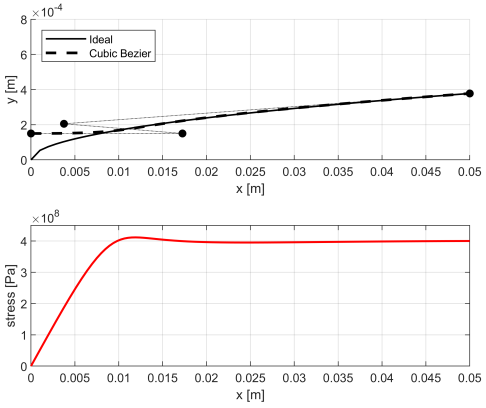

Figure 1. Approximation of the ideal thickness profile for constant stress using a cubic bezier curve. Thickness is thickness from the mid-line, so the full flexure is twice the thickness.

As can be seen in figure 1, a good approximation can be made by using a cubic bezier curve resulting in a near-constant stress profile for as much of the flexure.

3 Method and Case Studies

3.1 Definitions

The undeflected support stiffness, C_{x_0}, is defined as the stiffness in x-direction when undeflected (load step 1). The deflected support stiffness, C_x, is defined as the stiffness in x-direction when deflected (load step 3). The drive stiffness, C_u, is the stiffness in the compliant direction so in u-direction. See figure 3

3.2 Parametrization

Two variable thickness shape functions are defined. The first shape function uses a quadratic bezier at the end and at the base, acting as a fillet to the rigid world and uses 2 cubic bezier curves as the majority of the thickness profile. Using cubic bezier curves, the tangency at the endpoints is defined by the line between the last control point to the endpoint. To ensure a tangency of 0 in the middle, the last control point ($\mathbf{P}_{C2}$ is placed at the same y location as $\mathbf{P}_2$, the same holds for $\mathbf{P}_{C3}$. This ensures a smooth transition in the symmetric flexure between the two cubic bezier curves. This parametrization uses 15 parameters, but only 8 need to be optimized for the symmetric load case. The parameterization is visualized in appendix A.2 figure A.1.

The second shape function parameterizes the thickness profile of the flexure that is part of a partially rigid flexure. One of the parameters is the length of the flexure part, so the parameterization can make something from resembling a notch to a flexure with a minimal rigid part in the middle, thus fully distributed. This flexure is then mirrored and the rigid bodies are connected to form the full flexure.

This shape function uses 2 quadratic bezier curves to define the fillets to the fixed world and on the end to the rigid body. In the center, one cubic bezier curve is used that makes up the majority of the length of the flexure. The end of this flexure is rigidly connected to a beam element with a thickness of 10 mm to the point where the displacement is applied at the exact midpoint ($x = 50\,\text{mm}$). This parametrization uses 13 parameters. See appendix A.2 figure A.2.

For both flexures, the minimum thickness is set to 0.3 mm, this thickness is chosen as it is as thin as possible while still predictably producible with wire EDM.

3.3 Load case

The flexure length is 100 mm with a fixed rotation and free translation in x on its end. The simulation with an added partially rigid body is evaluated by only simulating one half and releasing the rotation. This load case is in fact the same as for a fixed-guided flexure, as the moment distribution is equal. From the end of the flexure, a rigid connection is made to a remote point 50 mm from the base. To get stiffness results for the full flexure, the stiffness must be divided by 2. The boundary conditions for these 2 simulations are visualized in figure 2.

The load steps are explained below and visualized in figure 3.

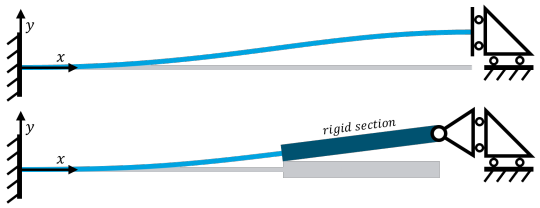

Figure 2. Boundary conditions for the top: fully distributed flexure and bottom: half of the full flexure incorporating a rigid section.

Load step 1: A dummy load of 10 N is applied in negative x-direction and the deflection δ_x is measured to calculate the C_{x_0}.

Load step 2: The x load is released and a deflection in y-direction called u of 10 mm is applied. The stress is measured and included in the constraints to keep the maximum stress of the optimized design below a certain level.

Load step 3: The y-displacement is maintained and a dummy load of 10 N is applied in negative x-direction to measure the C_x.

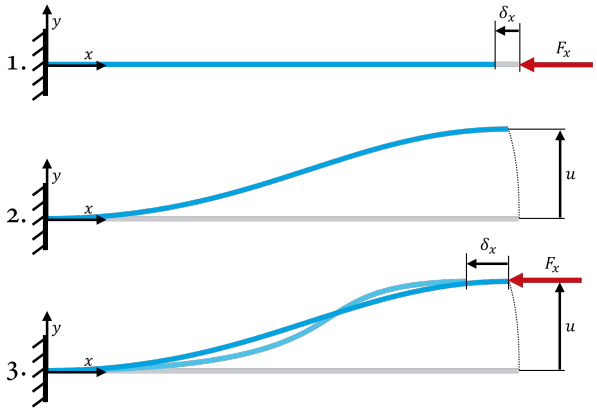

Figure 3. Load case visualized for distributed flexure.

3.4 Software

A custom mesher in python in combination with pyMAPDL [21], a python package that allows for direct communication with an instance of an Ansys solver via APDL scripting in python, is used to minimize the simulation time per design iteration. This allows for significant time reduction preventing the need for overhead software and license loading pending time.

3.5 Meshing

To ensure a fair and consistent comparison of a large number of design iterations, a robust and consistent mesher is essential. When using quad elements, peak stresses may occur within oddly shaped elements, especially when branching from one to two elements.

Therefore, the mesher creates a series of nearly 1:1 shaped elements on the outer edges, where the highest stresses are expected to occur, to make each iteration as comparable as possible. The mesher generates quadratic 2D "PLANE183" elements, set to a plane strain condition, with four elements in the thickness of the flexure. The "PLANE183" element is capable of plasticity, hyperelasticity, creep, stress stiffening, large deflection and large strain, as specified in [22].

3.6 Assumptions

Some assumptions are made in the design of the mechanisms. These are as follows:

(1) Stress is constant in z-direction if extruded
(2) 2D geometries are used
(3) Material is uniform
(4) The flexure is free of internal stresses

3.7 Optimization Algorithm

Matlab's surrogateopt algorithm is used [23]. This algorithm is suitable for computationally expensive objective functions as it uses the surrogate model to approximate the response of the system by interpolating a radial basis function between random sampling points. After a set amount of random sampling points between the bounds, the algorithm switches to the second phase. In phase 2 the algorithm searches for a minimum by sampling thousands of points on the surrogate model, the best point is then evaluated and the objective value is then used to update the surrogate model. This step continues until a minimum is found. When this minimum is found, the algorithm switches back to phase 1 and constructs a new surrogate.

3.8 Case studies introduction

Three case studies were investigated, the first case looks at the ability to improve the support stiffness ratio (C_x/C_{x0}) for flexures with the same stroke as a constant thickness flexure. Case 2 looks at the possible increase in support stiffness when deflected for a flexure with the same C_u. The last case investigates the ability to decrease the maximum stress in the flexure compared to the constant thickness flexure with the same stroke and the same C_u.

(1) Maximize support stiffness ratio
(2) Maximize support stiffness when deflected with the same drive stiffness
(3) Minimize stress with the same drive stiffness

3.9 Constraints

Stress constraint (Case 1): To constrain the maximum stress when deflected, the following constraint is used. This constraint is used for every set of nodes on every one of the 4 bezier curves with the maximum allowable stress σ_{limit}. A value of 400 MPa is set as σ_{limit} for Stavax.

$$\frac{max(\boldsymbol{\sigma}_{bezier}) - \sigma_{limit}}{\sigma_{limit}} \leq 0 \tag{3}$$

Base and end stress constraints (Case 1 & 2): In a flexure, the point of connection to rigid bodies is typically the most critical due to the highest moment occurring for a cantilever beam. This area is prone to stress concentration, particularly when transitioning from a compliant to a rigid structure. To address this issue, a stress constraint is imposed on the base and end of the flexure to maintain stress levels below 100 MPa, 4 times lower than the maximum allowable stress. The constraints used for σ_{base} and σ_{end} are as follows.

$$\frac{\sigma_{base} - 100\,\text{MPa}}{100\,\text{MPa}} \leq 0 \tag{4}$$

$$\frac{\sigma_{end} - 100\,\text{MPa}}{100\,\text{MPa}} \leq 0 \tag{5}$$

Drive stiffness constraint (Case 2): To define the drive stiffness, the reaction force is constrained, as the deflection is equal. As the length of the flexures and the thickness of the flexures tends to decrease when increasing the support stiffness, the drive stiffness decreases when optimizing for support stiffness. To prevent the drive stiffness to decrease, the following constraint is implemented where $F_{y,Ref}$ is the minimum reaction force.

$$\frac{F_{y,Ref} - F_y}{F_{y,Ref}} \leq 0 \tag{6}$$

3.10 Objective function

For the 3 cases, the following objective values are defined that need to be minimized subject to the constraints. The first two cases look at increasing the support stiffness when deflected and the third case looks to minimize the stress for the same drive stiffness.

Case 1

$$minimize \quad Obj = -C_x/C_{x_0} \tag{7}$$

Case 2

$$minimize \quad Obj = -C_x \tag{8}$$

Case 3

$$minimize \quad Obj = \sigma_{max} \tag{9}$$

3.11 Material properties

The material used in the optimization is Stavax ESR [24]. This is a medium carbon martensitic stainless steel with high corrosion resistance and low wear. The material properties can be found in table 1.

Table 1. Material properties of Stavax

Young's modulus	[GPa]	200
ultimiate tensile strenght	[GPa]	1.4
Poisson's ratio	[-]	0.3
density	[kg m^{-3}]	7800

To achieve infinite cycles a maximum stress limit of 400 MPa is used. With a maximum stress of 400 MPa and an amplitude stress of 200 MPa, an infinite life cycle safety factor of about 3 is achieved. This is calculated using the modified Goodman diagram [25].

4 Results

In this section, the results of the optimization problems are elaborated for the 3 test cases. The final optimized parameter values can be found in table A.1 and A.2 in appendix A.3.

4.1 Case 1: Maximize support stiffness ratio

Four cases were examined to maximize the stiffness ratio in the presence of infinite external parallel drive stiffness. The first step involved setting a baseline by optimizing a constant thickness flexure with a displacement of $L/10$ for maximum stiffness ratio (C_x/C_{x_0}), subject to stress constraints. Subsequently, the same optimization procedure was carried out for a fully distributed VT flexure, a partially rigid case with CT flexures and finally, a hybrid case that utilized VT and incorporated a partially rigid midsection.

The optimized flexures can be seen in figure 4 and their properties in table 2. A trend of decreasing the length of the flexure and increasing the thickness in the middle can be observed.

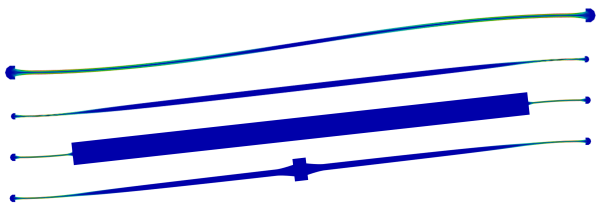

Figure 4. From top to bottom: Baseline, VT, Partially rigid CT, Partially rigid VT.

As can be seen in table 2, all cases perform better than the baseline, with an improvement of 60% for a partially rigid CT flexure and an improvement of 114% for the fully distributed and hybrid VT flexures.

Table 2. Properties of the Baseline, Hybrid CT, Hybrid VT and distributed flexures optimized for largest C_x/C_{x_0} ratio. The improvement in ratio compared to the baseline is depicted in bold numbers.

		Baseline	Distr. VT	Hybrid CT	Hybrid VT
C_{x_0}	[N/m]	1.50E9	1.43E9	2.95E9	1.46E9
C_x	[N/m]	3.15E8	6.42E8	9.92E8	6.57E9
C_x/C_{x_0}	[-]	21%	45%	34%	45%
Impr.	[-]	-	**114%**	**60%**	**114%**
F_u	[N]	760.3	144.3	173.1	142.7
σ_{max}	[Pa]	4.00E8	4.00E8	4.00E8	4.00E8

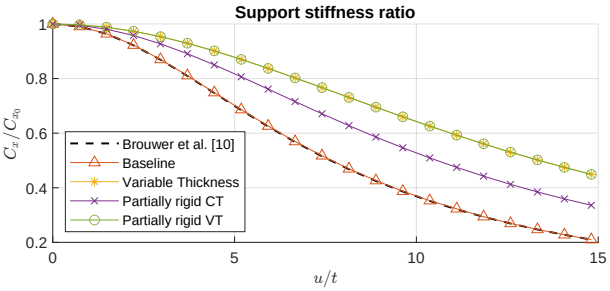

Figure 5. Support stiffness ratio over deflection comparison for the 4 cases.

These optimized designs are also used to plot the u/t graph as seen in the research of Brouwer, Meijaard and Jonker [10]. Here, since we optimize for the same stroke, the t value of the baseline is used for the other optimized flexures. As can be seen in figure 5, the VT flexures indeed have a better stiffness ratio over the whole stroke as the baseline and the partially rigid CT flexure.

4.2 Case 2: Maximize support stiffness for same drive stiffness

Four cases were analyzed to maximize the support stiffness when deflected for same stroke flexures with the same drive stiffness. Firstly a baseline is set. A constant thickness flexure with a displacement u of $L/10$ is optimized for maximum support stiffness with the same drive stiffness as the baseline of case 1, subject to stress constraints. After this, the same optimization is done for a fully distributed VT flexure, a partially rigid case with CT flexures and lastly a hybrid case that utilizes VT and incorporates a partially rigid midsection.

The optimized flexures can be seen in figure 6 and their properties can be found in table 3. As can be seen, all cases perform better than the baseline, with an improvement of 100% for a distributed VT flexure and an improvement of 125% for the hybrid VT flexure.

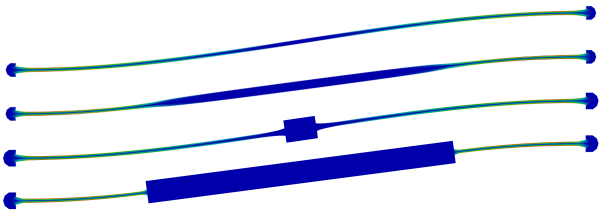

Figure 6. From top to bottom: Baseline, VT, Partially rigid CT, Partially rigid VT

Table 3. Properties of the Baseline, Hybrid CT, Hybrid VT and distributed flexures optimized for largest support stiffness. The improvement in ratio compared to the baseline is depicted in bold numbers.

		Baseline	Distr. VT	Hybrid CT	Hybrid VT
C_{x_0}	[N/m]	1.50E9	1.99E9	1.58E9	2.78E9
C_x	[N/m]	3.15E8	6.31E8	3.19E8	7.09E8
Impr.	[-]	-	**100%**	**1%**	**125%**
C_x/C_{x_0}	[-]	21%	32%	20%	26%
F_u	[N]	760.3	761.0	761.7	763.1
σ_{max}	[Pa]	4.00E8	4.00E8	4.00E8	4.00E8

As can be observed in table 3, the C_x is almost identical for the partially rigid CT flexure compared to the partially rigid CT flexure from Case 1. This is because the extra length is necessary to increase the drive stiffness to the constrained value.

4.3 Case 3: Minimize peak stress for same drive stiffness

Flexures are commonly prone to stress peaks limiting their range of motion and defining their design safety factor. To increase the range of motion or to increase the design safety factor, lower stress for the same deflection is required. As lowering the stress can be achieved by minimizing the thickness of the flexure, a drive stiffness constraint is used so that only flexures with the same drive stiffness are optimized. For this, the baseline flexure from Case 1 is used. This results, in the case of a critically loaded flexure, in a replacement flexure that can do the same job but with lower stresses, increasing the lifetime.

Firstly a baseline is set, for this case, the reaction force of the baseline flexure of Case 1 is used and a CT flexure is optimized for minimal stress. After this, the same optimization is done for a fully distributed VT flexure, a semi-lumped case with CT flexures and lastly a hybrid case that utilizes VT and incorporates a partially rigid midsection.

The optimized flexure properties can be seen in table 4 and the resultant thickness vs. stress plots can be seen in figure 8-11.

A clear improvement using VT flexures to minimize maximum stress can be observed. A decrease of

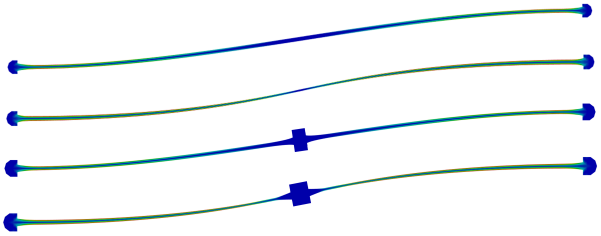

Figure 7. From top to bottom: Baseline, VT, Partially rigid CT, Partially rigid VT.

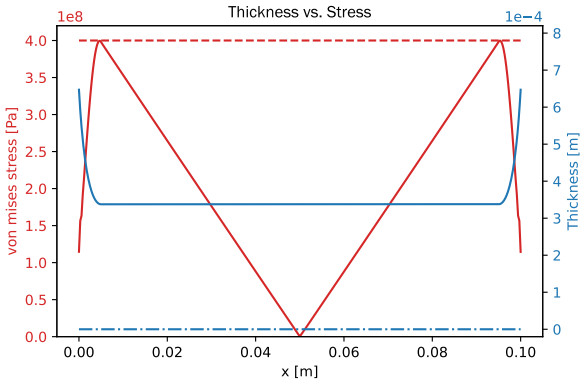

Figure 8. Half flexure thickness profile (blue) vs. stress (red) plot for the baseline flexure optimized for minimum stress.

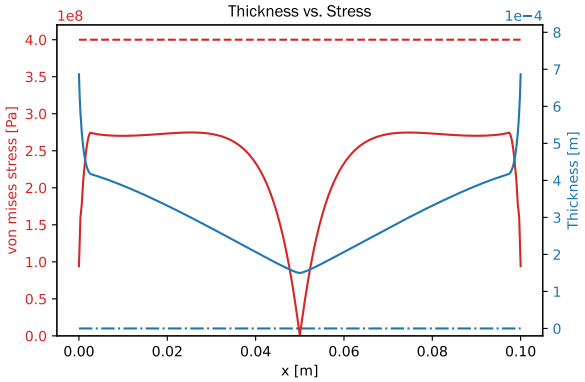

Figure 9. Half flexure thickness profile (blue) vs. stress (red) plot for a distributed VT flexure optimized for minimum stress.

31% was achieved for this case using the VT flexures. The flexure incorporating a rigid midsection has an effective length of 49 mm resulting in a near fully distributed flexure. From this, it can be concluded that when stress must be minimized it is most efficient to maximally use the whole length of the flexure.

5 Discussion

In Case 1, contrary to the partially rigid CT flexure, the length of the effective flexure is not minimized. The shape assumes roughly the same shape as the fully distributed VT flexure. This can have 2 possible

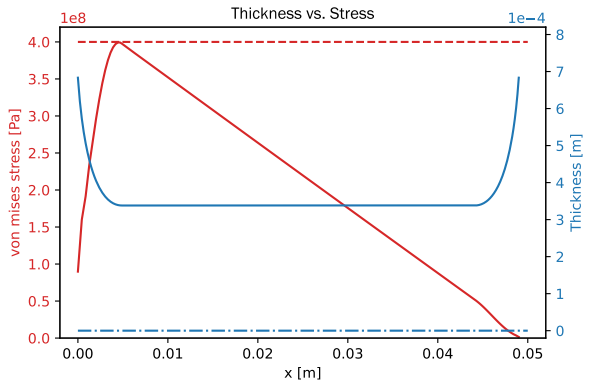

Figure 10. Half flexure thickness profile (blue) vs. stress (red) plot for a partially rigid CT flexure optimized for minimum stress. Only the left half of the flexure is plotted.

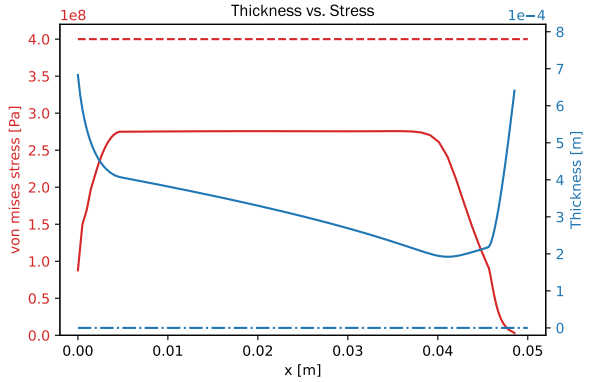

Figure 11. Half flexure thickness profile (blue) vs. stress (red) plot for a partially rigid VT flexure optimized for minimum stress. Only the left half of the flexure is plotted.

Table 4. Properties of the Baseline, Hybrid CT, Hybrid VT and distributed flexures optimized for lowest σ_{max} with the same drive stiffness. The improvement in stress minimization compared to the baseline is depicted in bold numbers.

		Baseline	**Distr. VT**	**Hybrid CT**	**Hybrid VT**
C_{x_0}	[N/m]	1.50E9	1.18E9	1.53E9	1.31E9
C_x	[N/m]	3.15E8	7.95E7	3.15E8	8.13E7
C_x/C_{x_0}	[-]	21%	7%	21%	6%
F_u	[N]	760.3	760.5	761.0	760.5
σ_{max}	[Pa]	4.00E8	2.75E8	4.00E8	2.76E8
Impr.	[-]	-	**31%**	**0%**	**31%**

reasons. The first one is that the flexure needs this less stiff (than the 10 mm beam) thicker section so that the C_{x0} is lower. As the objective is the ratio, the C_x could have less of an impact by this thinner midsection, thus resulting in a higher stiffness ratio. The second possibility is that the shape function as defined with the cubic Bezier curve cannot form the same "ideal" thickness variation in the region where the highest bending occurs. To see the influence on the ratio when constraining the maximum effective flexure length to 20 mm, the same optimization is run. The ratio drops quite significantly to 39%. Further analysis could be done with different shape functions to find out if this drop is due to the cubic Bezier not being able to generate the ideal thickness profile.

The optimization for the three cases is conducted using a fixed length flexure with a fixed minimum thickness, resulting in flexures with a comparable L/t ratio. To fully explore the potential impact of variable thickness (VT), the optimization should be performed for higher and lower L/t flexure ratios. Additionally, the length-to-displacement ratio L/u and its effect on the effectiveness of the method require further investigation. This study utilizes a ratio of 10, which represents a relatively long stroke. It is noteworthy that C_z is not taken into account in this research, which is also influenced by torsion around x.

In Case 1 and Case 2, the maximum C_x was influenced by, in the first case the C_{x_0} and in the second case the F_u. A case that is not explored but could prove beneficial is to maximize for C_x with only stress constraints. This would probably increase the drive stiffness, but could further show the potential to distribute material more effectively to increase stiffness. This is optimized for the partially rigid CT and VT flexures as the rigid midsection shows the highest potential in this research and in the literature as well. The maximum C_x achievable for a CT flexure is highly dependent on the minimum thickness, but with a minimum thickness set to 0.3 mm, a maximum C_x of 1.02×10^9 N m^{-1} and 1.05×10^9 N m^{-1} for a CT and a VT flexure, thus increasing the stiffness with 224% and 233%, but only differing 4.3% compared to each other.

6 Conclusion

This research introduces two new parametrizations and utilizes them to optimize the thickness profiles of leaf flexures. The study investigates three 2D cases, where the first two examine the improvement in support stiffness for same-stroke flexures. Case 1 looks at the increase in the support stiffness ratio. This is defined as the deflected support stiffness C_x divided by the undeflected support stiffness C_{x_0}. A higher stiffness ratio results in a flexure with a less severe support stiffness drop when deflected, allowing for larger ranges of motion with more predictable performance.

Case 2 introduces a constraint on the drive stiffness and maximizes the deflected support stiffness C_x, leading to an alternative flexure for an existing application where increased support stiffness is required. Case 3 assesses the potential to minimize the peak stress for a flexure with the same length and drive stiffness, providing an alternative with a higher range of motion or a higher safety factor on stress.

The results demonstrate that using the new parametrizations, both optimized variable thickness flexures outperform the baseline and partially rigid flexures utilizing constant thickness. In Case 1, the increase in stiffness ratio that could be achieved is 114% for distributed VT and partially rigid VT flexures. Here the trend of minimizing the length and thickness of the part of the flexure where most bending occurs clearly shows. Here utilizing a partially rigid midsection increases the stiffness ratio by 60% and using variable thickness, this increase in the ratio is doubled.

In Case 2, a significant increase in support stiffness can be achieved using a partially rigid VT flexure, with an increase of 125% compared to the baseline. Here again, the trend is to create a thicker midsection to distribute the bending further to the outer ends of the full flexure.

In Case 3, utilizing VT, a fully distributed flexure can achieve a decrease in maximum stress of 31%. The partially rigid flexure utilizes the full length and results in a near identical thickness profile resulting in the same maximum stress value.

The results suggest that VT flexures hold great promise for increasing support stiffness for same-stroke flexures and stress minimization for flexures with the same drive stiffness. The new parametrizations may offer a potential performance increase if maximum support stiffness is required for a mechanism where the driving force is constrained. Furthermore, VT flexures may increase the potential stroke or design safety factor of the flexure. Finally, compared to current CT flexure mechanisms, the increase in cost is minimal if the original manufacturing process is wire EDM.

References

[1] Hua Liu et al. "Design and modeling of a novel monolithic parallel XY stage with centimeters travel range". In: *Special Issue Article Advances in Mechanical Engineering* 9.11 (2017), p. 2017.

[2] Philipp Gräser et al. "High-precision and large-stroke XY micropositioning stage based on serially arranged compliant mechanisms with flexure hinges". In: *Precision Engineering* 72 (Nov. 2021), pp. 469–479.

[3] Lei-Jie Lai, Guo-Ying Gu, and Li-Min Zhu. "Design and control of a decoupled two degree of freedom translational parallel micropositioning stage". In: *Rev. Sci. Instrum* 83 (2012), p. 45105.

[4] C Werner, P C J N Rosielle, and M Steinbuch. "Design of a long stroke translation stage for AFM". In: *International Journal of Machine Tools and Manufacture* 50 (2009), pp. 183–190.

[5] Guangbo Hao and Jingjun Yu. "Design, modelling and analysis of a completely-decoupled XY compliant parallel manipulator". In: *Mechanism and Machine Theory* 102 (Aug. 2016), pp. 179–195.

[6] Guangbo Hao and Xianwen Kong. "A 3-DOF Translational Compliant Parallel Manipulator Based on Flexure Motion". In: (2012).

[7] Shorya Awtar and Alexander H Slocum. "Constraint-Based Design of Parallel Kinematic XY Flexure Mechanisms". In: (2007).

[8] Kee-Bong Choi and Doo-Hyeong Kim. "Monolithic parallel linear compliant mechanism for two axes ultraprecision linear motion". In: *Rev. Sci. Instrum* 77 (2006), p. 65106.

[9] Qingsong Xu. "New flexure parallel-kinematic micropositioning system with large workspace". In: *IEEE Transactions on Robotics* 28.2 (Apr. 2012), pp. 478–491.

[10] D. M. Brouwer, J. P. Meijaard, and J. B. Jonker. "Large deflection stiffness analysis of parallel prismatic leaf-spring flexures". In: *Precision Engineering* 37.3 (July 2013), pp. 505–521.

[11] Brian P Trease and Sridhar Kota. "Design of Large-Displacement Compliant Joints". In: (2005).

[12] Jan van Eijk. "ON THE DESIGN OF PLATE-SPRING MECHANISMS". PhD thesis. Delft: TU Delft, Apr. 1985.

[13] Girish Krishnan, Charles Kim, and Sridhar Kota. "A Metric to Evaluate and Synthesize Distributed Compliant Mechanisms". In: (2013).

[14] Saša Zelenika, Mircea Gh Munteanu, and Francesco De Bona. "Optimized flexural hinge shapes for microsystems and high-precision applications". In: *Mechanism and Machine Theory* 44.10 (Oct. 2009), pp. 1826–1839.

[15] Rongqi Wang, Xiaoqin Zhou, and Zhiwei Zhu. "Development of a novel sort of exponent-sine-shaped flexure hinges". In: *Review of Scientific Instruments* 84.9 (Sept. 2013).

[16] Qian Lu, Zhi Cui, and Xifu Chen. "Fuzzy multi-objective optimization for movement performance of deep-notch elliptical flexure hinges". In: *Rev. Sci. Instrum* 86 (2015), p. 65005.

[17] F. De Bona and M. Gh Munteanu. "Optimized flexural hinges for compliant micromechanisms". In: *Analog Integrated Circuits and Signal Processing* 44.2 (2005), pp. 163–174.

[18] Min Liu, Jinqing Zhan, and Xianmin Zhang. "Topology optimization of distributed flexure hinges with desired performance". In: *Engineering Optimization* 52.3 (Mar. 2020), pp. 405–425.

[19] Min Liu et al. "Topology optimization of flexure hinges with a prescribed compliance matrix based on the adaptive spring model and stress constraint". In: *Precision Engineering* 72 (Nov. 2021), pp. 397–408.

[20] Jon Freire Gómez, Julian D Booker, and Phil H Mellor. "2D shape optimization of leaf-type crossed flexure pivot springs for minimum stress". In: *Precision Engineering* 42 (2015), pp. 6–21.

[21] *PyMAPDL documentation 0.64.0 — PyMAPDL.*

[22] *PLANE183.* July 2017.

[23] *Surrogate Optimization Algorithm - MATLAB surrogateopt - MathWorks Benelux.*

[24] UDDEHOLMS AB. *UDDEHOLM STAVAX® ESR.* May 2013.

[25] Dan B. Marghitu, Cristian I. Diaconescu, and Bogdan O. Ciocirlan. "Mechanics of Materials". In: *Mechanical Engineer's Handbook* (2001), pp. 119–188.

A Appendix

A.1 Optimizing fit of cubic bezier curve to ideal thickness profile

To find out how good of an estimation a cubic bezier curve can make, a small optimization is run. Firstly we need to define the thickness profile for an ideal flexure using expression (2). The square root of x can be taken out of the full square root as the other part acts as a constant (see equation (A.2)).

$$t(x) = \sqrt{\frac{6Fx}{\sigma h}} = \sqrt{\frac{6F}{\sigma h}} \cdot \sqrt{x} \tag{A.1}$$

Filling in the constant using the data from the baseline of Case 3, we get:

$$t(x) = \sqrt{\frac{6F}{\sigma h}} \cdot \sqrt{x} = \sqrt{\frac{6 \cdot 761}{400e6 \cdot 1}} \cdot \sqrt{x} \tag{A.2}$$

The objective for the optimization is as follows with i the number of points on the curves that are compared:

$$Obj = \sum_{i=1}^{50} |t_{Bez}(i) - t_{Ideal}(i)| \tag{A.3}$$

For this optimization, the surrogateopt function in Matlab is used. More on this in chapter 3.7.

A.2 Variable thickness parametrization

In figure A.1 the parametrization of the distributed variable thickness flexure can be seen and in figure A.2 the parametrization of the variable thickness flexure using a partially rigid midsection.

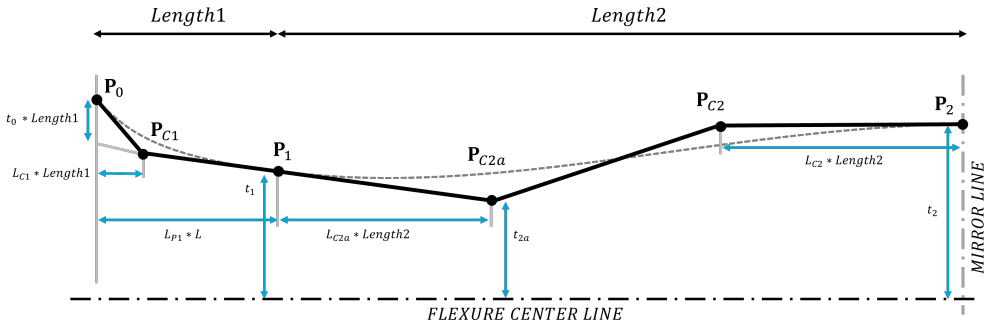

Figure A.1. Parametrization of VT flexure with 2 cubic bezier curves in the mid-section. See chapter 3.3 for more information.

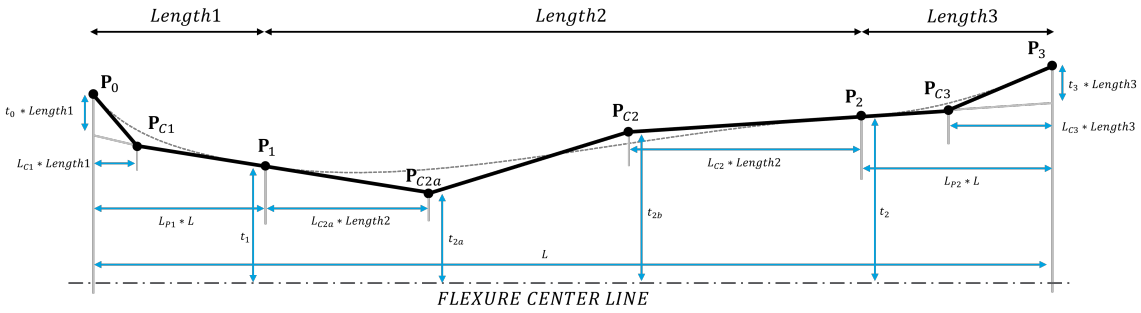

Figure A.2. Parametrization of VT flexure with 1 cubic bezier curves in the mid-section. This flexure is connected on the right using a rigid connection to a beam element connecting it to the output point at $x = 50$ mm. See chapter 3.3 for more information.

A.3 Optimized flexure parameter values

Table A.1. Optimized parameter values for the distributed reference flexure and distributed VT flexures.

Parameter	tmin	t0	LC1	t1	LP1	t2a	LC2a	LC2
lower bound	1.50E-04	0.05	0.20	0.000	0.05	1.50E-04	0.00	0.00
upper bound	1.00E-03	0.20	0.80	0.00	0.10	1.00E-03	1.00	1.00
Case 1 CT	3.3915E-04	7.6753E-02	0.20105627	3.3915E-04	0.0894223	3.3915E-04	0.3000000	0.3000000
VT	5.1878E-04	5.0174E-02	0.20000000	1.5000E-04	0.0604445	1.5000E-04	0.3243199	1.0000000
Case 2 CT	3.3915E-04	7.6753E-02	0.20105627	3.3915E-04	0.0894223	3.3915E-04	0.3000000	0.3000000
VT	7.6505E-04	1.0716E-01	0.20040123	3.4873E-04	0.0562451	1.5347E-04	0.7964520	0.8681653
Case 3 CT	3.3915E-04	7.6753E-02	0.20105627	3.3915E-04	0.0894223	3.3915E-04	0.3000000	0.3000000
VT	1.5000E-04	9.3656E-02	0.20710083	4.1656E-04	0.0555561	3.5648E-04	0.3594766	0.0671309

Table A.2. Optimized parameter values for the partially rigid CT and VT flexures.

Parameter	L	t_min	t_0	lc_1	t_1	l_1	t_2a	t_2b	lc_2a	lc_2	lc_3	l_3	t_3
lower bound	0.02	1.50E-04	0.05	0.20	1.50E-04	0.05	1.50E-04	1.50E-04	0.00	0.00	0.20	0.050	0.05
upper bound	0.049	1.00E-03	0.20	0.80	1.00E-03	0.10	1.00E-03	1.00E-03	1.00	1.00	0.80	0.10	0.20
Case 1 CT	0.01000000	1.5000E-04	0.17540401	0.69410189	1.5000E-04	0.10000000	1.5000E-04	1.5000E-04	0.30000000	0.30000000	0.69410189	0.10000000	0.17540401
VT	0.04900000	5.4947E-04	0.05960586	0.20000000	1.5000E-04	0.05061984	1.5000E-04	4.6196E-04	0.36043464	1.00000000	0.68741205	0.06578192	0.14969349
Case 2 CT	0.04745816	3.3848E-04	0.07301738	0.20417657	3.3848E-04	0.10000000	3.3848E-04	3.3848E-04	0.30000000	0.30000000	0.20417657	0.10000000	0.07301738
VT	0.02311528	3.0214E-04	0.07036656	0.51071497	3.7909E-04	0.05618080	3.4488E-04	3.0238E-04	0.01000000	0.55180223	0.45286761	0.05108695	0.19155989
Case 3 CT	0.04900000	3.3893E-04	0.07212523	0.20000000	3.3893E-04	0.10000000	3.3893E-04	3.3893E-04	0.30000000	0.30000000	0.20000000	0.10000000	0.07212523
VT	0.04852019	2.1735E-04	0.05270512	0.20637164	4.0652E-04	0.09948035	2.1891E-04	1.5000E-04	0.99853928	0.22191529	0.68229902	0.06073126	0.13623059

4

Paper II: Optimization of variable thickness, initially curved flexure mechanisms for increased support stiffness and increased range of motion

As is concluded in paper I, variable thickness with the same stroke and the same maximum stress can significantly improve the support stiffness. When optimizing for minimal stress, variable thickness again has an advantage.

In this paper, mechanisms using variable thickness flexures with initial curvature will be compared to mechanisms with constant thickness flexures with curvature to see again if the support stiffness can be increased, or the stroke of a mechanism can be maximized by having lower stress for the same stroke.

Highlights

Optimization of variable thickness, initially curved flexure mechanisms for increased support stiffness and increased range of motion

F.W.F. Colin

- A new design strategy adding variable thickness to optimizing initially curved flexure mechanisms is presented.
- A near-constant support stiffness mechanism with a range of motion of $\pm$ 10 mm, maximum parasitic translation of 10 µm and a stiffness ratio, C_y/C_x, of 248. Adding variable thickness increases this by 103%.
- A linear guiding mechanism with a parasitic motion of 0.2 µm and 100 µrad and a stiffness ratio of 729. Adding variable thickness increases this ratio by 84% and increases the mean support stiffness by 26%.
- A linear guiding mechanism with a parasitic translation of 10 µm, a minimum stiffness ratio of 100 and a stroke of 27.65 mm using constant thickness initially curved flexures. When variable thickness is added this range of motion increases to 30.60 mm.

Optimization of variable thickness, initially curved flexure mechanisms for increased support stiffness and increased range of motion

F.W.F. Colin [1]

[1] *Department of Precision and Microsystems Engineering, Faculty of 3mE, Delft University of Technology, Delft, the Netherlands*

ARTICLE INFO

Keywords:
Parasitic motion
Range of motion
Compliant mechanism
Stiffness ratio
Support stiffness
Constant support stiffness

Abstract

Flexure mechanisms have gained popularity as a viable alternative to conventional mechanical systems due to their high precision, lack of friction and lubrication-free operation. However, the limited range of motion caused by stress peaks, the significant reduction in support stiffness when deflected and undesired parasitic motions are three primary concerns in the application of flexure mechanisms. This paper presents a novel optimization method for designing mechanisms with good parasitic properties and increased support stiffness and range of motion using initially curved variable thickness flexures. To show the potential of this method, 3 cases were introduced. These cases are first optimized with constant thickness flexures and subsequently, variable thickness is added to further increase the support stiffness in cases 1 and 2 and to increase the stroke in case 3. The first case resulted in a mechanism with a near-constant support stiffness over the whole stroke. The change in support stiffness is constrained to 0.1% with parasitic motion below 10 µm and 2 mrad. Introducing variable thickness increases the support stiffness by 103% without compromising other properties. Case 2 optimized a minimum parasitic motion mechanism for maximum support stiffness, resulting in a mechanism with parasitic motion below 0.2 µm and 100 µrad. Using variable thickness flexures the support stiffness can be increased by 25.9%. In the last case, the maximum stroke is maximized with constrained parasitic behavior. This resulted in a mechanism with a stroke of 27.65 mm for constant thickness flexures and 30.60 mm for variable thickness flexures.

1 Introduction

Compliant mechanisms become more and more important in precision mechanisms in the fields of, for example, micro-manufacturing, optical fiber alignment, biological engineering and scanning probe microscopy [1]. High-precision motion stages in the field of lithography have an increasing need for larger ranges of motion and given the lack of friction, lack of lubrication needs and nearly flawless repeatability, compliant mechanisms are the ideal fit [1–3].

A commonly used mechanism is the parallel leaf spring flexure. Parallel flexure mechanisms have an approximate straight line motion for small displacements. These mechanisms are used for example in the use of precision coordinate measurement machines [4], Hao and Yu used this mechanism for a compliant xy manipulator [5], Hao and Kong used this in the design for a self-adaptive compliant parallel gripper for high-precision manipulation [6]. When stacked and mirrored, a double parallel leaf spring flexure is achieved that is used in many applications as the parasitic motion of the intermediate body cancels that of the output body. These double parallel leaf spring flexures are used in a variety of applications like precision xy stages [3, 6–13].

These mechanisms allow for translations with high repeatability, however, the range of motion is constrained by the material characteristics, particularly the maximum permitted stress concentrations [1–3]. Besides the stress concentrations, the drop in support stiffness (C_y as seen in figure 1) when deflected limits the precision that can be obtained [14, 15].

One way to improve flexure performance is by using variable thickness (VT) flexures. A benefit of thickness-varying flexures is their ability to deform less under axial load [16, 17]. This is advantageous in applications where a high support stiffness is necessary. Furthermore, Wu et al. showed that with the tuning of the parameters of thickness-varying flexures, a big influence on compliance and stiffness ratios could be achieved [18]. Krishnan et al. showed that besides increasing the support stiffness, VT flexures can travel a longer distance and handle larger input forces than a beam of the same stiffness but a uniform cross-section [19]. Tschiersky et al. showed that an increase in energy density of 277% was achiev-

able using variable thickness initially curved flexures towards the design of an assistive elbow orthosis [20].

A relatively new method for designing leaf flexure mechanisms is to use the advantages of initially curved flexures. The advantages these initially curved flexures pose are a relatively large range of motion and a relatively small strain range [21–25]. Another benefit could be using the geometric non-linearities these flexures exhibit for large deflections to our advantage. In the field of parasitic motion minimization, these non-linearities can be used to compensate the parasitic motions about 3.4 times better than the Roberts mechanism. It is also shown in a different case study that a much more constant stiffness along the full displacement can be achieved in all directions [26].

A drawback these initially curved flexures exhibit is that they perform poorly under compressive forces [27]. This however can be compensated for. By using a set of curved leaf flexures, the drop of stiffness in the stiff directions can be compensated as one of the 2 leaf flexures will straighten when deflected resulting in a stiffer geometry in deflected configuration [26, 28–31].

All these papers look at different properties and none seem to look at the ability of the method of initial curvature and variable thickness to generate straight line mechanisms with near-constant support stiffness, small parasitic errors, increased support stiffness, or an increased range of motion. The previous work of Meinders et al. [26] shows promising results using initially curved flexures to generate straight line mechanisms so this method will be used as a starting point to explore different design goals. As variable thickness flexures show great promise in terms of increasing support stiffness or minimizing stress, an addition to this method of optimizing initially curved flexure mechanisms will be made to combine the best of both worlds.

This research aims to see the potential of optimizing initially curved flexure mechanisms towards the design of a constant support stiffness, a minimal parasitic motion and a maximum stroke linear guiding mechanism and explore if we can improve the performance in support stiffness or range of motion even further by combining initially curved and variable thickness flexures.

The structure of this paper is as follows. First, the method and case studies are introduced. Afterwards, the results of these case studies are presented. Then, the experimental results of one of the cases are presented followed by a discussion and a conclusion.

2 Method and Case Studies

In this section, the method will be introduced and described in detail. The case studies will be introduced and lastly, the constraint and objective functions are presented.

2.1 Definitions

In figure 1 the global definitions can be seen. Besides the global coordinates, parasitic motion δy and parasitic rotation $ParRotation$ or δrot are visualised as well.

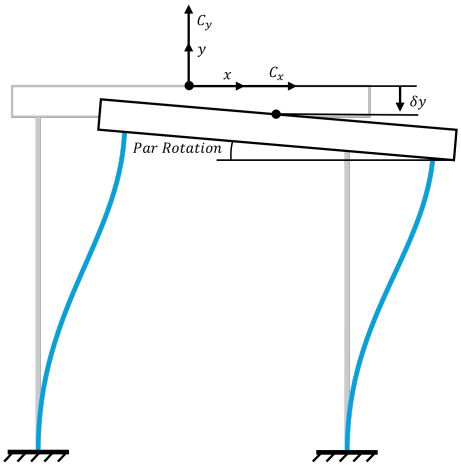

Figure 1. x and y-axis definition, z-axis is out of plane and points towards you.

2.2 Scope and Assumptions

In this research we only look at 2D extruded mechanisms, with the support stiffness defined as the stiffness in y-direction, see figure 1. Some assumptions are made in the design of the mechanisms. These are as follows:

(1) The effects of gravity are negligible
(2) In-plane geometries are used, these are extruded to form 3D geometries
(3) Material is uniform
(4) The material is free from internal stresses
(5) No other loads are applied to the mechanism
(6) Beams connecting flexures are considered rigid

2.3 Modelling initial curvature

To parameterize the initial curvature of the middle line of the flexures (as can be seen as the dotted line in figure 3), quadratic Bezier curves are used. These Bezier curves are useful as they offer smooth continuous curvature with only 3 control points. The x and y coordinates for points along the curve are defined by 3 control points, $\mathbf{P}_0$, $\mathbf{P}_1$ and $\mathbf{P}_2$ and a value t from 0 to 1 as follows.

$$\mathbf{B}(t) = (1-t)^2\mathbf{P}_0 + 2t(1-t)\mathbf{P}_1 + t^2\mathbf{P}_2 \qquad (1)$$

Using n equally spaced t values to generate points on the curve does not lead to same-length beam elements. Elements closer to tight curvature are shorter than straighter sections. This is not a problem for constant thickness flexures, but to be able to have a consistent parametrization for variable thickness flexures for all curvatures, these elements need to be of equal length as the individual elements have a characteristic thickness. To mitigate this problem, the actual distances are compared to their t value when n equally spaced t values are used. The resultant t to length values are interpolated to define the t values where the length of the elements are equal. With these new t values the points are again generated and these correspond to near-equal-length elements.

The parameterization of the Bezier curves is done by 2 control points, $\mathbf{P}_0$ and $\mathbf{P}_2$, on the ends of the curve that are defined by an x and y value. The middle control point, $\mathbf{P}_1$, is a result of a fraction of the length between $\mathbf{P}_0$ and $\mathbf{P}_2$ called l and a perpendicular distance from this point, defined as $b \cdot L$ with L the distance between $\mathbf{P}_0$ and $\mathbf{P}_2$, see figure 2. With this parametrization, each flexure has 6 control points to define the shape of the mid-line and either 1 or 4 control points to define the thickness profile for a constant thickness and variable thickness flexure respectively. This results in a total of 28 parameters to define the CT flexure mechanism and 40 parameters for a VT flexure mechanism.

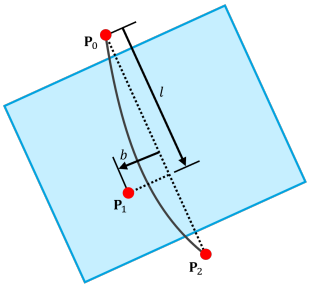

Figure 2. Bezier curve parametrization using control point $\mathbf{P}_0$, $\mathbf{P}_1$ and $\mathbf{P}_2$. In blue, the constraint space for $\mathbf{P}_1$.

2.4 Variable thickness flexures

To parameterize the variable thickness, a modified Akima piecewise cubic Hermite interpolation is used [32]. This interpolation is done in n equally spaced points that correspond to the thickness values of the beam elements. The spline is interpolated between 3 control points. The first, $\mathbf{t}_0$, at the base of the flexure. The second point, $\mathbf{t}_1$, is placed somewhere between 0.1 and 0.9 times l (this parameter is called l_{min}) on the length of the flexure. And lastly, $\mathbf{t}_2$ is placed at the end of the flexure. See figure 3 for the parametrization.

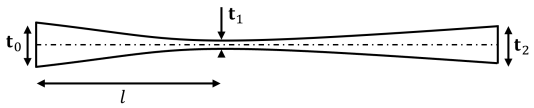

Figure 3. Parametrization of the control thicknesses interpolated by Akima piecewise cubic Hermite interpolation.

2.5 Topology

The input topology uses 2 flexures fixed on one side and connected to an intermediate body on the other side, from this intermediate body 2 flexures are connected to the output body. This topology is chosen so that the algorithm, in theory, can make something resembling a double parallelogram and a Roberts mechanism, see figure 4. Besides this, it was shown in the work of Meinders [33], it has the potential for a variety of mechanisms with good parasitic properties. It might be very interesting to look at more configurations, however, this induces overconstraints.

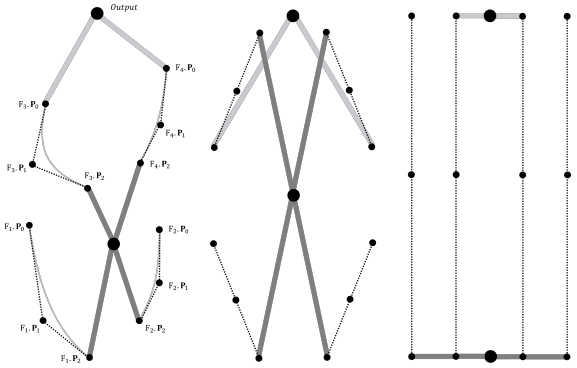

Figure 4. left: Control points for the four initially curved flexures with on the top the output node. center: Roberts mechanism and on the right: the double parallelogram.

The mechanism is horizontally mirrored to form the full mechanism. This removes the rotational degree of freedom resulting in a 1-degree-of-freedom mechanism.

2.6 Software

To carry out the numerical analysis, *SPACAR* [34] is used. This is a flexible multibody software package that uses planar nonlinear beam elements to model the mechanism. These nonlinear beam elements have a constant cross-sectional area and are straight in their undeformed state.

2.7 Discretization

To model the initial curvature of the flexure, quadratic Bezier curves are used as described in section 2.3. As the beam elements used by *SPACAR* are straight, the flexure needs to be discretized by multiple beam segments. The thickness is also discretized by means of the constant thickness beam elements each with its unique thickness defined by the modified Akima piecewise cubic Hermite interpolation as described in section 2.4.

2.8 Optimization Algorithm

Matlab's surrogateopt algorithm is used [35]. This algorithm is suitable for computationally expensive objective functions as it uses the surrogate model to approximate the response of the system by interpolating a radial basis function between random sampling points. After a set amount of random sampling points between the bounds, the algorithm switches to the second phase. In phase 2 the algorithm searches for a minimum by sampling thousands of points on the surrogate model and the best point is then evaluated and the objective value is used to update the surrogate model. This step continues until a minimum is found. When this minimum is found, the algorithm switches back to phase 1 and constructs a new surrogate.

2.9 Case studies introduction

To see the ability of this new method to generate better performing mechanisms, 3 test cases were used to find 3 mechanisms that look at one of the 3 important limiting factors for compliant mechanisms. The first one is the significant drop in support stiffness when deflected. The second case looks for a new geometry that has a minimal parasitic motion while maintaining a support-to-drive stiffness ratio(R_C) of at least 100 and the last case aims to find a geometry that has a maximum range of motion.

After these novel new mechanisms are found, the first 2 case studies are conducted for CT and VT flexures to see the influence that variable thickness has on the performance in support stiffness. The last case study looks at the increase in range of motion variable thickness flexures can offer.

(1) Maximizing stiffness ratio for a near-constant support stiffness mechanism
(2) Maximizing stiffness ratio for a minimum parasitic motion mechanism
(3) Maximizing stroke with constrained parasitic behavior

2.10 Constraints

For the different test cases, different constraints were applied. These fall under geometry constraints and output constraints. In this section, the different constraints are explained.

2.10.1 Geometry constraints

Minimum flexure clearance constraint: To be able to generate monolithic designs, it is necessary not to have flexure intersections and allow for space between flexures to allow solid structure elements to connect all the flexures. The minimum distance and, if applicable, intersection (utilizing part of the code from Schwarz [36]) is defined for every flexure combination at all load steps. If the flexures intersect at any point in the stroke the distance is 0, otherwise, the distance is the minimum distance.

$$\frac{distance_{max} - min(\boldsymbol{distance})}{distance_{max}} \leq 0 \tag{2}$$

Self intersection constraint: Self-intersection can be avoided by using the constraint proposed by Zhou and Ting [24].

$$max(0.5w - \rho(t)) < 0 \tag{3}$$

$$\rho(t) = \frac{(\dot{x}^2(t) + \dot{y}^2(t))^{2/3}}{|\dot{x}(t)\ddot{y}(t) - \ddot{x}(t)\dot{y}(t)|} \tag{4}$$

The extreme case would be maximum thickness, maximum or minimum l and maximum or minimum b, see figure 2. The maximum thickness of a flexure is set at 2mm. In this case, the length between $\mathbf{P}_0$ and $\mathbf{P}_2$ must be at least 4mm not to have a self-intersection. As this results in a lumped flexure hinge, this will not happen in any of the cases and therefore is neglected in the optimization.

2.10.2 Output constraints

Parasitic translation constraint: The maximum deviation in y-direction should not exceed δy_{max}, resulting in the following constraint.

$$\frac{max(\boldsymbol{\delta y}) - \delta y_{max}}{\delta y_{max}} \leq 0 \tag{5}$$

Parasitic rotation constraint: The maximum parasitic rotation around the z-axis should not exceed δrot_{max}, resulting in the following constraint.

$$\frac{max(\boldsymbol{\delta rot}) - \delta rot_{max}}{\delta rot_{max}} \leq 0 \tag{6}$$

Stress constraint: The maximum stress occurring somewhere in the system at any point in the displace-

ment must not exceed σ_{max}.

$$\frac{max(\boldsymbol{\sigma}) - \sigma_{max}}{\sigma_{max}} \leq 0 \tag{7}$$

Support stiffness deviation constraint: The maximum difference in support stiffness is constrained to be below $\delta C_{y,max}$.

$$\delta C_y = \frac{max(\boldsymbol{C}_y) - min(\boldsymbol{C}_y)}{min(\boldsymbol{C}_y)} \tag{8}$$

$$\frac{\delta C_y - \delta C_{y,max}}{\delta C_{y,max}} < 0 \tag{9}$$

Drive stiffness constraint: To see the possible increase in support stiffness for a mechanism with the same or increased drive stiffness, a constraint is set on the minimum $\overline{C}_x$.

$$\frac{\overline{C}_{x,CT} - \overline{C}_x}{\overline{C}_{x,CT}} \leq 0 \tag{10}$$

2.11 Objective

For the 3 case studies, different objectives are used and these are introduced in the following subsections.

2.11.1 Case 1: Increase stiffness ratio for a near-constant support stiffness mechanism

This case aims to look at the capability of the initially curved flexure mechanisms to improve the support stiffness for a mechanism designed to have a near-constant support stiffness. Decreasing the support stiffness difference results in mechanisms having less parasitic motion deviation due to an external load and a more constant parasitic motion shift, still resulting in good straight line motion. Increasing the support stiffness makes the mechanism less influenced by external loads as the induced parasitic motion will be lower.

This optimization is done sequentially. In the first step the objective is to minimize the support stiffness difference, while in the second step, the objective is to maximize the stiffness ratio with the parasitic motion as a constraint. The parasitic motion is relaxed a bit and the bounds on the control point positions are set to ±5% of the optimized design from step 1. The stiffness ratio is used as this is a normalized metric independent of material choice and size.

As the stiffness ratio is determined by the C_x as well as the C_y, Case 1 looks at the increase in stiffness ratio and Case 1.1 looks at the increase of the stiffness ratio with a constrained $\overline{C}_x$ to be at least as high as the $\overline{C}_x$ for the optimized CT design.

Step 1:

$$min. \quad Obj = \delta C_y \tag{11}$$

Step 2:

$$min. \quad Obj = -R_C \tag{12}$$

2.11.2 Case 2: Increase stiffness ratio with minimal parasitic error

This case looks at the ability to increase the stiffness ratio while having a very small parasitic error. A minimal parasitic error is desired in multiple fields from atomic microscopes to wafer scanning stages.

This optimization is done sequentially. In the first step the objective is to minimize the parasitic error, while in the second step, the objective is to maximize the stiffness ratio with the parasitic motion as a constraint. The parasitic motion is relaxed a bit and the bounds of the control point positions are set to ±5% of the optimized design from step 1.

As the stiffness ratio is determined by the C_x as well as the C_y, Case 2 looks at the increase in stiffness ratio and Case 2.1 looks at the increase of the stiffness ratio with a constrained $\overline{C}_x$ to be at least as high or higher than the $\overline{C}_x$ of the optimized CT design.

Step 1:

$$min. \quad Obj = \delta y \tag{13}$$

Step 2:

$$min. \quad Obj = -R_C \tag{14}$$

2.11.3 Case 3: Maximizing stroke with constrained parasitic behavior

As one common limitation of compliant mechanisms is their limited range of motion, this case aims to maximize this with constrained parasitic motion, a minimum stiffness ratio R_C of 100, subject to stress constraints.

To define the maximum stroke, the input displacement was set to 35 mm (assumed unachievable within the bounds) and the maximum displacement is interpolated between the load step that is below and over the stress limit. The parasitic motion as well as the stiffness ratio are defined within this maximum stroke.

This makes the response increasingly non-linear as the parasitic and stiffness response is only taken when the stress is below 20 MPa. For this reason, only 4 elements per flexure are used and only half of the mechanism is modeled in step 1. Using the parasitic behavior when deflected in positive and negative directions, the parasitic motion, parasitic rotation and C_y are defined for the full mechanism. In step 2 the lower and upper bounds on the control

point positions are set ±10% of this geometry and the optimization is done for the constant thickness and variable thickness flexures using 6 elements per flexure and the full mirrored mechanism is used.

Step 1:

$$min. \quad Obj = -\delta x \tag{15}$$

Step 2:

$$min. \quad Obj = -\delta x \tag{16}$$

2.12 Material properties

The material used in the optimization is Tough 1500 from Formlabs [37]. This material is used as it is printable on the Formlabs 3 SLS 3D printer. This printer has an xy accuracy of 25 µm [38] making it ideal for printing variable thickness flexures. The minimal support stiffness deviation mechanism is optimized for this material, as well as with aluminium 7075-T6. The 7075-T6 mechanism is produced with wire EDM and is used for testing to validate the simulation. This experiment is explained in section 3.4. Material properties used for these 2 materials can be seen in table 1.

Table 1. Material properties of Formlabs Tough 1500 [37] & Aluminium 7075-T6.

		Tough 1500	7075-T6
Young's modulus	[GPa]	1.5	71.7
yield strength	[MPa]	33	460
shear modulus	[GPa]	0.4	26.9
density	[kg/m^3]	1070	2800

3 Results

In this section, the results of the 3 case studies are presented. First, 3 novel mechanisms are designed by optimizing for support stiffness deviation, parasitic motion and maximum stroke for the 3 cases respectively. Afterwards, each of these mechanisms is further optimized using constant thickness and variable thickness flexures and the 2 are compared to each other.

3.1 Maximizing stiffness ratio for a near constant support stiffness mechanism

Step one minimizes support stiffness deviation subject to the constraints as stated in table 2. Optimizing for C_y deviation results in a novel mechanism with a support stiffness deviation of only 0.0026% with a parasitic translation of 7.99 µm, a parasitic rotation of 6.98×10^{-4} rad and a stiffness ratio of 122.7. In step 2 the maximum support stiffness deviation is constrained to a maximum of 0.1%. As this is an extremely nonlinear optimization problem with a large set of parameters, the lower and upper bounds for the control point positions are taken ±5% of the initially found mechanism from step 1. This reduces the design space by a factor of 10^{24} as we have 28 parameters minus 4 parameters for the thickness of each flexure.

Table 2. Constraint values for the near constant support stiffness mechanism. The maximum $\overline{C}_x$ difference ct. CT constraint is not active for Case 1 but is activated for Case 1.1.

Constraint		step 1	step 2
Maximum parasitic motion	[µm]	10	10
Maximum parasitic rotation	[µrad]	2000	2000
Maximum stress	[MPa]	20	20
Maximum C_y deviation	[%]	*Obj*	0.1
Maximum $\overline{C}_x$ difference ct. CT	[%]	-/5	-/5
Minimum C_y/C_x ratio	[-]	100	*Obj*

In step 2 the constant thickness mechanism is optimized for the highest stiffness ratio (C_y/C_x). This was also done for the variable thickness mechanism and a second optimization is done for a variable thickness mechanism but with a $\overline{C}_x$ constraint to be greater or equal to $\overline{C}_x$ of the CT mechanism.

The mechanism properties can be seen in table 3. Optimizing for R_C results in an increase of 89.3%. This is mainly because the C_x drops 68%. The C_y drops as well, thus resulting in a decreased support stiffness performance.

The optimized design that constrains $\overline{C}_x$ has an increase in R_C of 103.2% and an increase in C_y of 103%. This design can be seen in figure 5. Case 1 did not result in the same optimal point while there is no bound on the $\overline{C}_x$ in this case. This is due to limited computation time per case and here resulted in a local minimum.

Table 3. Properties of CT and VT mechanisms for maximum R_C with near constant support stiffness.

			Case 1		**Case 1.1**	
		CT	VT	Δ	VT	Δ
δy	[m]	4.36	9.56	-119%	9.42	-116%
δrot	[rad]	1.70×10^{-3}	1.50×10^{-3}	12%	2.67×10^{-4}	84%
$\delta x\pm$	[mm]	10	10	0%	10	0%
σ_{max}	[MPa]	14.67	11.44	28%	16.2	-9%
δC_y	[-]	0.086%	0.099%	-15%	0.096%	-11%
$\overline{C}_x$	[N m^{-1}]	677.81	215.42	-68%	676.4	0%
$\overline{C}_y$	[N m^{-1}]	1.74E+05	1.05E+05	-40%	3.54E+05	103%
R_C	[-]	247.7	469.0	**89.3%**	503.4	**103.2%**

To see the effectiveness in minimizing the induced parasitic motion due to external loads, an external load in negative y direction of 1 N is applied and the parasitic motion difference is plotted in figure 6. The increase in support stiffness has indeed resulted in a lower induced error and besides that for both

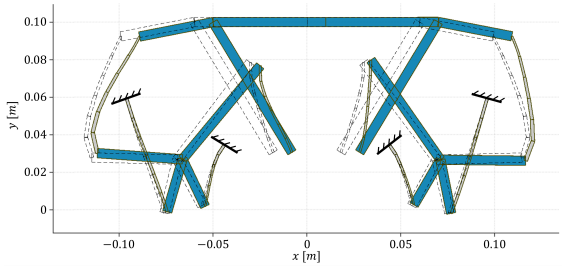

Figure 5. Mechanism optimized for stiffness ratio with same C_x as CT mechanism using variable thickness flexures for minimal C_y deviation.

the CT and VT mechanism, the change in straight line error is 3.3 nm and 1.5 nm for the CT and VT mechanism respectively, thus resulting in straight line motion(max 10 µm) for arbitrary external loads.

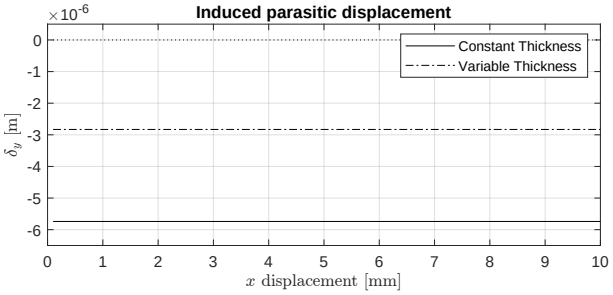

Figure 6. Induced parasitic motion with an applied load of 1 N in negative y direction for the CT and VT optimized designs with near constant C_y over the whole stroke.

3.2 Maximizing stiffness ratio for a minimum parasitic motion mechanism

Step 1 minimizes the parasitic motion, with active constraints as defined in table 4. This results in a mechanism with a parasitic translation of 13.6 nm and a parasitic rotation of 35.2 µrad. In comparrison, when optimizing the Roberts mechanism in *SPACAR* with the same constraints, a parasitic translation of 327 nm can be achieved, being 9.3 times higher.

Table 4. Constraint values for a minimal parasitic motion mechanism. The maximum $\overline{C}_x$ difference ct. CT constraint is not active for Case 2 but is activated for Case 2.1.

Constraint		step 1	step 2
Maximum parasitic motion	[µm]	*Obj*	0.2
Maximum parasitic rotation	[µrad]	100	100
Maximum stress	[MPa]	20	20
Maximum C_y deviation	[%]	-	-
Maximum $\overline{C}_x$ difference ct. CT	[%]	-/5	-/5
Minimum C_y/C_x ratio	[-]	100	*Obj*

Step 2 optimizes the stiffness ratio R_C with the parasitic motion constrained to 0.2 µm and the lower and upper bounds of the control points are taken ±5% of the optimized design from step 1. Just as in Case 1, the lower and upper bounds of the thickness of the flexures is not altered. The optimized mechanisms properties can be seen in table 5.

Table 5. Properties of CT and VT mechanisms for maximum R_C with minimal parasitic motion.

			Case 2		**Case 2.1**	
		CT	VT	Δ	VT	Δ
δy	[m]	1.72E-07	1.94E-07	-13%	1.97E-07	-15%
δrot	[rad]	3.22E-05	8.79E-05	-173%	9.67E-05	-200%
$\delta x\pm$	[mm]	10	10		10	
σ_{max}	[MPa]	10.04	8.94	12%	10.01	0%
δC_y	[-]	11.1%	16.0%	-45%	13.2%	-19%
$\overline{C}_x$	[N m^{-1}]	614.20	407.95	-34%	613.51	0%
$\overline{C}_y$	[N m^{-1}]	4.82E+05	6.07E+05	25.9%	5.66E+05	17.3%
R_C	[-]	729.1	1339.9	**83.8%**	848.7	**16.4%**

For constant thickness leaf flexures, a maximum R_C of 729.1 is achieved with $\overline{C}_y = 4.82 \times 10^5$ N m^{-1}. The same optimization is done for VT flexures using the same design space for the control points. Maximizing the R_C results in an increase of 83.8% to 1339.9 and an increase in $\overline{C}_y$ of 25.9% to 6.07×10^5.

Applying a lower bound on the $\overline{C}_x$ to be at least $\overline{C}_x$ of the CT flexure mechanism results in an increase of R_C of 16.4% with an increase in $\overline{C}_y$ of 17.3% to 5.66×10^5. In this case, the $\overline{C}_y$ is lower than in Case 2, suggesting that if an increase in support stiffness is desired

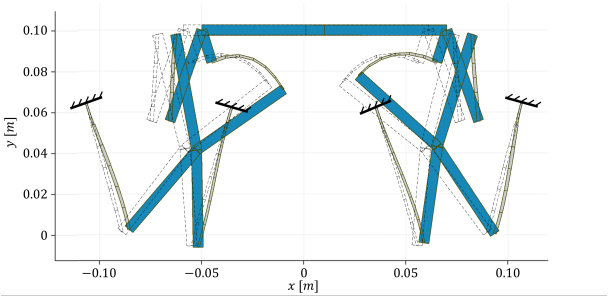

Figure 7. VT flexure mechanism optimized for maximum R_C with constrained parasitic motion.

3.3 Maximizing stroke with constrained parasitic behavior

Table 6. Constraint values for a maximum stroke mechanism with constrained parasitic behavior

Constraint		Value
Maximum parasitic motion	[µm]	10
Maximum parasitic rotation	[µrad]	2000
Maximum stress	[MPa]	20
Minimum C_y/C_x ratio	[-]	100

With limited elements per flexure (4 elements) and a maximum parasitic motion constraint of 15 µm, a good initial guess can be found. For step 2, the mechanism is optimized further for CT and VT with the new control point bounds ±10% of the initial optimized design from step 1.

Using CT flexures, a mechanism with a maximum stroke of 27.6 mm can be achieved. All the properties can be found in table 7. When optimizing for maximum stroke with VT flexures, the stroke can be extended to 30.6 mm, a 10.7% increase. The VT mechanism can be seen in figure 8.

Table 7. Properties of CT and VT mechanisms for maximum stroke with constrained parasitic behavior

		CT	VT	Δ
δy	[µm]	9.30	9.90	-6%
δrot	[rad]	0.002	0.002	0%
$\delta x\pm$	[mm]	27.65	30.60	**10.7%**
σ_{max}	[MPa]	20.0	20.0	0%
δC_y	[-]	93.9%	121%	-28%
$\overline{C}_x$	[N m^{-1}]	257.42	207.33	-19%
$\overline{C}_y$	[N m^{-1}]	4.41×10^4	3.80×10^4	-14%
R_C	[-]	105.8	100.0	-5%

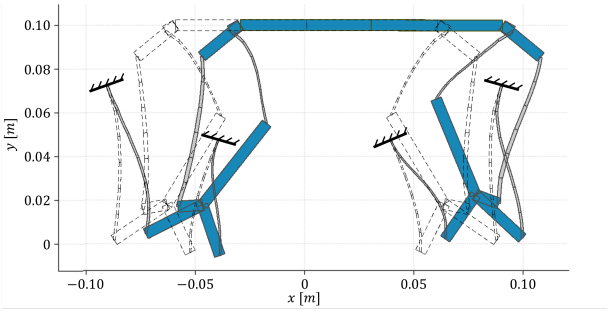

Figure 8. Mechanism with VT flexures optimized for a maximum stroke with parasitic motion and minimum stiffness ratio constraints. Maximum stroke is 30.6 mm

3.4 FEA validation and Test measurements

To validate and test the *SPACAR* simulation, the mechanism from case 1 is optimized for aluminium 7075-T6. This mechanism is then produced using wire EDM for a physical test. The minimum flexure thickness is set to 0.4 mm and a maximum reaction force of 40 N is implemented. This is firstly optimized for CT flexures and secondly, a VT flexure mechanism with a constrained $\overline{C}_x$ is optimized for a maximum stiffness ratio. The resultant properties can be seen in table 8. To have a more accurate approximation of the real mechanism, 10 beam elements per flexure are used.

The optimized design is converted to a 3d model which is used to construct an aluminium version for the experiment and the model is also used in Ansys to validate the model using solid elements.

Table 8. Properties of CT and VT mechanisms for maximum R_C with near constant support stiffness optimized with 10 beam elements per flexure in aluminium 7075-T6

		Case 1.1		
		CT	VT	Δ
δy	[µm]	6.64	10.0	-51%
δrot	[rad]	2.00×10^{-3}	1.90×10^{-3}	5%
$\delta x\pm$	[mm]	10	10	0%
σ_{max}	[MPa]	282.6	338.2	-16%
δC_y	[-]	0.100%	0.110%	-10%
$\overline{C}_x$	[N m^{-1}]	2.53×10^3	2.47×10^3	-2%
$\overline{C}_y$	[N m^{-1}]	7.30×10^5	1.46×10^6	100%
R_C	[-]	278.6	568.3	**104%**

As the accuracy of the *SPACAR* result may be subject to the limited amount of beam elements, a FEM simulation in Ansys is done. The flexures are modeled with 2 quadratic hex elements in thickness. To minimize elements, the solid bodies are modeled with a tetrahedron mesh. As the stresses are significantly lower, these larger elements will have a negligible influence on the results. See figure 9 for the mesh of the VT model.

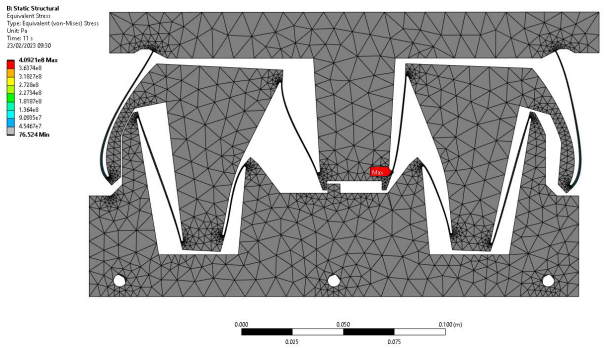

Figure 9. Von Mises stress result and mesh of FEM analysis of case 1 VT mechanism

The experimental setup can be seen in figure 10. The setup consists of 3 laser distance sensors. One sensor measures the x position while the other 2 simultaneously measure the parasitic translation of 2 points on the output body. The mechanism is pushed and pulled over its stroke using a linear motion stage. Using the x translation and the 2 top measurements the parasitic translation as well as rotation can be measured. This test is done multiple times without an external load applied and subsequently with an additional load of 9.81 N applied on the center of the output body.

The results of the 3 methods can be seen in figure 11-13. A good coherence in terms of parasitic translation and rotation are observed, while a small devia-

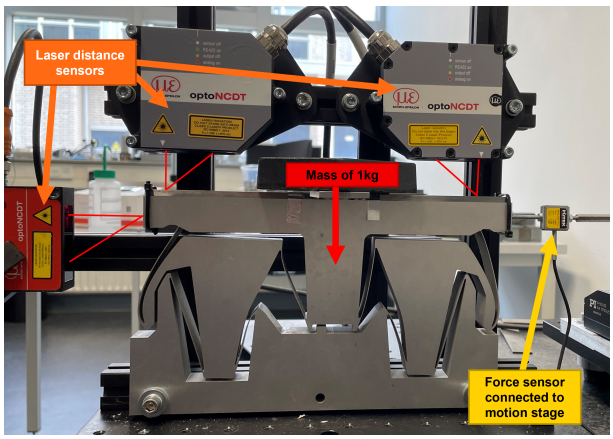

Figure 10. Experimental setup

tion in the results for induced parasitic motion are measured. The induced parasitic motion is less constant compared to the *SPACAR* and Ansys model.

This higher difference in induced parasitic motion can be caused by a multitude of factors like production errors and measurement errors. One main influence on the measurement data is the use of curve fitting to approximate the actual measurement data which is 3 noisy signals coming from the laser distance sensors. The measured signal is fitted using a 4th order polynomial. These fitted signals from laser 1 and 2 are then used to calculate the parasitic motion and this parasitic motions for the 2 measurements (with and without the external load) are used to calculate the induced parasitic motion.

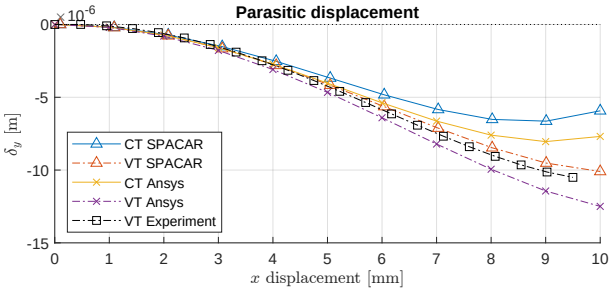

Figure 11. parasitic translation

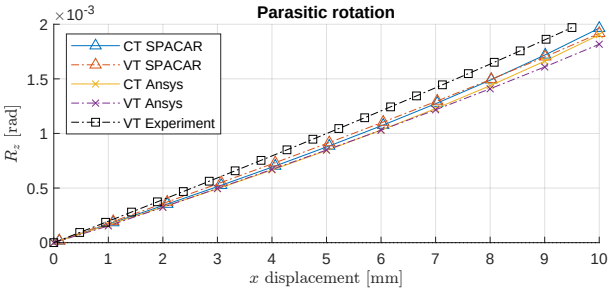

Figure 12. parasitic rotation

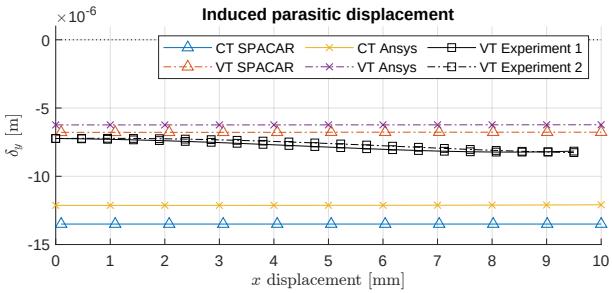

Figure 13. induced parasitic motion

4 Discussion

This method of optimizing new mechanisms is very time-consuming, to see the improvement this additional time brings, the mechanisms from step 1 for Case 1 and Case 2 and the CT mechanism from Case 3 are compared to two commonly used mechanisms, the double parallelogram and the Roberts mechanism. These mechanisms are optimized in *SPACAR* using the same constraints as the 3 cases.

For Case 1, the results can be found in table 9. A clear increase in support stiffness difference can be seen by using the double parallelogram mechanism as expected. The Roberts mechanism has much better performance, however still about a factor 1000 higher than the optimized design using this paper's method. The normalized support stiffness for the 3 mechanisms can be seen in figure 14.

Table 9. Comparison of results for mechanisms designed for minimal support stiffness difference using a double parallelogram(DP), a Roberts mechanism and the optimized design using initially curved flexures.

			DP	Roberts	Optimized
δy	[m]	<10e-6	1.38E-06	8.90E-06	7.99E-06
δrot	[rad]	<0.002	2.89E-04	4.50E-05	6.98E-04
δC_x	[-]	Obj	56.3%	3.3%	0.0026%
R_C	[-]	>100	100	446	123
Stroke	[mm]		10	10	10

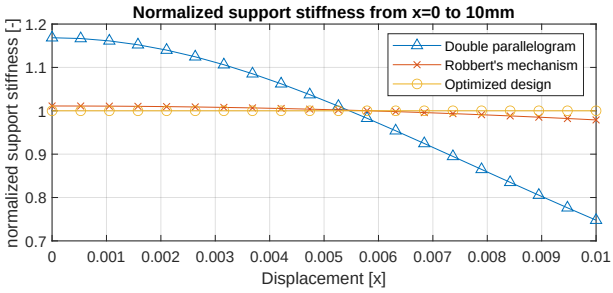

Figure 14. Normalized support stiffness for a double parallelogram, a Roberts mechanism and optimized mechanisms. All the mechanisms are optimized for a minimum support stiffness difference.

The same comparison is made for Case 2. As can be seen in table 10, the parasitic translation is lowest for the optimized initially curved mechanism, however closely followed by the double parallelogram mechanism. However, a significant difference can be seen in δC_x, this is not optimized for and both designs are valid within the constraints so no claims about this can be made.

Table 10. Comparison of results for mechanisms designed for minimal parasitic motion using a double parallelogram(DP), a Roberts mechanism and the optimized design using initially curved flexures.

			DP	**Roberts**	**Optimized**
δy	[m]	Obj	1.74E-08	3.27E-07	1.36E-08
δrot	[rad]	<100e-6	3.53E-06	2.81E-05	3.52E-05
δC_x	[-]		9957%	42.9%	1486%
R_C	[-]	>100	272	3167	496
Stroke	[mm]		10	10	10

And for the last case, the comparison is made. As can be seen in table 11, the initially curved optimized design has a significantly larger stroke compared to the other 2 mechanisms.

Table 11. Comparison of results for mechanisms designed for maximum stroke using a double parallelogram(DP), a Roberts mechanism and the optimized design using initially curved flexures.

			DP	**Roberts**	**Optimized**
δy	[m]	<10e-6	9.37E-08	7.02E-06	9.3E-06
δrot	[rad]	<0.002	1.14E-05	7.43E-05	0.002
δC_x	[-]		27180%	302%	94%
R_C	[-]	>100	100	1365	106
Stroke	[mm]	Obj	16.6	20.6	27.6

It is intersesting to see that every optimized design results in approximately a half Roberts mechanism on the bottom. It seems that using this layout the intermediate body travels in a relatively straight motion and the top part is then responsible for the function of the mechanism. In Case 1, the function of the top 2 flexures is to hand over the support stiffness to each other when deflecting while it seems that in Case 2, the top flexures ensure a smaller parasitic motion. The third case is a bit different with the bottom 2 flexures being more initially curved and a bit more parallel to each other. Here besides rotation resulting in the translation, the translation as well is achieved by significant bending of these flexures. The top 2 flexures seem to have somewhat of the same function to increase the maximum stroke.

In test cases 1 and 2, the optimization is done for the stiffness ratio with and without a constrained $\overline{C}_x$. Another interesting case could be optimizing purely for a maximum $\overline{C}_y$. This could result in a mechanism with a significantly increased drive stiffness, however, if this is not an issue this could be beneficial as the support stiffness is increased as well.

No claims can be made that these mechanisms are the global minimum designs within the design space. The problem is extremely nonlinear and time-consuming that optimized mechanisms are defined as the best-found design within the function evaluation limit. This issue can be observed in Case 1, where when constraining the drive stiffness led to a higher stiffness ratio. The optimizer was able to make this mechanism, however, due to computation limitations, the best minimum found until that time was performing less. The benefits of even this "limited" search of the full design space results in mechanisms that perform significantly better in a lot of fields, but to show the full potential, a study can be done with the use of a computer cluster to do more function evaluations.

Something that is not taken into account is the manufacturing inaccuracies and induced stresses due to thermal loads during production. If these induced stresses are known they could be taken into account during optimization. If this seems to be an issue in terms of shorter life span due to for example crack forming, it is something worth looking into in the future.

Besides the stiffness in x and y direction, this planar case's last degree of freedom is the R_z and its corresponding M_z. In these cases no constraint is set on the minimum of this rotation stiffness, however, for some models, it was noticeable that one extra degree of freedom was present. This is mainly because the flexures from the intermediate body to the output body when mirrored were all close to crossing in the same virtual point. This is something that could be incorporated into a future study. A simple way of mitigating this problem is by putting the mirrored mechanism halves farther apart, but for small design spaces, this solution might not be a solution. Extending the distance between mirrored mechanisms could also help minimize the parasitic rotation if this is critical.

5 Conclusion

In this research 3 novel straight-line mechanisms are presented that are optimized for 3 of the main limiting factors of compliant mechanisms.

Several test cases have been examined with the aim of enhancing the stiffness ratio and increasing the range of motion while minimizing parasitic motion and peak stresses. Two test cases were conducted to demonstrate the potential for increasing support stiffness. In the first case, the stiffness ratio, C_y/C_x

is maximized for a mechanism with a near constant support stiffness, $\delta C_y < 0.1\%$. An increase of 89.3% in stiffness ratio was observed when compared to constant thickness flexures. This is largely due to a significant decrease in drive stiffness while support stiffness dropped less. When drive stiffness was constrained to be at least that of the CT mechanism, the stiffness ratio increased by 103.2%. In this case, when constraining the drive stiffness, a higher ratio is observed. This is due to the limited computation time.

The second test case aimed to increase the stiffness ratio for a mechanism with a maximum parasitic translation of 0.2 µm and maximum parasitic rotation of 100 µrad. Here, an 83.8% increase in stiffness ratio was achieved. The optimized design has lower drive stiffness and increased support stiffness of 25.9%. Constrained drive stiffness led to a stiffness ratio increase of 16.4% compared to the constant thickness flexure mechanism. However, support stiffness in the constrained drive stiffness case was lower than the unconstrained drive stiffness case, so in this case, a decrease in drive stiffness is also beneficial towards increasing support stiffness.

The final test case examined variable thickness mechanisms and their ability to translate longer distances before failure. Mechanisms were optimized using constant and variable thickness flexures. Within the same parasitic and stiffness ratio constraints, a 10.7% increase in stroke was achieved with the variable thickness flexure mechanism.

In conclusion, it can be stated that initially curved flexures show great promise in a whole range of applications. And on top of that, variable thickness and initially curved flexure mechanisms show improved performance in terms of support stiffness and stroke compared to constant thickness initially curved flexures.

References

[1] Hua Liu et al. "Design and modeling of a novel monolithic parallel XY stage with centimeters travel range". In: *Special Issue Article Advances in Mechanical Engineering* 9.11 (2017), p. 2017.

[2] Philipp Gräser et al. "High-precision and large-stroke XY micropositioning stage based on serially arranged compliant mechanisms with flexure hinges". In: *Precision Engineering* 72 (Nov. 2021), pp. 469–479.

[3] Lei-Jie Lai, Guo-Ying Gu, and Li-Min Zhu. "Design and control of a decoupled two degree of freedom translational parallel micropositioning stage". In: *Rev. Sci. Instrum* 83 (2012), p. 45105.

[4] C Werner, P C J N Rosielle, and M Steinbuch. "Design of a long stroke translation stage for AFM". In: *International Journal of Machine Tools and Manufacture* 50 (2009), pp. 183–190.

[5] Guangbo Hao and Jingjun Yu. "Design, modelling and analysis of a completely-decoupled XY compliant parallel manipulator". In: *Mechanism and Machine Theory* 102 (Aug. 2016), pp. 179–195.

[6] Guangbo Hao and Xianwen Kong. "A 3-DOF Translational Compliant Parallel Manipulator Based on Flexure Motion". In: (2012).

[7] Shorya Awtar and Alexander H Slocum. "Constraint-Based Design of Parallel Kinematic XY Flexure Mechanisms". In: (2007).

[8] Kee-Bong Choi and Doo-Hyeong Kim. "Monolithic parallel linear compliant mechanism for two axes ultraprecision linear motion". In: *Rev. Sci. Instrum* 77 (2006), p. 65106.

[9] Yangmin Li et al. "Design, Modeling, Control and Experiment for a 2-DOF Compliant Micro-Motion Stage". In: *International Journal of Precision Engineering and Manufacturing* 15.4 (2014), p. 735.

[10] Fujun Wang et al. "A 2-DOF nano-positioning scanner with novel compound decoupling-guiding mechanism". In: *Mechanism and Machine Theory* 155 (Jan. 2021).

[11] Jingjun Yu et al. "Design and experimental testing of an improved large-range decoupled XY compliant parallel micromanipulator". In: *Journal of Mechanisms and Robotics* 7.4 (Nov. 2015).

[12] Qingsong Xu. "New flexure parallel-kinematic micropositioning system with large workspace". In: *IEEE Transactions on Robotics* 28.2 (Apr. 2012), pp. 478–491.

[13] Qingsong Xu. "Design, testing and precision control of a novel long-stroke flexure micropositioning system". In: *Mechanism and Machine Theory* 70 (2013), pp. 209–224.

[14] D. M. Brouwer, J. P. Meijaard, and J. B. Jonker. "Large deflection stiffness analysis of parallel prismatic leaf-spring flexures". In: *Precision Engineering* 37.3 (July 2013), pp. 505–521.

[15] Brian P Trease and Sridhar Kota. "Design of Large-Displacement Compliant Joints". In: (2005).

[16] Miao Yang, Zhijiang Du, and Wei Dong. "Design and Modeling of a Variable Thickness Flexure Pivot". In: (Feb. 2019).

[17] Yang Miao et al. "Optimal design, modeling and control of a long stroke 3-PRR compliant parallel manipulator with variable thickness flexure pivots". In: *Robotics and Computer-Integrated Manufacturing* 60 (Dec. 2019), pp. 23–33.

[18] Jianwei Wu et al. "Modeling and analysis of conical-shaped notch flexure hinges based on NURBS". In: *Mechanism and Machine Theory* 128 (Oct. 2018), pp. 560–568.

[19] Girish Krishnan, Charles Kim, and Sridhar Kota. "A Metric to Evaluate and Synthesize Distributed Compliant Mechanisms". In: (2013).

[20] Martin Tschiersky et al. "Gravity Balancing Flexure Springs for an Assistive Elbow Orthosis". In: *IEEE TRANSACTIONS ON MEDICAL ROBOTICS AND BIONICS* 1.3 (2019).

[21] Hong Zhou and Nisar Ahmed. *Synthesis of path generation compliant mechanisms using variable width spline curves*. Tech. rep. 2014.

[22] Yu Jingjun et al. *A new family of large-displacement flexural pivots*. Tech. rep. 2007.

[23] Ke Wu, Gang Zheng, and Guangbo Hao. "Efficient spatial compliance analysis of general initially curved beams for mechanism synthesis and optimization". In: *Mechanism and Machine Theory* 162 (Aug. 2021).

[24] Hong Zhou and Kwun Lon Ting. "Shape and Size Synthesis of Compliant Mechanisms Using Wide Curve Theory". In: *Journal of Mechanical Design* 128.3 (May 2006), pp. 551–558.

[25] Ashok Kumar Rai, Anupam Saxena, and Nilesh D Mankame. "Synthesis of Path Generating Compliant Mechanisms Using Initially Curved Frame Elements". In: (2007).

[26] N.K. Meinders. "Compensating parasitic motions and cross-couplings in compliant mechanisms". PhD thesis. Delft: Delft University of Technology, 2021.

[27] Alexandre E Guérinot et al. "Compliant Joint Design Principles for High Compressive Load Situations". In: (2005).

[28] D M Brouwer, J P Meijaard, and J B Jonker. "Elastic element showing low stiffness loss at large deflection". In: ().

[29] Steven E Boer et al. "Multibody Modelling and Optimization of a Curved Hinge Flexure". In: *The 1st Joint International Conference on Multibody System Dynamics* (May 2010).

[30] J Rommers. "Design strategies for large range flexure mechanisms". PhD thesis. Delft: Delft University of Technology, June 2022.

[31] D H Wiersma et al. "Design and Performance Optimization of Large Stroke Spatial Flexures". In: (2014).

[32] *Modified Akima piecewise cubic Hermite interpolation - MATLAB makima - MathWorks Benelux*.

[33] N.K. Meinders. "Compensating parasitic motions and cross-couplings in compliant mechanisms". Delft: Delft University of Technology, 2021.

[34] J. B. Jonker and J. P. Meijaard. "SPACAR — Computer Program for Dynamic Analysis of Flexible Spatial Mechanisms and Manipulators". In: *Multibody Systems Handbook* (1990), pp. 123–143.

[35] *Surrogate Optimization Algorithm - MATLAB surrogateopt - MathWorks Benelux*.

[36] Douglas Schwarz. *Fast and Robust Curve Intersections*. 2023.

[37] *Buy Tough 1500 Resin*. URL: https://formlabs.com/eu/store/materials/tough-1500-resin/.

[38] *Form 3: Industrial-Quality Desktop SLA 3D Printer*.

5

Discussion

One of the harder parts of the project was to make a fast, consistent meshing tool, see appendix A.1 for more insight in what went into the meshing tool. This tool is optimized for these specific flexure designs, but when unrealistic geometries were evaluated, the solver returned errors as some elements had extreme aspect ratios. This was solved by means of telling the solver that this was an infeasible design and this way could continue. This was not an issue for this research, as these geometries were evaluated and all were unrealistic designs. The solver thus has a limited range of quality meshes but this range was sufficient for the desired flexure shapes.

SPACAR is fundamental in the ability to optimize new mechanisms using curved flexures. With simulation times of ± 20 seconds compared to 1 hour and 30 minutes for Ansys, still results in reliable and comparable results. Due to the highly nonlinear nature of the problem and utilizing these nonlinearities to our advantage, a limitation was still posed by simulation time. Using parallel optimization with 6 cores working in parallel, the optimizations still could take multiple days. This relatively limited simulation time prevented the investigations in terms of different lower and upper bounds for example on the minimum thickness of the flexures (more on this in appendix B.4) or on the influence of more or fewer elements used in *SPACAR* as just increasing the number of elements and evaluate the simulation results in slightly to sometimes moderately different results, as this increase or decrease in angles between elements have an influence on parasitic performance. To fully evaluate the difference, the same optimization must be done for more elements to draw conclusions. One way to speed up this process is by utilizing a more powerful computing cluster with many more cores to evaluate more mechanism geometries at the same time. In this research this posed a problem as the current version of *SPACAR* is unable to run on Linux systems that the systems at hand run on. Besides using a bigger computer, a promising feature *SPACAR* is working on are tapered elements. Dwarshuis [1] developed these elements in his Ph.D. research and these will be implemented in *SPACAR* in the future. Using tapered elements would potentially allow for fewer elements or increased accuracy. For small variations in cross-section compared to the length, the errors in stiffness are typically below 10% and errors in stress below 20%.

One of the assumptions of this research was that the mass of the 'rigid' bodies was not taken into account. This is not taken into account as the shape of the intermediate bodies is highly dictated by the geometry of the mechanism and how the body must be shaped to fit in between the flexures. See for example the mechanism from Case 1 where an additional thick beam is necessary to connect one of the flexures from the output body to the intermediate body. In further research, a good estimation can be made and integrated as these bodies can be adapted to save weight and still be sufficiently stiff.

6

Conclusion

In this research, two novel optimization approaches to increase support stiffness or lower the peak stress are presented. The first method uses bezier curves to parameterize the thickness profile of leaf flexures and these thickness profiles are optimized for 3 cases. The first case optimized the stiffness ratio C_x/C_{x0}, the second case maximizes the support stiffness C_x for the same drive stiffness. And lastly, Case 3 minimizes the maximum stress for the same drive stiffness. The use of VT increases performance in all 3 cases and show the ability to implement this method to improve a multitude of already existing mechanisms.

The second method optimizes not only the thickness profile of the flexures but optimizes mechanisms with 4 initially curved flexures. These mechanisms are optimized for CT and VT flexures and a comparison is made to show the increase in performance using VT flexures with initial curvature. To show the increase in performance, 3 test cases are used. Case 1 optimizes the support stiffness for a mechanism with a near-constant support stiffness over its deflection. Case 2 optimizes the support stiffness for a mechanism with a parasitic translation of only 0.2 µm and a parasitic rotation of only 100 µrad while having a stiffness ratio C_y/C_x of at least 100. The last case maximizes the stroke of a mechanism with constrained parasitic motion and with a stiffness ratio of at least 100. These mechanisms perform better than commonly used double parallelogram and Roberts mechanisms and by adding variable thickness to the flexures, the results show in all cases an additional performance increase.

This thesis showed that VT flexures show great promise in multiple fields and can be used to increase the performance of existing mechanisms or can be used in combination with initial curvature towards the design of mechanisms with significant performance increase in terms of support stiffness, precision and range of motion.

References

[1] Koen Dwarshuis et al. “Beams With a Varying Cross Section in the Generalized Strain Formulation for Flexure Modeling”. In: (2023).

[2] *Fusion 360 | 3D CAD-, CAM-, CAE- en PCB-software in de cloud | Autodesk*. Dec. 2022.

[3] E. Salvati and A. M. Korsunsky. “Micro-scale measurement & FEM modelling of residual stresses in AA6082-T6 Al alloy generated by wire EDM cutting”. In: *Journal of Materials Processing Technology* 275 (Jan. 2020).

[4] JPE. *Flexure engineering fundamental: Leaf spring*. Oct. 2021.

[5] D. M. Brouwer, J. P. Meijaard, and J. B. Jonker. “Large deflection stiffness analysis of parallel prismatic leaf-spring flexures”. In: *Precision Engineering* 37.3 (July 2013), pp. 505–521.

[6] D M Brouwer, J P Meijaard, and J B Jonker. “Elastic element showing low stiffness loss at large deflection”. In: ().

[7] J Rommers. “Design strategies for large range flexure mechanisms”. PhD thesis. Delft: Delft University of Technology, June 2022.

A

Appendix: Paper I

A.1. Meshing

To become computationally feasible to simulate thousands of iterations in an optimizer, design iteration time had to be significantly reduced by reducing most of the pre-processing tasks that are conducted in commercial software like Ansys Workbench or Comsol Multiphysics. Using Ansys python scripting in Spaceclaim to define the thickness, a full design iteration loop from parameters to results takes about 2 minutes. This is mainly because different software packages like SpaceClaim and Mechanical are opened and closed in the background, so there is a lot of overhead. The bare minimum we need is the nodes and the element connections. To do this more efficiently and more consistently, a custom 2D mesher was created that can create meshes from notches to flexures in a consistent way, so that results could be compared better in the optimizer.

Besides reducing the time by not relying on meshing in commercial software, reducing the number of elements saves time as well in solving. To minimize the elements needed while maintaining an accurate result a study was done to find the ideal compromise. For a constant thickness flexure with an ellipsoid fillet to a solid body, the number of elements in thickness is changed for the same load case and the reaction force, maximum stress and undeflected and deflected support stiffness are recorded. To simulate a real connection to the fixed world the half circle (see figure A.1) was added as this allows stress at the transition to be accurate as well. The number of elements in thickness is increased and compared with the result that 12 elements in thickness bring. The results are shown in table A.1. It clearly shows that the main difference can be observed for maximum stress.

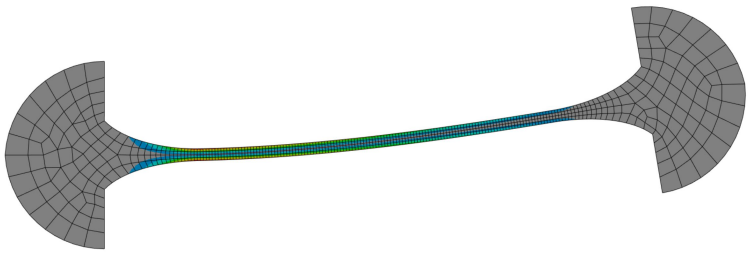

Figure A.1 Loadcase used for the mesh sensitivity analysis. Cantilever beam with 10% u/L deflection in y.

As can be seen in figure A.2, the automatic meshing does not result in consistent meshes, especially when the amount of elements increases over 4. Another thing that can be observed is that when an uneven amount of elements is used, the mesh becomes inherently unsymmetric along the midline of the flexure. To be able to create a good and consistent mesh, a mesh of 4 elements in thickness is

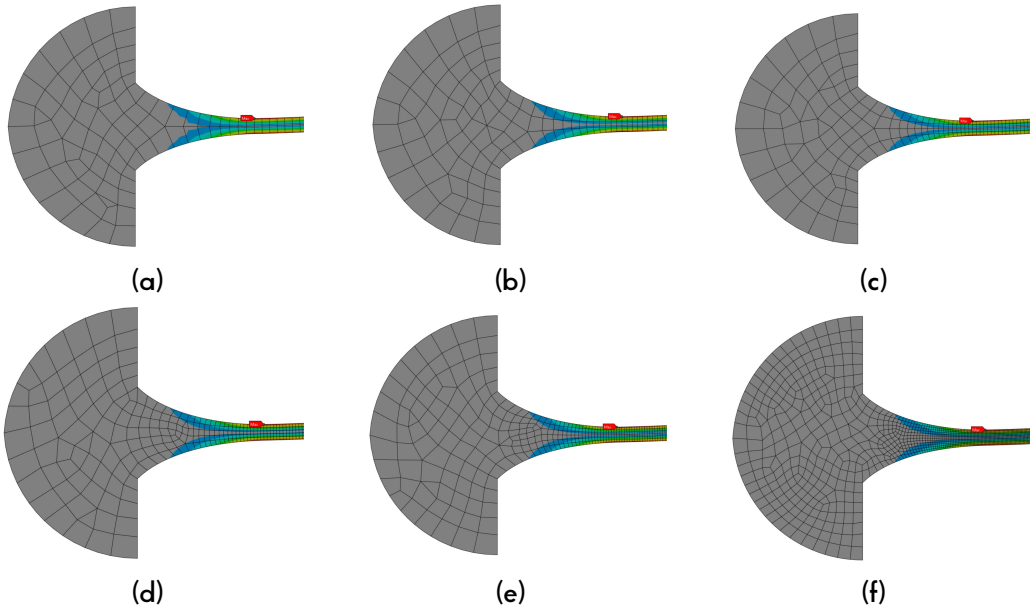

Figure A.2 a: n = 2, b: n = 3, c: n = 4, d: n = 5, e: n = 6, f: n = 12

Table A.1 Comparrison of the different number of elements in thickness of the flexure. The difference Δ is compared to the mesh using 12 elements in thickness.

n		**2**	**3**	**4**	**5**	**6**	**12**
nr. elements		295	492	762	1157	1605	6080
Fr	[N]	765.15	764.94	764.76	764.75	764.75	764.76
Δ		0.05%	0.02%	0.00%	0.00%	0.00%	
σ_{max}	[Pa]	7.75E+08	7.77E+08	7.78E+08	7.79E+08	7.78E+08	7.79E+08
Δ		0.6%	0.3%	0.2%	0.1%	0.1%	
C_{x_0}	[N/m]	1.88E+09	1.88E+09	1.88E+09	1.88E+09	1.88E+09	1.88E+09
Δ		0.0%	0.0%	0.0%	0.0%	0.0%	
C_x	[N/m]	1.60E+09	1.60E+09	1.60E+09	1.60E+09	1.60E+09	1.60E+09
Δ		0.1%	0.0%	0.0%	0.1%	0.0%	

used as it is symmetric over its mid-line and does not use too many elements as this scales roughly by $elements^2$ and the error on maximum stress is below 0.5% (normally standard for stress convergence criteria in Ansys). To generate a good and comparable mesh for all design iterations, a custom mesher was built just for this purpose and is optimized for the meshing of this specific flexure shape. Looking at the meshes that Ansys generates (figure A.2) and looking at where higher stresses occur, the mesher is made to have good quality elements in these areas. This means nicely shaped elements along the outer edge that shapes nicely along with the curvature near the base. Just like the Ansys mesh with 4 elements in the thickness (figure A.2.c), the custom mesher will add elements when the angle on the ends increases. See figure A.3 for a similar mesh made by the custom mesher.

One other advantage of the optimized designs is that in theory, fewer peaks in stress occur and thus less local refinement is necessary. The mesher generates a mesh with quadratic elements, thus resulting in better stress results. To include the area where in constant thickness flexures without a proper fillet to the solid body exhibit the highest stress, a ring of 1 element is added. The connection to the 'rigid' world is not infinitely stiff and is in this way included. The edge of this ring is fixed on the base and a rigid connection to the remote output node is connected to the ring on the end.

Using the bezier curves and equally spaced nodes on these curves over their length, a mesh can be generated. The problem with this approach however is that where the flexure is thinnest, the elements

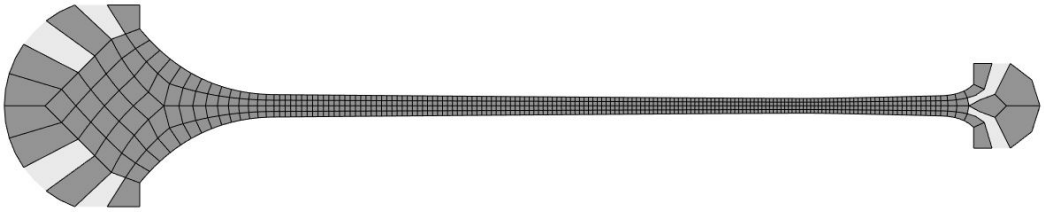

Figure A.3 Mesh generated by custom mesher. Dark gray elements have an element quality above 0.75

are much wider than where the flexure is thickest, where the elements are much thinner. To get the most accurate results, being as close as possible to a 1:1 ratio mesh element is preferred. So to combat this problem an implementation of a bias factor is implemented. A bias factor is a ratio of the largest length to the shortest element using a quadratic size increase, see equation A.1. The bias factor is defined as r^{n-1}, with r as the growth rate. If we want the height of the first element(h_1) to be equal to its width, the first element's length must be h_1. If we want the last element to have the same width as its height(h_2), $h_1 * r^{n-1}$ must be equal to h_2. This results in a growth rate r as stated in equation A.2.

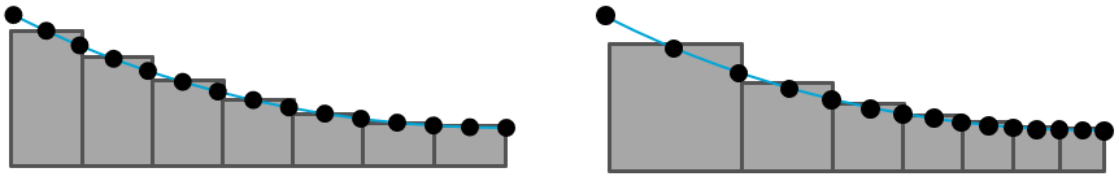

Figure A.4 On the left: equally spaced nodes, on the right: ideally scaled elements.

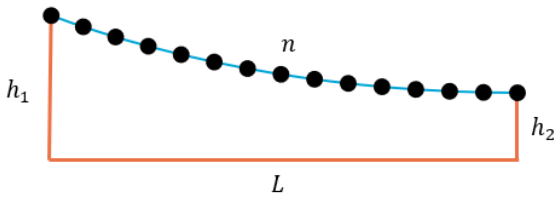

Figure A.5 If the first element is as long as h_1 and the last element is as long as h_2, it results in a 1:1 aspect ratio mesh.

$$L = \sum_{i=0}^{n-1} l_1 \cdot r^i \rightarrow L = h_1 \cdot \left(1 + r + r^2 + ... + r^{n-1}\right) \tag{A.1}$$

$$h_1 \cdot r^{n-1} = h_2 \rightarrow r = \left(\frac{h_2}{h_1}\right)^{\frac{1}{n-1}} \tag{A.2}$$

This gives approximate same aspect ratio elements, however, the aspect ratio is also of importance. The aspect ratio is defined as the width of the element divided by the height. This bias factor implementation realizes nearly the same aspect ratio elements, however, the aspect ratio that is desired must be achieved by increasing or decreasing the number of elements. In the mesher this is done iteratively. A mesh with just 2 elements along the bezier curve is evaluated for its aspect ratio, then iteratively elements are added until the desired aspect ratio is achieved.

Now the outer edges of the flexure have their nodes positioned, the rest of the nodes can be placed. Having looked at the methods Ansys uses to mesh these geometries, a similar approach was used. The majority of the flexure uses 4 elements in its thickness, however near the base and end of the flexure, its thickness increases resulting in a steeper angle compared to the horizontal mid-line of the flexure, see figure A.6. This results in poorly shaped elements. Looking at the Ansys mesh (figure A.2 .c), it can be seen that from a certain moment when the elements are stretched a significant amount, an additional element is added in the middle to better maintain the desired aspect ratio and element sizing along the edge. In the mesher, this is done by means of a minimal angle($30\,°$) the elements along the edge have compared to the midline. See figure A.7 for the improved mesh aspect ratio when taking the minimal angle into account.

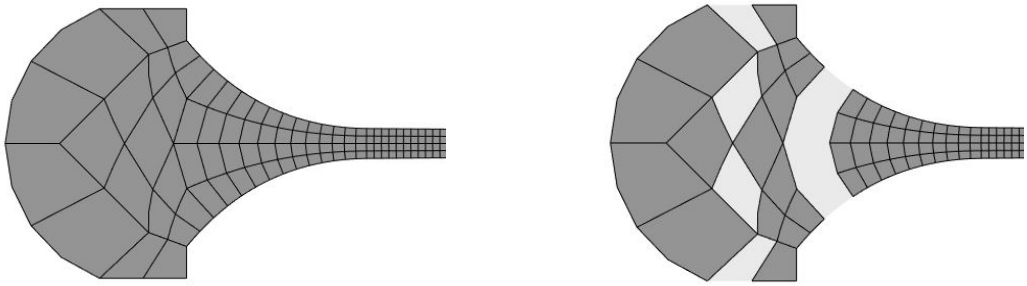

Figure A.6 a: Mesh with a high angle before elements are added in the middle and in b: the elements with an aspect ratio below 1.5 are shown.

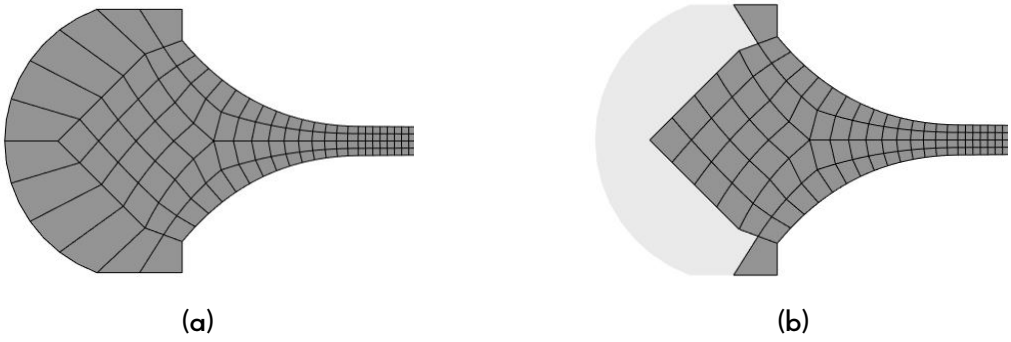

Figure A.7 a: Mesh with a $30°$ before elements are added in the middle and in b: the elements with an aspect ratio below 1.5 are shown.

A.2. Mesh aspect ratio

To minimize simulation time for optimizing, the influence of the aspect ratio of the elements of the middle section of the flexures is increased, see figure A.8 of an example of using an aspect ratio of 4 for the elements in the midsection.

Figure A.8 Mesh with a midsection aspect ratio of 4.

The found optimum was then compared with its 1:1 aspect ratio counterpart and all results were within 0.1%. To find out what the minimum aspect ratio is to reduce computation time further, a study is done for the 3 cases. The results of an aspect ratio of $1, 2, 4, 6, 8$ and 10 are evaluated and the results are shown in table A.2, A.3 and A.4. As can be seen in table A.4, the only property that is slightly influenced is the stress and as can be seen in table A.2 for an aspect ratio of 10, the stiffness results start to diverge.

To model stiffness accurately, an aspect ratio of 8 seems to be an ideal optimum between accuracy and computation time. An accurate mesh to reliably model stress is a bit more complex. The stress peak seems to occur exactly where the fillet transitions to the midsection. this can be modeled better by means of an added bias factor to create smaller elements near this area and bigger elements near the middle. This is something that could be added in future work.

Table A.2 Influence on results of a flexure optimized for maximum support stiffness ratio using different aspect ratios(AR) of the elements in the midsection.

AR		1	2	4	6	8	10
σ_{max}	[Pa]	4.00E+08	4.00E+08	4.00E+08	4.00E+08	4.01E+08	4.01E+08
			0.00%	**0.02%**	**-0.01%**	**0.06%**	**0.15%**
C_{x0}	[N m^{-1}]	2.62E+09	2.61E+09	2.62E+09	2.62E+09	2.62E+09	2.62E+09
			-0.21%	**0.01%**	**0.07%**	**0.02%**	**0.15%**
C_x	[N m^{-1}]	9.33E+08	9.32E+08	9.33E+08	9.32E+08	9.33E+08	9.36E+08
			-0.07%	**0.04%**	**-0.02%**	**0.07%**	**0.39%**
C_x/C_{x0}	[-]	0.356341	0.356831	0.356456	0.356036	0.356538	0.357202
			0.14%	**0.03%**	**-0.09%**	**0.06%**	**0.24%**
time	[s]	30.00	16.60	11.60	10.50	8.30	8.30
			34.80%	**24.32%**	**22.01%**	**17.40%**	**17.40%**

Table A.3 Influence on results of a flexure optimized for maximum deflected support stiffness using different aspect ratios(AR) of the elements in the midsection.

AR		1	2	4	6	8	10
σ_{max}	[Pa]	4.00E+08	4.00E+08	4.00E+08	4.00E+08	4.00E+08	4.00E+08
			0.00%	**0.00%**	**0.01%**	**0.02%**	**0.03%**
C_{x0}	[N m^{-1}]	3.17E+09	3.17E+09	3.18E+09	3.17E+09	3.18E+09	3.18E+09
			0.00%	**0.08%**	**0.00%**	**0.08%**	**0.08%**
C_x	[N m^{-1}]	8.08E+08	8.08E+08	8.08E+08	8.08E+08	8.08E+08	8.08E+08
			0.00%	**0.02%**	**0.00%**	**0.03%**	**0.03%**
C_x/C_{x0}	[-]	0.25461	0.25461	0.254448	0.254609	0.254488	0.254488
			0.00%	**-0.06%**	**0.00%**	**-0.05%**	**-0.05%**
time	[s]	47.7	24.60	17.80	13.50	9.00	8.30
			51.57%	**37.32%**	**28.30%**	**18.87%**	**17.40%**

Table A.4 Influence on results of a flexure optimized for minimum stress using different aspect ratios(AR) of the elements in the midsection.

AR		1	2	4	6	8	10
σ_{max}	[Pa]	2.85E+08	2.83E+08	2.83E+08	2.82E+08	2.82E+08	2.82E+08
			-0.62%	**-0.81%**	**-1.09%**	**-1.20%**	**-1.19%**
C_{x0}	[N m^{-1}]	1.51E+09	1.51E+09	1.51E+09	1.51E+09	1.51E+09	1.51E+09
			0.05%	**-0.12%**	**-0.12%**	**0.05%**	**0.05%**
C_x	[N m^{-1}]	9.92E+07	9.92E+07	9.91E+07	9.92E+07	9.92E+07	99163064
			0.01%	**-0.01%**	**-0.01%**	**0.01%**	**0.01%**
C_x/C_{x0}	[-]	0.065592	0.065566	0.065664	0.065665	0.065566	0.065566
			-0.04%	**0.11%**	**0.11%**	**-0.04%**	**-0.04%**
time	[s]	51.2	30.60	19.30	14.70	13.80	12.80
			59.77%	**37.70%**	**28.71%**	**26.95%**	**25.00%**

B

Appendix: Paper II

B.1. Self intersection constraint

To see whether or not the self-intersection constraint needs to be added the extreme case is investigated to see what the minimum length of a flexure must be to not have a self-intersection. The maximum curvature can be obtained if $l = 0.9$ and $b = 0.5$ as can be seen in figure B.1.

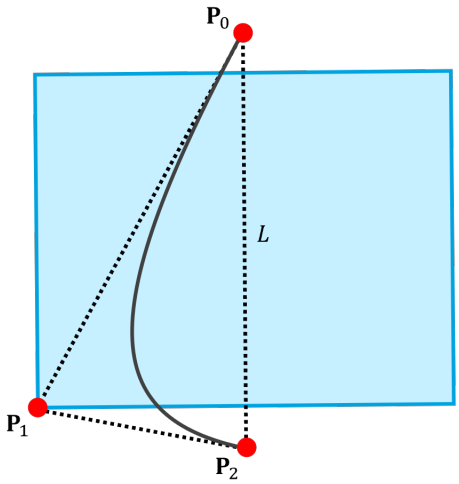

Figure B.1 Extreme case with $l = 0.9$ and $b = 0.5$. In blue is the constraint space for P_1.

This bezier curve scales with its length L but the thickness remains a constant maximum thickness. So an investigation is done on how small L can be without having self-intersections issues.

A length L of 4mm is a minimum as can be seen in figure B.2. When decreasing this length you get a self intersection as can be seen in figure B.3. As flexures of 4mm result in lumped hinges, this will not occur in one of the test cases and thus this constraint can be neglected.

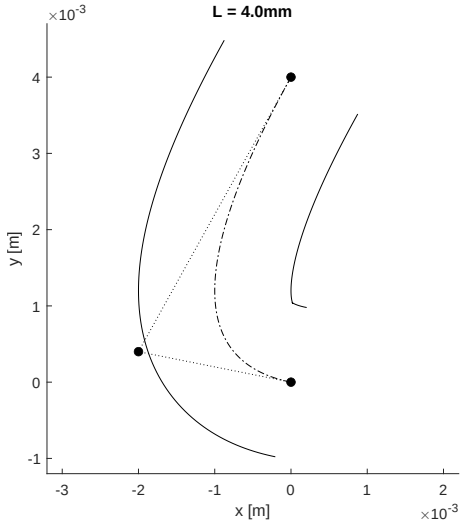

Figure B.2 $t = 2mm$ and $L = 4mm$.

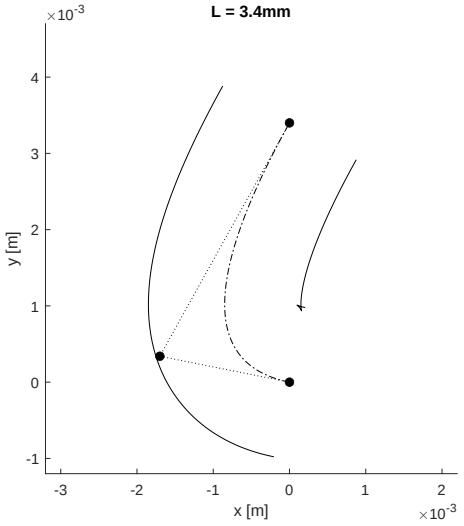

Figure B.3 $t = 2mm$ and $L = 3.4mm$.

B.2. Finite element analysis

In this chapter, the test setup and data processing and the FEM simulation in Ansys will be discussed. First, the FEM analysis will be discussed, then the experimental setup will be discussed for measurements of case 1 and lastly, the results from *SPACAR*, Ansys and the experiment will be compared.

B.2.1. FEM analysis

In this section, the FEM simulation for all 3 mechanisms will be discussed. The FEM analysis is conducted in Ansys 2022 R2.

To go from *SPACAR* models to 3d solid geometry, Fusion 360 is used. Fusion 360 is a cloud-based 3d modelling software platform from Autodesk for product design and production [2].

Fusion 360 has a bezier curve tool and with the control point coordinates and the flexure thickness profile, the flexures can be modeled. The connecting rigid bodies are then modeled and a built-in FEM tool in Fusion 360 is used to see possible intersections for the designed stroke. In figure B.4 - B.6 the 3 3d models for the 3 test cases can be seen. Only the 3d model for test case 1 is used to do a FEM analysis. To mitigate stress peaks, fillets of 0.5 mm are added and taken into account in the simulation.

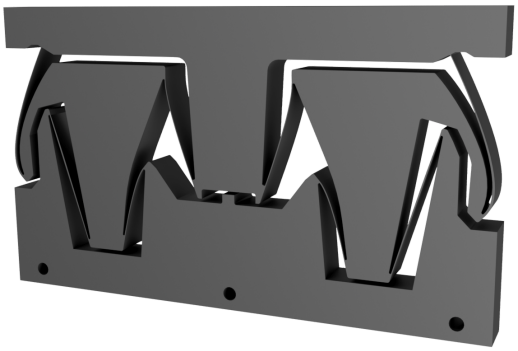

Figure B.4 3d model for test case 1, Maximizing stiffness ratio for a near constant support stiffness mechanism using VT flexures.

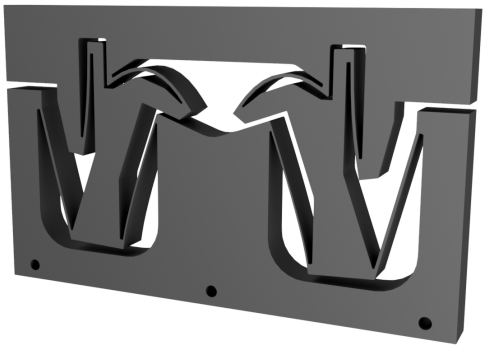

Figure B.5 3d model for test case 2, Maximizing stiffness ratio for a minimum parasitic motion mechanism using CT flexures.

To get an accurate result, quadratic mesh elements with 2 elements in flexure thickness are used. The Solid bodies are modeled with quadratic tetrahedrons as this allows for more easy meshing and rapid increase in element size as the stresses are so minimal in these bodies.

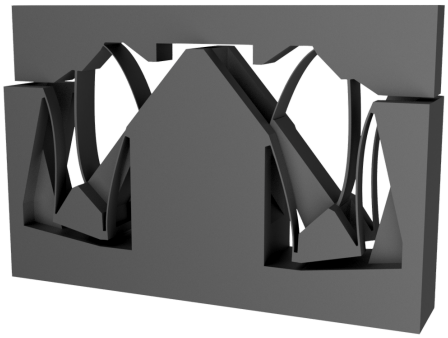

Figure B.6 3d model for test case 3, Maximizing stroke with constrained parasitic behavior using CT flexures.

Parasitic motion is measured by using 2 probes($p1$ and $p2$, with each a x and y component). One on the very left top corner and one on the very right top corner. The distance of these points to each other, L, is known and therefore the parasitic behavior can be measured as follows with i the load step.

$$\delta y(i) = \frac{p1_y(i) + p2_y(i)}{2} \tag{B.1}$$

$$\delta rot(i) = \sin^{-1}\left(\frac{p2_y(i) - p1_y(i)}{L}\right) \tag{B.2}$$

To measure the induced parasitic motion, an external load of 9.81 N in negative y direction is applied in the center of the output body and the same results are measured.

The resultant deformation and mesh can be seen in figure B.7. The maximum stress occurs on the interface between the end of one flexure and the fillet. To more accurately mesh this area, a few extra cubic elements are added and the bias for the flexure elements was chosen to have more equal-length elements beside each other. These extra elements can be seen in figure B.8 as the green elements and in figure B.9 the resultant stress distribution can be seen. With the altered mesh the maximum stress is on the surface of good shaped elements and the stress is already dropping before the transition to pyramid mesh elements. This gives a more accurate value of the maximum stress in the mechanism as this is the limiting factor.

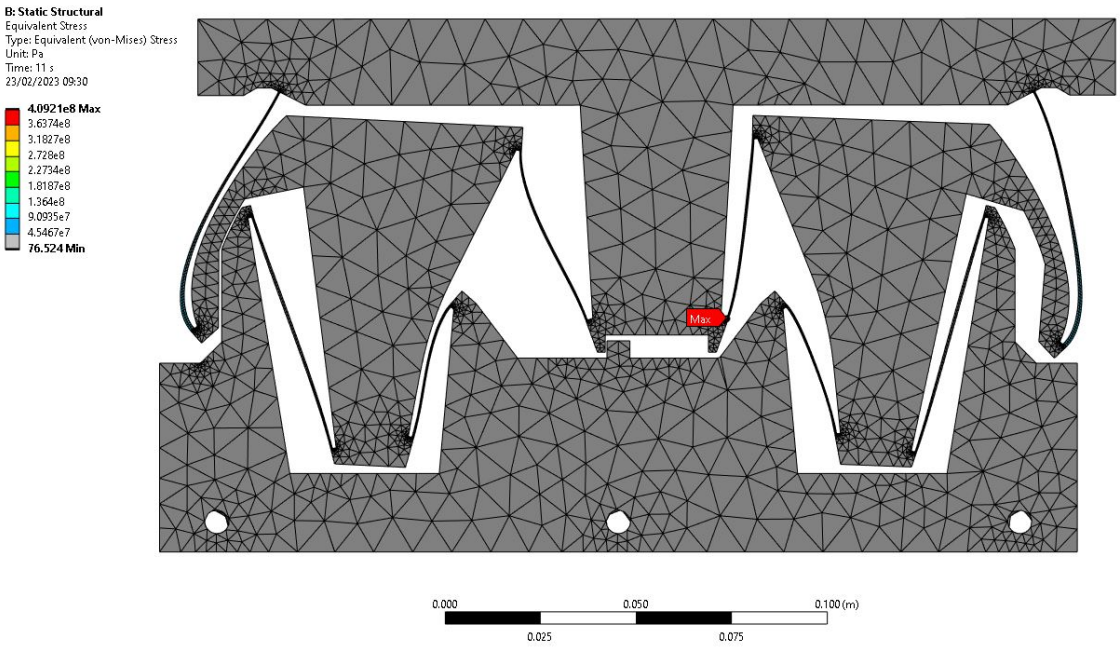

Figure B.7 Deformed mesh and maximum stress of Case 1 VT.

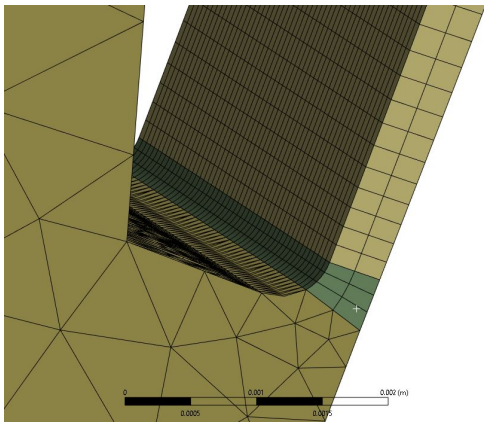

Figure B.8 Extra hex elements added to fillet as shown in green.

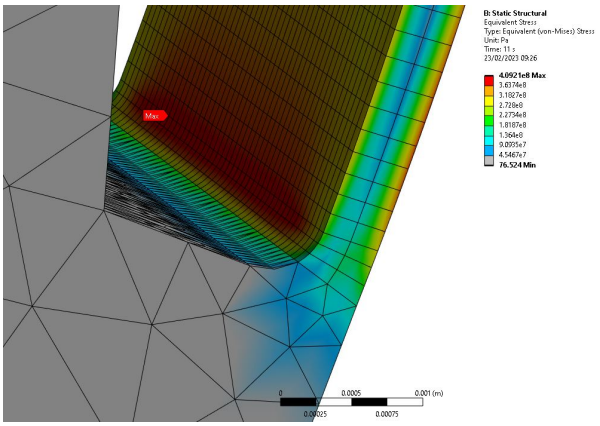

Figure B.9 Von Mises stress results for the new mesh with peak stress shown with red pointer.

The parasitic motion and induced parasitic motion can be seen in Paper II.

B.3. Experimental setup

In this section, the prototype and its differences compared to the simulations will be elaborated on. After that the test setup will be discussed, followed by the data acquisition.

B.3.1. Aluminium 7075-T6 Prototype

For this test, an aluminium 7075-T6 prototype is produced. This is produced using wire EDM. It is assumed that tolerances of 1 to 5 µm can be obtained using this process.

Possible differences compared to Ansys can be caused by multiple things. The first is the material properties. For the Ansys simulation, generic aluminium 7075-T6 material properties are used. This could however differ slightly compared to the material used for the prototype.

The second difference could be caused by internal stresses in the flexures due to production. Wire EDM induces rapid heating and subsequent quick cooling (i.e. quenching). This can induce different material properties on the outside of the flexure compared to the inside and can cause internal stresses [3].

One last difference will be that the weight of the rigid bodies is not taken into account in *SPACAR* and this will have an effect on the parasitic motion. To show the influence of this mass, it is added in *SPACAR* and Ansys and the difference is measured. The initial parasitic displacement according to *SPACAR* is 3.1 µm. If this initial displacement is subtracted from all the load steps, a near identical parasitic motion can be observed, see figure B.10. This is most likely due to the constant support stiffness characteristics of the mechanism.

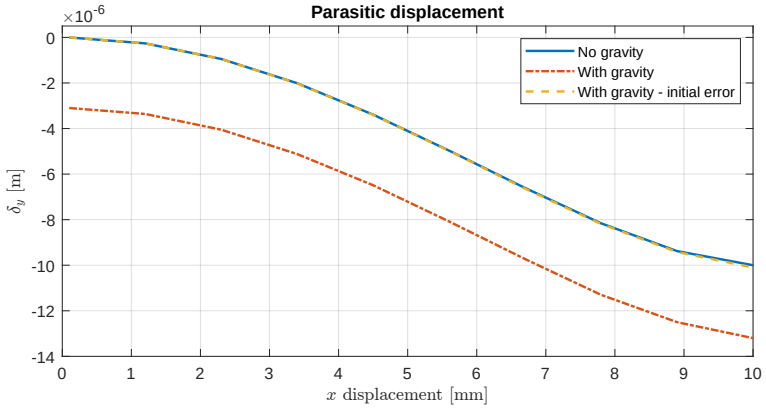

Figure B.10 Parasitic motion with and without gravity active.

B.3.2. Test setup

The test setup consists of 3 laser distance sensors, one force cell and a linear motion stage. The mechanism is connected by the bolt holes to the base structure which the linear stage is attached to as well. The linear stage is connected to the mechanism with a m3 thread and a force cell is positioned in between. One laser distance sensor is positioned horizontally to measure the x displacement and 2 laser sensors are positioned downward to measure the parasitic translation of 2 points at the ends of the output body. Using 2 distances over the output body ensures the parasitic translation measurement is not influenced by the translation in x when deflected, as the measurement area is not the middle of the mechanism anymore and can thus be influenced by parasitic rotation. Interpolating between the 2 measurements dependent on x ensures the translation is calculated in the exact middle. Besides these advantages, parasitic rotation can also be measured. See figure B.11 for the schematic test setup.

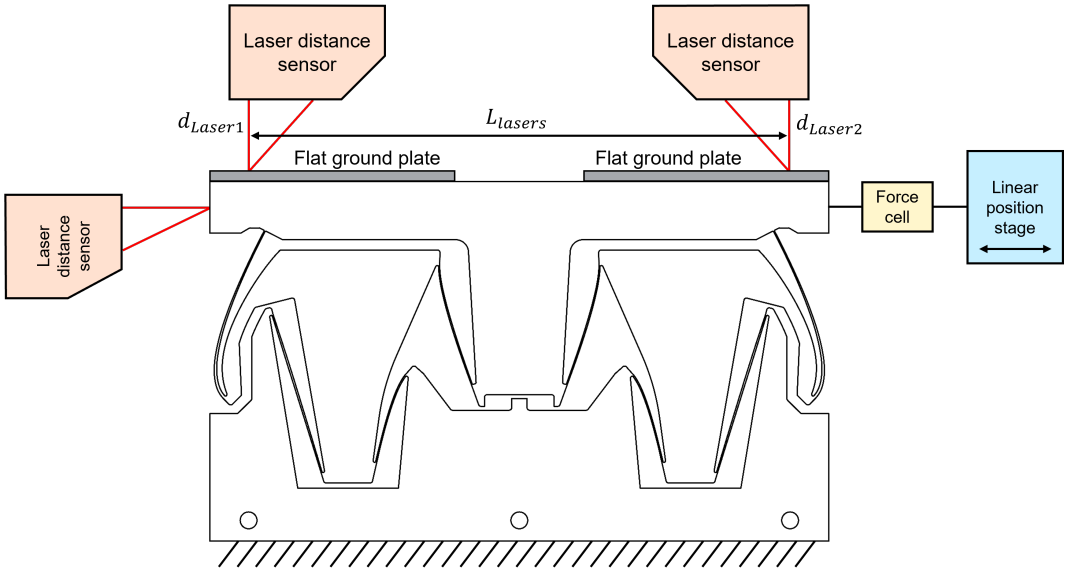

Figure B.11 Ideal test setup.

The wire EDM process leaves a slightly rough surface finish and the laser distance sensors(Micro-Epsilon optoNCDT 1750 with a measuring range of $2\,\text{mm}$) have a measuring repeatability of $0.1\,\mu\text{m}$ so every surface imperfection will be noticeable. To mitigate this problem, 2 flat ground stainless steel plates are placed on top of the top surface.

The laser sensors give an absolute distance measurement that increases when the distance is increased, so the measurements must be flipped and the start distance is dependent on the pre-alignment. To get relative motions, the initial distance is subtracted from the measurement distance. The parasitic motion of the center point is calculated using equation (B.5) and the parasitic rotation is measured using equation (B.6).

$$\delta_{yLaser1}(x) = -1 \cdot (d_{Laser1}(x) - d_{Laser1}(x=0)) \tag{B.3}$$

$$\delta_{yLaser2}(x) = -1 \cdot (d_{Laser2}(x) - d_{Laser2}(x=0)) \tag{B.4}$$

$$\delta_y(x) = \frac{\delta_{yLaser1}(x) \cdot (L_{lasers}/2 - x) + \delta_{yLaser2}(x) \cdot (L_{lasers}/2 + x)}{L_{lasers}} \tag{B.5}$$

$$\delta rot(x) = \sin^{-1}\left(\frac{\delta_{yLaser2}(x) - \delta_{yLaser2}(x)}{L_{lasers}}\right) \tag{B.6}$$

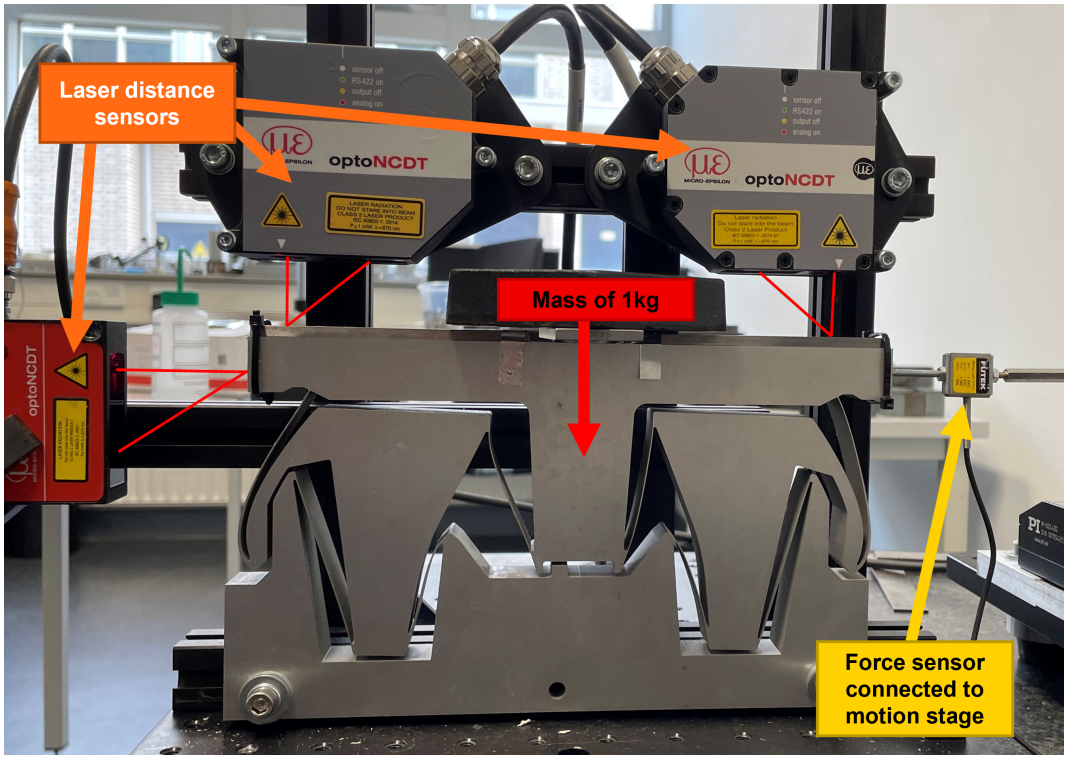

Figure B.12 Test setup with 1 laser(left) that measures the x position while 2 lasers on top measure the distance in y direction. On the right, attached to the yellow load cell, the positioning stage pulls the mechanism to the right.

B.3.3. Test procedure

The test will be conducted as follows. First, the reaction force of the force sensor will be measured before attaching the mechanism. Then the mechanism is attached and the motion stage is positioned so that a zero reaction force compared to the unattached state is measured. Now the mechanism is in its neutral position. From this neutral position, multiple measurements will be conducted by moving the motion stage continuously with a very fine step size back and forth while measuring the laser data. This procedure is then repeated after a load of 1 kg is applied.

B.3.4. Measurement errors

In figure B.11, the ideal test setup is shown. Apart from the errors described before, additional errors are present. The total measurement error is a cumulative error consisting of the following:

1. **Manufacturing error:** If the top surface of the mechanism is not straight but for example slanted, a parasitic motion can be measured when the mechanism is moving in a perfectly straight line.

2. **Surface error:** A measurement error can occur when the top surface that is measured is not flat enough. This can induce noise and non-existent added or reduced parasitic translation and hereby influence the accuracy of the measurement.

3. **Laser alignment error:** As the 2 lasers together determine the parasitic motion in the center of the output body, the alignment of these 2 lasers is quite important. As the output body experiences rotation as well, the x motion must be taken into account using equation (B.5). Here the assumption is that the lasers are exactly aligned an equal distance ($L_{lasers}/2$) from the exact midpoint and if this is not the case the parasitic motion can be influenced.

4. **Mechanism alignment error:** An additional error can occur when the mechanism is not aligned perfectly level. This however has a minimal influence on the parasitic motion due to the straight-line motion and the parasitic motion. If this alignment error becomes higher, the measurement can give a distorted result if the mechanism does not move in a perfectly straight line.

5. **Motion stage noise:** As the motion stage is a stepper-based system, vibrations created can be transferred to the mechanism and be measured by the lasers. To prevent this from influencing the measurement excessively, the measurement is repeated multiple times and the results are fitted over the full measurement set to even out these errors.

All these errors are visualised in figure B.13.

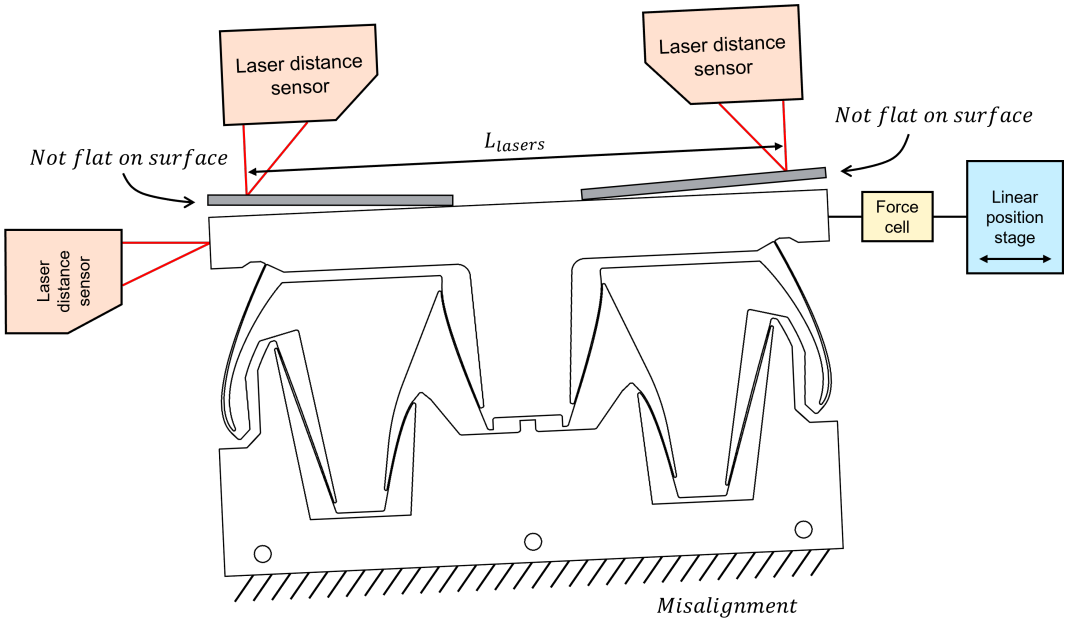

Figure B.13 Test setup with errors.

B.3.5. Data processing

The data gathered by the laser sensors is plotted in figure B.14. The measurement is quite noisy and as can be seen in the figure, at $x = 0$ the parasitic motion is not 0. This is due to the laser range of 2 mm and inaccuracy in aligning. This error can be compensated by subtracting the initial distance from the data set of each laser, however, due to the noisy measurement this is not possible, as this initial distance is not known. For this, the data of each laser is fitted with a polynomial curve. A polynomial of order 4 has been used and these fitted curves can be seen in figure B.15.

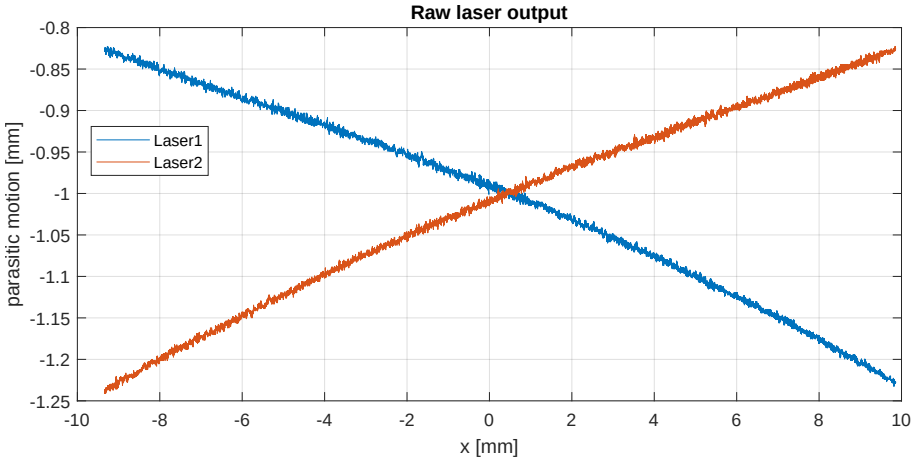

Figure B.14 Raw laser output data for the measurement without an external load applied.

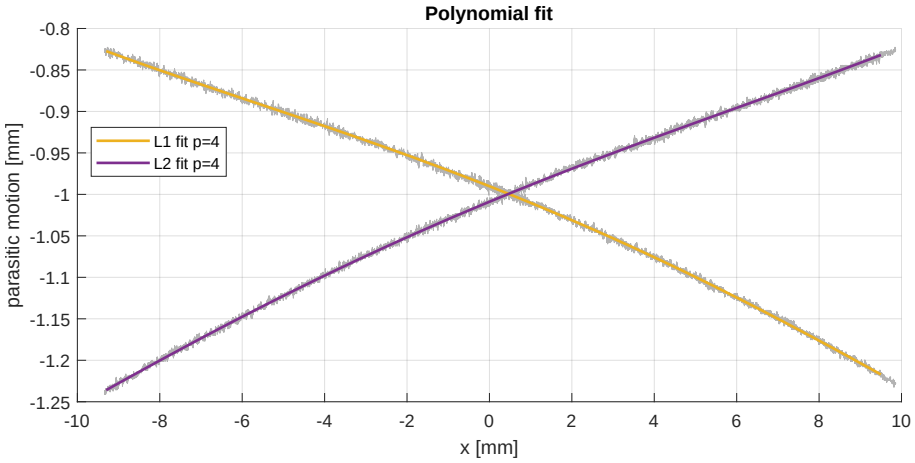

Figure B.15 Fitted laser data with 4th order polynomials.

Now the y measurement offset can be subtracted from the polynomial fit by setting the last constant to 0 resulting in the final fitted parasitic motion measurements for the 2 laser sensors. For the second measurement, with a weight of 1 kg added, the same procedure is run, however, now the offset in y from the first measurement is subtracted from the offset in y of the second measurement to incorporate the initial parasitic translation when undeflected due to the external load. Using equation (B.5) and (B.6), the parasitic translation and rotation are calculated and these results compared to the *SPACAR* and Ansys results can be seen in Paper II. To calculate the induced parasitic motion, the parasitic motion of the first measurement is subtracted from the parasitic motion of the second measurement with the applied weight. This induced parasitic motion for the measurement from 0 to -9.5 mm is flipped around the $x = 0$ axis so the difference can be observed and an average of the induced parasitic motion in positive and negative x displacement is taken. See figure B.16.

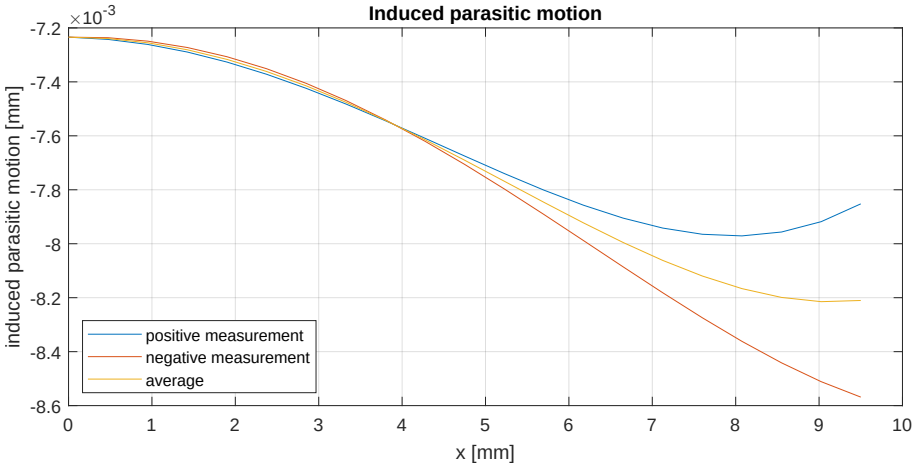

Figure B.16 Difference in induced parasitic motion between negative x direction measurement vs. positive x direction.

In figure B.16 it can be seen that the induced parasitic motion is different when displacing the mechanism in negative x direction compared to positive x direction. This can be caused by multiple reasons. The first reason could be that the mechanism is indeed not symmetric due to production errors. The second reason could be that the weight was not applied perfectly in the center of the mechanism. This influence of the placement of the weight is evaluated in *SPACAR* and with the weight placed 2 mm off-center, the difference in induced parasitic motion is only 0.07 µm. A third reason could be an error accumulation and this is probably the most influential. As we use the polynomial fit of the individual laser measurements, we induce an error. These 2 polynomials that have an intrinsic error are then used to calculate the resultant parasitic motion which does an interpolation between 2 inaccurate measurements. This is also the case for the measurement with the weight applied. Then to define the induced parasitic motion, these 2 flawed parasitic motion measurements are subtracted from each other resulting in an even more flawed response.

B.4. Stiffness ratio increase with lower minimal flexure thickness

Another factor that affects the stiffness ratio is the minimum thickness of a flexure. For the initial optimization, Tough 1500 from Formlabs is used and through testing, it was found that 0.6 mm was the minimum thickness to print flexures. That is why the lower bound on flexure thickness was set to 0.6 mm. When optimizing for aluminium 7075-T6, the minimum thickness was set to 0.4 mm as this is a minimum thickness that can confidently be produced using wire EDM. As the drive stiffness C_x and support stiffness when undeflected C_z scale linearly with different materials Young's modulus E, see equation (B.7) and (B.8), the ratio will remain the same. However, changing the minimum thickness will result in a change in the stiffness ratio. C_x will decrease its stiffness from $Eb/L^3 \cdot 0.6^3$ to $Eb/L^3 \cdot 0.4^3$, a drop of about 70%. The support stiffness C_z will drop only 33.3%. This results in a stiffness ratio increase of 125%. It is worth noting that this is only valid for undeflected flexures.

The stiffness of a fixed-guided flexure as can be seen in figure B.17, has a drive stiffness C_x defined as follows:

$$C_x = \frac{Ebt^3}{L^3} \tag{B.7}$$

The axial undeformed stiffness of a beam in tension is defined as follows:

$$C_z = \frac{EA}{l} = \frac{Ebt}{l} \tag{B.8}$$

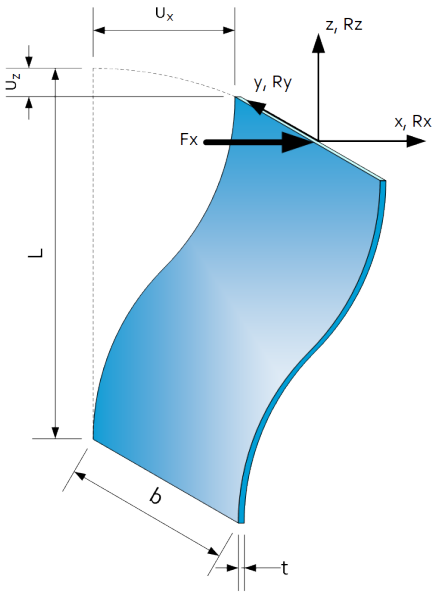

Figure B.17 Fixed-guided leaf spring. Figure retrieved from [4].

When taking into account the drop in support stiffness when deflected, the approximations posed by Brouwer, Meijaard and Jonker can be used [5] (see equation (B.9) for approximation for leaf springs with an aspect ratio of $w^2/(lt) \cdot (l/w)^2 > 200$ and equation (B.10) for flexures with an aspect ratio of $w^2/(lt) \cdot (l/w)^2 \leq 100$).

$$\frac{C_z}{C_{z0}} \approx \frac{1}{1 + (51/35)(u/t)^2} \tag{B.9}$$

$$\frac{C_z}{C_{z0}} \approx \frac{1}{1 + (u/t)^2} \tag{B.10}$$

Filling in equation (B.9) for $t = 0.6$ mm and 0.4 mm, we get a stiffness ratio of 0.25% and 0.11% respectively. This is both significantly lower than undeflected, however, it is clear that minimizing the thickness

of the flexure is of significance when assessing stiffnesses when deflected.

This all is however for simple single flexures and initial curvature is not taken into account. What also is not taken into account is the ability to hand over support stiffness when deflecting due to initially curved flexures straightening as in the work of Brouwer et. al. and Rommers [6, 7]. Using this method could improve the stiffness ratio when decreasing the thickness of the flexures.

B.5. Influence of curved flexures

To see the influence of curved flexures, a few flexures are straightened and the effects are observed.

B.5.1. The influence of the curved flexure in case 1

For case 1, the outermost flexure from the intermediate body to the output body is curved significantly. To see the influence of this curvature, the same simulation is done but changing this flexure to a straight one by changing b to 0 for flexure 3. The deformed mechanism can be seen in figure B.18. As can be seen in table B.1, the R_K can be improved significantly, however, this comes at the cost of an increase in support stiffness difference by a factor of 156 and a significant increase in parasitic motion. The large difference in terms of support difference ruins the purpose of this mechanism. This curved flexure hands over the support stiffness perfectly to ensure a small deviation similar to the methods used by Brouwer, Meijaard and Jonker [6] and Rommers [7].

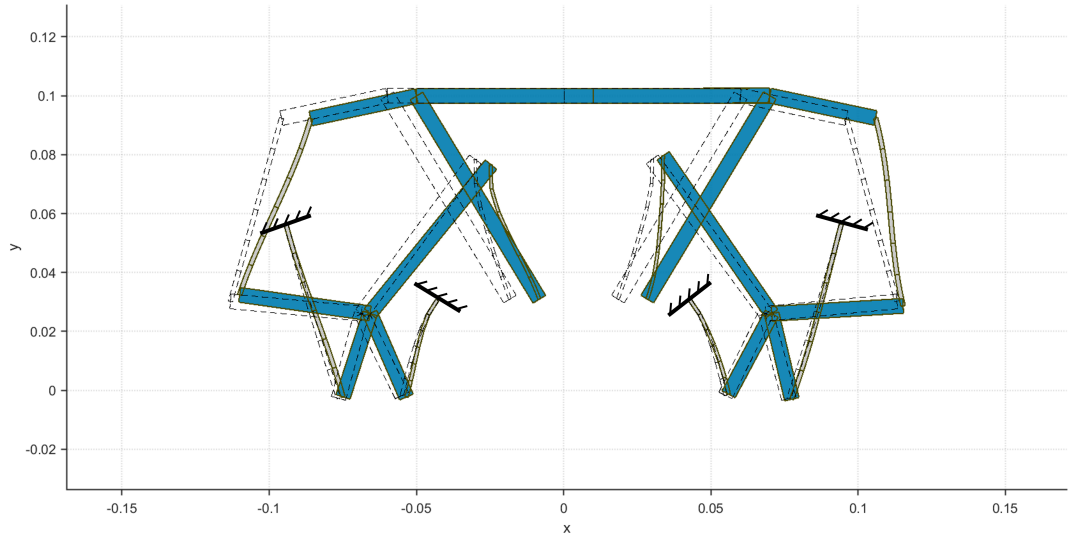

Figure B.18 Optimized CT mechanism with straight flexure 4.

Table B.1 Case 1: Optimized CT mechanism vs. the same mechanism but with straight flexure 3.

		curved	straight	
Dy	**[m]**	4.36×10^{-6}	4.27×10^{-5}	-881%
Par Rot	**[rad]**	1.70×10^{-3}	1.20×10^{-3}	29%
Stroke +-	**[mm]**	10	10	0%
Stress	**[MPa]**	14.7	15.0	-2%
Cy diff	**[-]**	0.1%	13.5%	-15577%
Cx mean	**[N/m]**	677.8	691.5	2%
Cy mean	**[N/m]**	1.74×10^{5}	4.04×10^{5}	131.9%
Rc	**[-]**	247.7	515.5	108.1%

B.5.2. The influence of the curved flexure in case 2

To see the influence of the most curved horizontal flexure, a simulation was done with all parameters the same as the optimized CT mechanism, but with the b value set to 0 for flexure 4. See figure B.19 for this displaced configuration. As can be seen in table B.2, the main influence of this curvature is on the parasitic behavior, being 5.6 and 18.3 times higher for parasitic translation and parasitic rotation respectively. This mechanism is not optimized with this flexure straight, so this can possibly be compensated for by the other curved flexures.

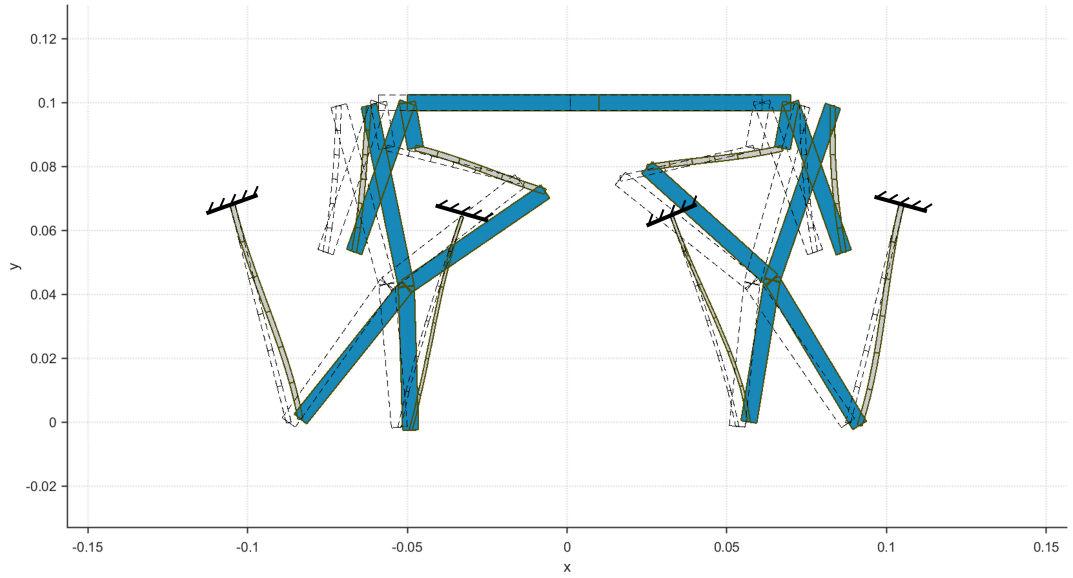

Figure B.19 Optimized CT mechanism for minimal parasitic motion with straight flexure 4.

Table B.2 Case 2: Optimized CT mechanism vs. the same mechanism but with straight flexure 4.

		curved	straight	
Dy	**[m]**	1.71×10^{-7}	1.12×10^{-6}	-555%
Par Rot	**[rad]**	3.21×10^{-5}	6.18×10^{-4}	-1829%
Stroke +-	**[mm]**	10	10	0%
Stress	**[MPa]**	10.03	12.78	-21%
Cy diff	**[-]**	11.0%	13.1%	-19%
Cx mean	**[N/m]**	613.8	683.3	11%
Cy mean	**[N/m]**	4.80×10^{5}	5.10×10^{5}	6.3%
Rc	**[-]**	728.6	686.2	-5.8%

B.5.3. The influence of curved flexures in case 3

To see the influence of the moderate curvature of the flexures, a simulation was done with all parameters the same as the optimized CT mechanism, but with the b value set to 0 for all flexures. See figure B.20 for this displaced configuration. As can be seen in table B.3, the main influence of this curvature is on the parasitic translation, being 46 times higher. As can be seen in figure B.21, the majority of the additional parasitic translation is due to the bottom 2 flexures being straight. Making only these flexures curved results in a parasitic translation increase from 46 to 12. An explanation for this could be that the error in the intermediate body is amplified and thus has a larger influence on the parasitic motion.

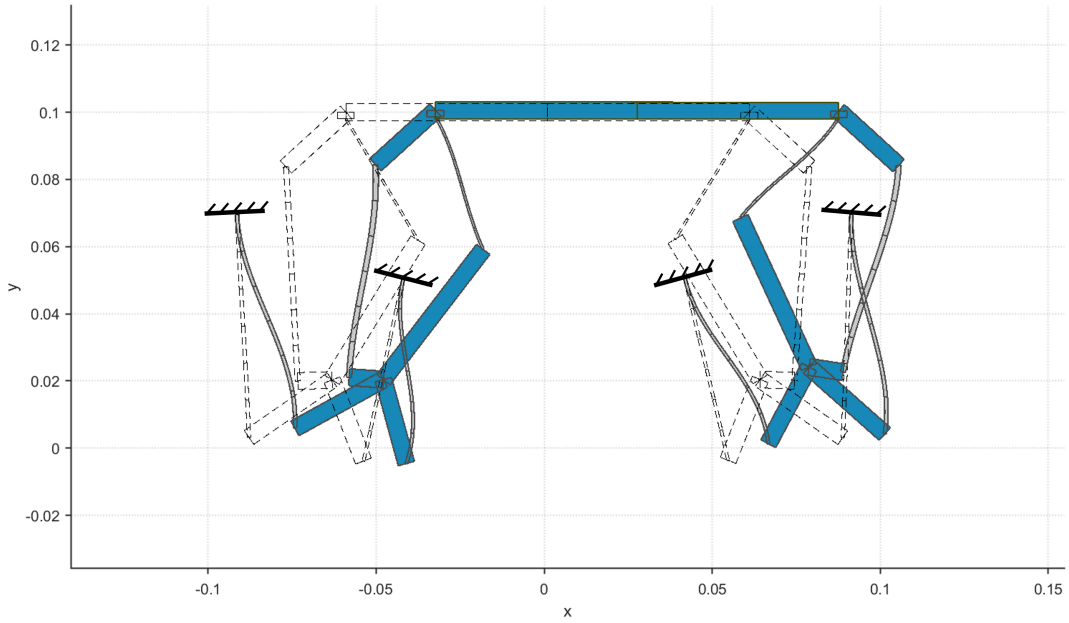

Figure B.20 Optimized CT mechanism for maximum stroke with straight flexures.

Apart from an increase in parasitic motion, the difference in support stiffness also increases dramatically. This, however, is not optimized for so no conclusions can be made about this.

Table B.3 Case 3: Optimized CT mechanism vs. the same mechanism but with straight flexures.

		curved	straight	
Dy	**[m]**	9.30×10^{-6}	4.41×10^{-4}	-4648%
Par Rot	**[rad]**	0.0020	0.0008	59%
Stroke +-	**[mm]**	27.646	27.646	0%
Stress	**[MPa]**	20.0	21.9	-9%
Cy diff	**[-]**	93.9%	546.8%	-482%
Cx mean	**[N/m]**	257.4	258.1	0%
Cy mean	**[N/m]**	4.41×10^{4}	2.60×10^{5}	489.7%
Rc	**[-]**	105.8	280.8	165.5%

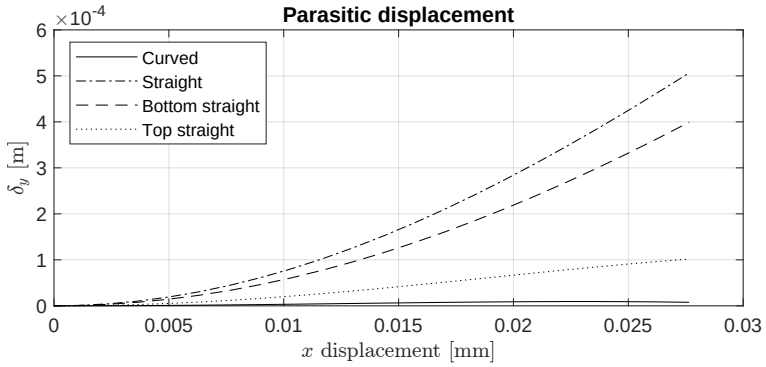

Figure B.21 Parasitic motion for curved and straight flexures for max stroke mechanism.